ABSTRACT

KHAN, MD TANVIR ARAFAT. Dynamic Modeling and Control of Distributed Generation System Driven by Solid-State Transformers: A Nonlinear Dynamical Approach. (Under the direction of Drs. Iqbal Husain and Aranya Chakrabortty.)

With advances in power electronic components and their controls, the penetration of renewable energy resources into the traditional power grid is steadily increasing. Higher penetration of the renewable sources causes power quality and stability problems such as voltage rise, frequency fluctuation, and subsequent impacts on the customer side. To address the penetration issues and facilitate the integration of renewable energy, the Future Renewable Electric Energy Delivery and Management (FREEDM) system has developed a power electronics based solid-state transformer (SST) which serves as an energy router for the power distribution system. SST interfaces distributed generation, storage and local loads on the low voltage side with the medium voltage node of the distribution grid. In this research, a physics based comprehensive dynamic model of FREEDM system is developed to analyze the feasibility based on system equilibrium which is one of the necessary conditions for stable operation of any power distribution system. State-space modeling of the SST along with the renewable generation sources and storage components has been adopted as the means of studying the feasible operating points and analyzing the dynamic behavior of the FREEDM system. The actual model of the single-SST system is a highly complex one with more than hundred state variables. Model reduction techniques are applied that leads to a 70^{th} order state-space average model, which is suitable for AC and DC energy cell system sizing, stability analysis, and controller design.

Based on the average model and feasibility analysis on the single SST, constraints for the multiple SST system on a microgrid has been developed, and subsequently the power sharing methods among the SSTs in a distribution network are analyzed. Two different methods have been proposed

and simulated by maintaining the node voltage or input current constant with a step change in any SST in the neighborhood. Energy storage and photovoltaic (PV) 'plug-and-play' units have important roles in the power sharing methods in the microgrids. Energy storage control for the microgrid has been developed considering instantaneous change from renewable generation or load demand; the storage controller can also assist in power sharing methods respecting the feasibility bounds with known system parameters and generation capacity of renewables.

For the PV units in residential FREEDM system, a method for a quick, low-cost installation has been developed to facilitate an autonomous and 'plug-and-play' (PnP) installation for flexible SST operation. The method addresses the cost challenge which is one of the biggest obstacles of renewable energy integration into any power distribution system. PnP system has been developed with the emphasis on the controls, software, and system level communications within the system. A PV Utility Interface (PUI) circuit has been built for automated electrical safety checks and authentication for the PnP PV system. Fully developed system has been demonstrated for a real-time installation which shows 95% reduction in installation time along with the potential to reduce the residential PV system cost by $0.3/watt.

Dynamic Modeling and Control of Distributed Generation System Driven by Solid-State Transformers: A Nonlinear Dynamical Approach

by
Md Tanvir Arafat Khan

A dissertation submitted to the Graduate Faculty of
North Carolina State University
in partial fulfillment of the
requirements for the degree of
Doctor of Philosophy

Electrical Engineering

Raleigh, North Carolina

2018

APPROVED BY:

_____	_____
Dr. Iqbal Husain Committee Co-Chair	Dr. Aranya Chakrabortty Committee Co-Chair
_____	_____
Dr. Wensong Yu	Dr. Andre Mazzoleni

DEDICATION

To my mother Bilkis Khan and father Md. Mainur Rahman Khan who are the idols and inspirations of my life.

BIOGRAPHY

Md Tanvir Arafat Khan received his B.Sc. degree in Electrical and Electronic Engineering (EEE) from Bangladesh University of Engineering and Technology (BUET), Dhaka, Bangladesh, in 2011. He received his M.Sc. and Ph.D. degree from the department of Electrical and Computer Engineering at North Carolina State University, Raleigh, NC in 2014 and 2018, respectively.

From 2011 to 2012, he worked as a quality control engineer at The Smart Solar Inc, Sendai, Japan. Since joining the North Carolina State University, Raleigh, NC in 2013, he is working as research assistant in the NSF FREEDM Systems Center. During his Ph.D. study he also worked for Tabuchi Electric as a research engineering intern during the summer of 2015 and 2016. His general research interests lie in the area of integration of power systems and power electronics engineering. His research spans smart microgrid system, distributed renewable electric energy conversion, energy storage dynamics and optimization, energy management system, ‘plug-and-play’ residential solar system, and microgrid modeling.

ACKNOWLEDGMENTS

I express my deepest gratitude to my advisors Drs. Iqbal Husain and Aranya Chakrabortty for their sincere guidance and advice to pursue my doctoral study. Dr. Husain is a passionate researcher and mentor from whom I learnt to conduct the research in a way that leads to a meaningful contribution. Dr. Chakrabortty is a dedicated adviser whose continuous guidance and assistance were essential to the completion of this research. I would also like to thank my dissertation committee members, Dr. Wensong Yu and Dr. Andre Mazzoleni for their valuable suggestions and support. I also thank Dr. Rafael Cisneros Montoya for his guidance during the last year of my PhD.

I would also like to thank all the faculty, students and staffs working at the NSF FREEDM Systems center for providing tremendous support and encouragement since I joined here in 2013. A special thanks goes to Karen Autry for her endless support to make my life easier from the very first day in the center. I would also like to thank Alireza Afiat Milani for being a great friend and partner in our microgrid system modeling and control research. I would like to thank Ritwik Chattopadhyay and Gregory Norris for their every suggestion and help in the experimental work.

I would like to acknowledge my father Md. Mainur Rahman Khan, my mother Bilkis Khan, and my younger brother Md. Ayubur Rahman Khan for their unconditional support, care and encouragement. Finally, I would like to thank my loving wife Riyana Ayub for all the sacrifices she made for a successful completion of my study. Her appreciation, faith and continued patience provided me the moral strength and inspiration during all these years. And I thank the Almighty for blessing me much more than I deserve.

TABLE OF CONTENTS

LIST OF TABLES

LIST OF FIGURES

CHAPTER 1
INTRODUCTION

1.1. Research Background

1.2. Research Motivation

1.3. Contribution

1.4. Dissertation Outline

1.1. Research Background

Renewable energy integration is increasing steadily in residential and commercial entities due to the reduced system cost and increased reliability and performance. System cost of onshore wind and solar photovoltaic (PV) have reduced by 14% and 61%, respectively since 2009 [1]. Annual growth rate of all the renewable energy resources (RES) are increasing since 2010 with a growth rate of 42% for solar PV from the end of 2010 to the end of 2015 [2]. Exceptional growth rate with advancement in the technology drives European Union (EU) to set an exemplary goal of generating 50% of the energy by RES within 2030 [3]. United States of America (USA) also targets to increase the share of RES more than triple in the energy mix by 2030, from 7.5 % to 27% [4]. RES share is expected to rise to 50% in US power sector with right policies and advancement in technology.

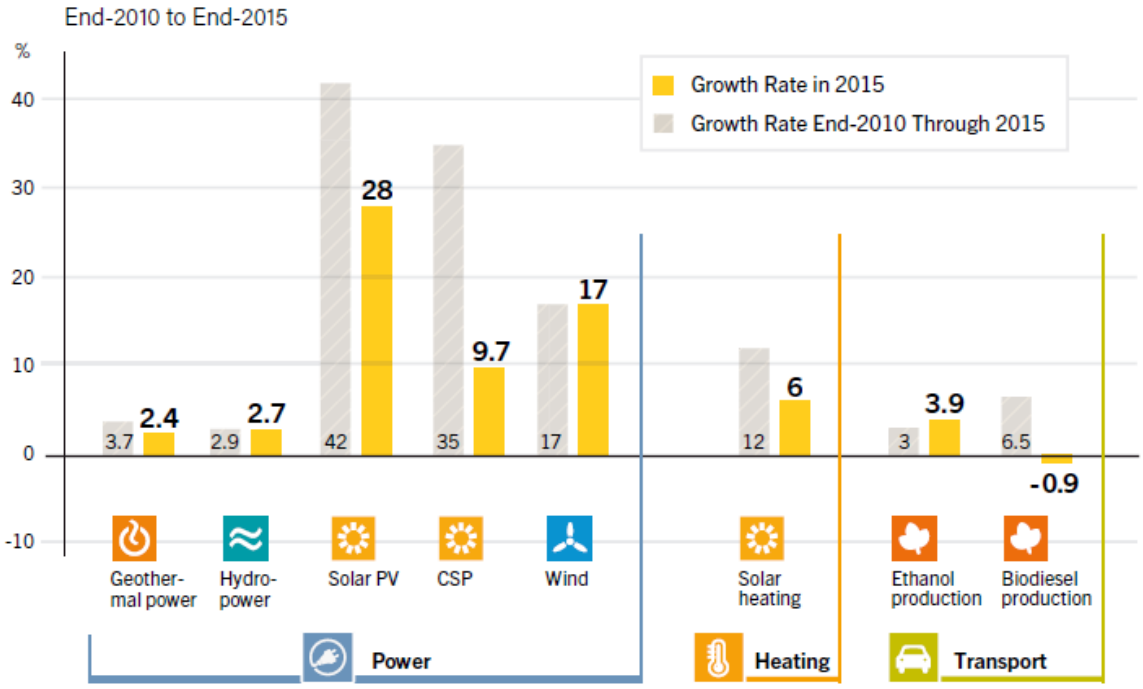

Figure 1.1. Average annual growth rates of renewable energy [1].

Microgrid (MG) based integration of RES will be the prime factor to achieve the 2030 renewable energy target of USA. Particularly, providing power in the off grid locations through MG structure where conventional electricity is expensive compared to RES has the biggest prospect in near future. Even, in the on-grid locations, advanced MG has all the capability to improve the power quality and assist the traditional power grid during any kind of natural calamities [5]. MG based installations are getting notable interest in the recent years due to various benefits like power quality improvement, reactive power compensation and controlling the voltage fluctuation [6]. However, increasing trend of MG system also comes with a separate set of problem with grid voltage disturbance due to the higher penetration during the off-peak hours [7]. The generation from the renewables are maximum during the daytime when the load demand is the lowest, and increasing injection from the RES to the grid leads to an unbalanced voltage condition. Numerous researches have been conducted over the years to solve this critical problem and multiple solutions are proposed [8, 9, 10, and 11]. Recent trend of research and market application bring the focus on the storage application to support the voltage disturbances from RES [12, 13, 14, and 15]. Storage with added cost has the potential to mitigate the penetration issues caused by the renewable energy and no power curtailment will be necessary [16]. Utilities across the USA are already installing large scale energy storage system to support the grid functionalities and residential market is growing, as well [17, 18]. As it is obvious, the system dynamics and control get further complicated as the storage and RES tied together requiring buffering capability by the distribution transfer to balance any unexpected changes in the system. Traditionally, automatic generation control (AGC) adjusts the power output of multiple generators at different power plants to buffer the changes in the customer side through the

distribution transformer [19]. Although, AGC based control works excellent for the traditional generation system, it does not work efficiently with MG based systems where generation capability exists at the distribution end with integrated energy storage with RES [20]. Besides, traditional distribution transformer is incapable of improving power quality issues such as power factor correction, harmonics injection, and volt-var control. Recent development of the Future Renewable Electric Energy Delivery and Management (FREEDM) power distribution system provides an excellent opportunity to integrate RES with the storage and eliminates the usage of low frequency distribution transformer [21]. The Future Renewable Electric Energy Delivery and Management (FREEDM) power distribution system is designed to facilitate distributed renewable generation with energy storage and 'plug-and-play' (PnP) interface of these components. The one-node FREEDM system consists of a solid-state transformer (SST), a DC energy cell and an AC energy cell on the low voltage side of the distribution system [22]. SST serves as an energy router to enable flexible energy sharing among consumers in a residential distribution system where energy cells connected in SST consist of Distributed Renewable Energy Resources (DRERs), Distributed Energy Storage Devices (DESDs) and local loads. The renewable generation sources and the storage devices are enabled to be 'plug-and-play' types with the help of power electronic converter stages between these devices and the system nodes. SST in its role as an energy router enables integration of microgrid components with the traditional grid acting both as an energy management unit and a buffer between the Medium Voltage (MV) grid and the Low Voltage (LV) distribution side where local generations, storages and loads are located [23]. Numerous researches have been conducted about the functionalities and application of SST in distribution system, however, comprehensive system level study

relating the operational constraints put together by the physical parameters were not studied before [24, 25, 26, and 27]. SST based distribution system has been studied in a distribution model and failures are observed under certain conditions, however the reasons behind the failures are unknown [28]. No study has either been reported about the system feasibility or equilibrium analysis which might lead to the system failure in a distribution network. The average model and control scheme of the three stages (rectifier, dual active bridge and inverter) of SST are developed with system level simulation results, though it did not include the energy cells in the average model which is important for dynamic system analysis [23]. PV, wind and storage have their own dynamics and those are required to include in the average model to analyze the system comprehensively. Average model of the FREEDM system also provides an opportunity to analysis system level dynamics and interaction among the multiple of these. Multiple SST operation in a typical distribution system to demonstrate the power sharing capability of AC and DC microgrid were not also analyzed previously. It is critical to study such functionalities to get the full advantages out of a microgrid system. Dynamic control of the DRER and DESD for an optimized and flexible operation is also critical which has been considered in this dissertation besides developing the comprehensive analytical model for microgrid system with power sharing capability. FREEDM system will be mostly operated in the residential neighborhood and getting the PV system installed in such places are highly inefficient due to the various processes involved. This dissertation also investigates the present procedures those are followed for residential PV system installations and a novel PnP method has been proposed as a solution.

1.2 Research Motivation:

Rapid developments of power electronic devices allow the utilization of high frequency pulse-width modulation (PWM) converters like SSTs at the distribution level to interface the renewable resources into the traditional grid [29, 30]. SST is a three stage power converter that offers three key technologies: 'plug-and-play' interfaces at LVDC and LVAC, works as an electric energy router, and implements distributed communication and control protocol, without using a 60 Hz conventional transformer. The SST has three power electronics stages to interface MVAC in the distribution grid with both LVDC and LVAC. These three conversion stages are: Rectifier, Dual Active Bridge (DAB) and Inverter. The rectifier stage converts MVAC power into MVDC power which is then processed by the DAB to convert the MVDC output into lower voltage levels. The DAB is essentially a DC-DC converter with a high frequency transformer. The inverter converts LVDC into LVAC for the AC energy cell applications [21]. Besides efficient operation with much smaller size and lower mass potentials compared to an iron core traditional 60Hz distribution transformer, the SST offers features like power factor correction, instantaneous voltage regulation, voltage sag tolerance, and harmonic isolation [31, 32]. SST makes the system more energy efficient by assisting with power quality improvement at the distribution level (residential users and industry customers) and prioritizing the usage of different types of energy sources to use maximum possible green energy [29]. The overall controller complexity increases for the SST interfaced power distribution system with the possibility of many additional services and also because of the presence of several highly nonlinear power electronics based circuits throughout the system [33, 34, and 35]. Physical parameters of the interface converters (SST) pose operations bounds, coming from the non-linear nature of the power converters which is

essential to study from a theoretical perspective. Knowledge about the operation bounds is necessary to guarantee feasibility of the system by setting appropriate setpoints for every sub-system. Multiple power transformers can also be connected in radial/tree configurations where neighboring transformers can support the change of load in any transformer through adjusting their input power from grid. In order to find the operational bounds of a multi-SST power distribution system for defining the power sharing capability, feasibility analysis for a single SST system is required to perform using its nonlinear dynamic model. Derived feasible bounds will assist the controller to generate appropriate operating points for power balancing among the neighbors. The analysis is conducted in this dissertation for multi-SST system to address the question of "how to choose the setpoints for every SST in the system to maintain the feasibility of the total system".

Moreover, there is no well-defined methods for power sharing between multiple SST systems in the power grid considering the physical constraints coming from the model, itself. In case of change in the load of a SST, the setpoints for every SST can be recalculated according to the feasible bounds of the system. This research also takes into the consideration of appropriate control of the storage system in the MG to support the proposed power sharing methods. Traditionally, storages are controlled from the operational requirements, no initiatives are taken to design coordinated storage control based on system operational bounds and sharing capability [36, 37, and 38]. Eventually, dynamic control of storage will assist the grid operators to maintain the grid stability and support the power sharing within a MG network. To demonstrate the storage control and power sharing capability, a distribution test bed based on IEEE 34 bus system is built and then, different case studies are studied to verify the system design and power sharing concept.

Along with the storage, PV system is another integral part of the FREEDM system for a flexible and efficient operation. PV installations in both residential and commercial sectors have increased rapidly throughout the world in the last decade primarily because of the technical advancements and hardware cost reduction. However, challenges remain in the installation and permitting process and the cost is not yet competitive enough for mass adoption. The focus has shifted in recent years to reduce the complexities of PV system installation and streamlining the permitting process. Hardware cost reduction has likely reached limits and only way to reduce cost further is through reduction in soft costs such as installation, permitting and inspection. This research discusses the barriers in making the PV system 'plug-and-play' (PnP) for residential applications, and then, presents a PV utility interface (PUI) concept that includes a hardware between the grid and the PV panel and a web portal to bring together all the stake holders for simpler installation and commissioning. A cost comparison for a practical implementation of such a system is discussed and a real-time demonstration is also conducted with the developed hardware for a full system installation.

1.3 Contribution:

Key contributions from this dissertation are listed below:

1. 70^{th} order FREEDM system model has been developed that includes the SST, PV, wind generator and storage. The developed model is critical for the analytical analysis of the FREEDM system to find the practical operational bounds of such a power distribution system.
2. Feasible operation bounds are developed and verified in a distribution network for the first time for FREEDM system. The bounds will guarantee practical system design

for a wider range of operation and are related to load demand, location of the transformer and parameters.

3. Novel power sharing methods have been proposed and verified for multiple SST based power distribution network. This methods has all the potentials to redefine the system integration of the renewables and storage for a smart grid operation.
4. Decentralized dynamic controller for energy storage is developed considering feasible operation bounds to maintain net load constant over a particular period through local support and power sharing in FREEDM system.
5. A novel automation device for the residential PV system installations is designed and hardware is developed for a real-time testing. The developed device has a potential of cost reduction of $0.3/watts for residential PV system along with a 95% reduction of installation time.

1.4 Dissertation Outline:

Chapter 2:

Nonlinear 70th FREEDM system model has been developed that includes a single SST along with PV, wind generators and storage in both the DC and AC energy cells. The modeling approach has been carried out for the full system with energy cells to develop a physics based comprehensive model and results have been extended to develop the feasibility constraints for a simplified FREEDM model. Surface plots of various conditions are observed to study the system constraints and then, a distribution network is built to verify the developed model for a system level simulation. Case studies for various combination of storage and renewables have been studied; this chapter is accepted for publication in IEEE Energy

Conversion Congress and Expo (ECCE)'2016 and in the IEEE journal of Transactions of Industrial Society (IAS) [39, 40].

Chapter 3:

Based on the average model and detailed feasibility analysis of the single SST, feasibility constraints are found and those are further analyzed for the multiple SST system in a tree configuration. The multi-SST constraint provides the relationship of physical parameters of SST with the coupling terms (tie-line impedance) that is utilized to develop the power sharing method among the neighboring SSTs. Two different methods are proposed and simulated by maintaining the node voltage or input current constant for a 3-SST validation model. Case studies from the power sharing methods lead to the formulation of Intelligent Power Management (IPM) and Intelligent Energy Management (IEM) controller design for multi-SST system. This chapter is a part of the publication that has been published in the IEEE journal of Transactions of Power System (TPWRS) [41].

Chapter 4:

Storage plays an important role in the FREEDM system and dynamic storage controller considering the multi-SST power sharing methods will add operational benefits to MG network. Decentralized energy storage controller is developed based on input-output linearization method to maintain the net load constant through local support and enable power sharing methods for multi-SST support. The controller is verified in IEEE 34 bus based nine SST systems; this chapter is drafted to submit in IEEE TPWRS journal.

Chapter 5:

Large scale system simulation (LSSS) testbed based on the modified IEEE 34 bus has been built to analyze the feasibility analysis developed in chapter two. The simulation verifies the developed bounds from the dynamic model and then, subsequent analysis is also performed to get rid of the system failure due the feasibility in a distribution network. This part of the research also investigates the storage and renewable combined operation in IEEE 34 bus based distribution system to implement the power sharing methods in chapter three. Part of this chapter has been published in IEEE journal of IAS [40].

Chapter 6:

PV system is another critical component of the FREEDM system based distribution network and this chapter provides an automated installation solution for PnP system. PV is one of the biggest players of renewable energy installations although the soft costs remain as concern for higher penetration of solar energy. To address the soft cost challenges, PnP system for a quick, low-cost installation is proposed and designed with emphasis on the controls, software, and system level communications within the system. PUI is the developed hardware out of this research for this automation purposes and it will expedite the process of PnP integration of PV system with SST. The developed hardware will reduce residential PV system price by $0.3/watt and the installation time by 95% compared to the present procedures. This chapter is a compilation of two conference papers published in ECCE'2014 [42], ECCE'2015 [43] and a journal paper that has been accepted to publish in the IEEE journal of IAS [44].

Chapter 7:

Overall contributions from this dissertation and future works are summarized in this chapter.

CHAPTER 2

DYNAMIC MODELING AND FEASIBILITY ANALYSIS OF A SOLID-STATE TRANSFORMER BASED POWER DISTRIBUTION SYSTEM

2.1. Introduction

2.2. Detailed Modeling of FREEDM System

2.3. Case Studies with the Developed Average Model

2.4. Feasibility and Stability Surface Plots Based on Rectifier Model

2.5. Contribution

2.6. Conclusions

2.1. Introduction

This chapter presents a physics based comprehensive dynamic model of a future power distribution system, termed as the FREEDM system, for 'plug-and-play' interface of distributed renewable energy resources and distributed energy storage devices. The system allows for high penetration of renewable generation with energy storage at the distribution level. FREEDM system consists of an energy router, which is the power electronics SST that interfaces distributed generation, storage and local loads on the low voltage side with the medium voltage node of the distribution grid. The one-node FREEDM system consists of a solid-state transformer (SST), a DC energy cell and an AC energy cell on the low voltage side of the distribution system as shown in Fig. 2.1. These energy cells consist of DRERs, DESDs and local loads. SST in its role as an energy router enables integration of energy cell components with the traditional grid acting both as an energy management unit and a buffer between the MV grid and LV distribution side where local generations, storages and loads are located. The tremendous advancements in power electronics and converter control techniques make it possible to utilize the SST and other power electronic interfaces at the distribution level [29]. The SST has three power electronics stages to interface MVAC in the distribution grid with both LVDC and LVAC. These three conversion stages are: Rectifier, Dual Active Bridge (DAB) and Inverter as shown in Fig. 2.2. The rectifier stage converts MVAC power into MVDC power which is then processed by the DAB to convert the MVDC output into lower voltage levels. The DAB is essentially a DC-DC converter with a high frequency transformer. The inverter converts LVDC into LVAC for the AC energy cell applications [23, 45]. SST makes the system more energy efficient by assisting with power quality improvement at the distribution level (residential users and industry customers) and

prioritizing the usage of different types of energy sources to use maximum possible green energy [26]. The overall controller complexity increases for the SST interfaced power distribution system with the possibility of many additional services and also because of the presence of several highly nonlinear power electronics based circuits throughout the system. Prior research focused on developing analytical models of only SST without considering the renewable generation and storage components and their physical constraints or interactions with the SST [23, 25, and 27]. In this chapter, state-space modeling and dynamic performance of the SST is analyzed along with the renewable generation sources and storage components with the goal of studying the feasible operating points of the FREEDM system. The objective of this chapter is to develop a comprehensive dynamic model of the FREEDM power distribution system for feasibility analysis and multi-level controller development for reliable and resilient operation of the system. The actual model of the single-SST system amounts to highly complex dynamics with more than hundred state variables. Singular perturbation based model reduction techniques are applied, thereby leading to a 70^{th} order state-space average model suitable for AC and DC energy cell system sizing, stability analysis, and controller design. The analysis with the system model reveals the SST input stage system parameters have the dominant effect on the feasible operation region.

2.2. Detailed Modeling of FREEDM System

The FREEDM system consists of SST, DRER, DESD and local loads that makes its overall dynamics nonlinear in nature. The end-to-end comprehensive mathematical model has been developed capturing all the nonlinear, and sometimes non-smooth, dynamic phenomena triggered by different types of switching command, and disturbances within a FREEDM

system. Due to the nonlinearities in the FREEDM system, the modeling process starts with building sub-system state-space models, such as those for SST, Wind DRER, PV DRER and DESD. The sub-system models are then integrated to build the comprehensive FREEDM system model. The component states and the associated controller states are also separated such that the plant model and the controller model can be developed and upgraded individually. The functional diagram representing the FREEDM system that includes SST and other sub-systems considered for the modeling purpose are shown in Fig. 2.1. In Fig. 2.2, all the parameters and physical states are shown by a_i and x_i, respectively; PI controller states are denoted by ξ_i; and d_i's are the output of the controllers. DAB output current is denoted by I_{DAB}, rectifier net output power is presented by P_{rec}, while L_{DC} and L_{AC} represent the net load of DC and AC energy cells (generation sources, energy storage and local loads), respectively. The time-scales of evolution of the different states, however, are sharply different ranging from 10^{-3} microseconds to 0.1 seconds within SST. Singular perturbation techniques have been applied to reduce the model order, and represent it in a more tractable form. Singular perturbation method separates the dynamic system into slow and fast variables that allow the simplification of the rectifier model by eliminating the states those have no effects on system performance [46]. Total system states have been reduced from more than hundreds for the full FREEDM system by utilizing the singular perturbation technique and that makes the system analysis simpler. The final order of the simplified derived model, including all internal controller states, is seventy.

2.2.1 SST - Rectifier Model and Controllers

The rectifier is the connection point of the SST, and more generally the FREEDM system to the grid. The modeled rectifier has an LCL filter at the front end which is simplified to

represent an L-rectifier through model reduction. In a dual loop controller, the rectifier output voltage is controlled in the outer loop that generates the *d*-axis current reference for controlling the i_d-component of the SST input current in the inner loop. Current reference can be set to zero for unity power factor in the *q*-axis controller that controls the reactive power flow.

Fig. 2.2 shows the simplified circuit diagram of the rectifier and the equations (2.1)-(2.10) present the rectifier physical states, controller states and controller output where y_1, y_2, $x_1$and x_2 represent *d* and *q*-axes grid voltages and currents, respectively. All the parameters and states are enlisted in table 1.1.

$$\dot{x}_1 = -\frac{a_2}{a_1}x_1 + \omega_1 x_2 + \frac{1}{a_1}d_1 x_3 - \frac{1}{a_1}y_1 \tag{2.1}$$

$$\dot{x}_2 = -\omega_1 x_1 - \frac{a_2}{a_1}x_2 + \frac{1}{a_1}d_2 x_3 - \frac{1}{a_1}y_2 \tag{2.2}$$

$$\dot{x}_3 = -\frac{1}{2a_3}d_a x_a - \frac{P_{rec}}{a_3 x_3} \tag{2.3}$$

d_a and x_a can be found using equations (2.4-2.5) through inverse *dq-αβ* modeling and the phase output (θ) from the phase locked loop (PLL) block. PLL synchronizes with the input voltage of the SST such that accurate phase of the AC voltage can be detected. Output DC voltage of the rectifier has to capture the AC side frequency in the DC side and considering equation (2.3) will guarantee that. Eventually, this model can be used for the validation with the switching model also.

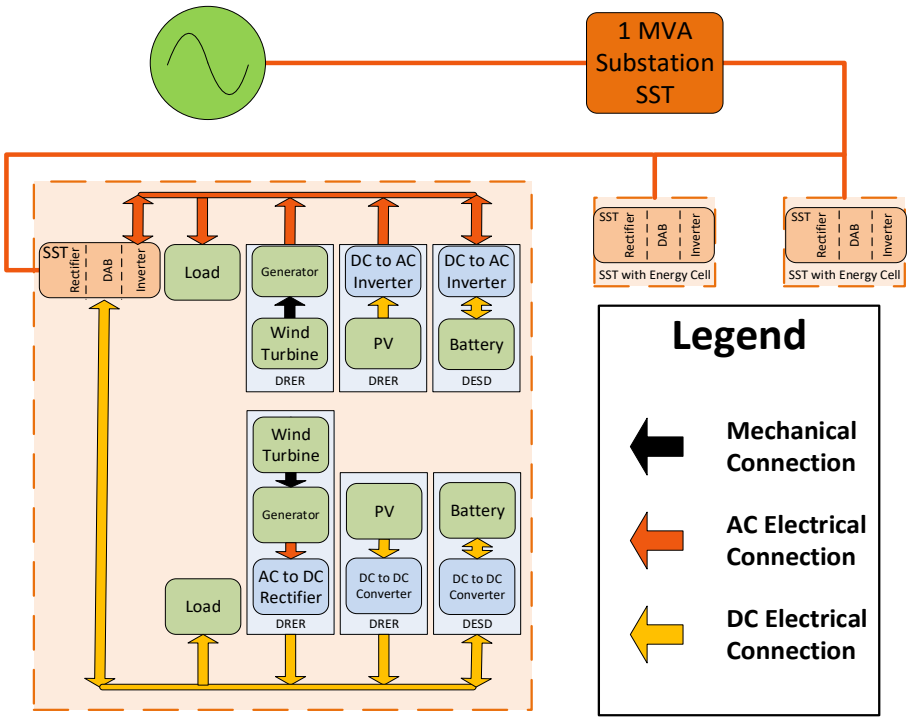

Figure 2.1. One node FREEDM system model.

$$d_a = d_1 \cos(\theta) + d_2 \sin(\theta) \tag{2.4}$$

$$x_a = x_1 \cos(\theta) + x_2 \sin(\theta) \tag{2.5}$$

$$\dot{\xi}_1 = r_1 - x_3 \tag{2.6}$$

$$\dot{\xi}_2 = a_4(r_1 - x_3) + a_5\xi_1 - x_1 \tag{2.7}$$

$$\dot{\xi}_3 = q_1 - x_2 \tag{2.8}$$

$$d_1 = a_6(a_4(r_1 - x_3) + a_5\xi_1 - x_1) + a_7\xi_2 \tag{2.9}$$

$$d_2 = a_8(q_1 - x_2) + a_9\xi_3 \tag{2.10}$$

2.2.2 SST - DAB Model and Controllers

The DAB consists of two full bridges and a high frequency transformer in between these bridges. In order to be able to transfer the power from the first bridge to the second one, phase difference must exist between the switching of these bridges. The states of the system

are input and output capacitor voltages and inductor current. However, the system can be divided into a slow-varying system and a fast-varying system since the capacitor voltage changes are much slower compared to the changes in inductor current [47, 48].

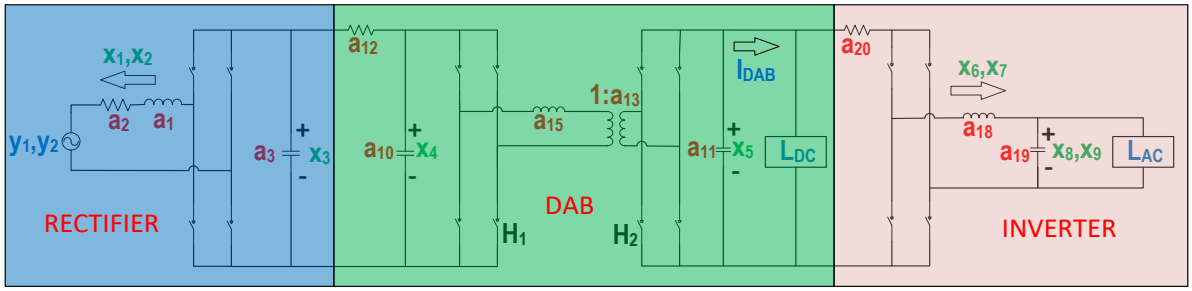

Figure 2.2. Solid-state transformer circuit model.

The two-dimensional representation of the DAB converter is obtained by linearly representing the fast-varying inductor current in each sub-interval and applying the state-space averaging method. Equations (2.11) - (2.14) provide the final state models for DAB along with the controller output.

$$\dot{x}_4 = +\frac{1}{a_{10}a_{12}}x_3 - \frac{1}{a_{10}a_{12}}x_4 - \frac{\phi_3(1-\phi_3)a_{13}}{2a_{10}a_{14}a_{15}}x_5 \tag{2.11}$$

$$\dot{x}_5 = \frac{\phi_3(1-\phi_3)a_{13}}{2a_{11}a_{14}a_{15}}x_4 - \frac{1}{a_{11}L_{DC}}x_5 \tag{2.12}$$

$$\dot{\xi}_4 = r_2 - x_5 \tag{2.13}$$

$$\phi_3 = a_{16}(r_2 - x_5) + a_{17}\xi_4 \tag{2.14}$$

2.2.3 SST - Inverter Model and Controllers

In the inverter stage, the AC inverter controls the magnitude of the output side AC voltage in the *dq* reference frame to interface with the AC energy cell. An inner current loop can be added to track the voltage references faster. The inverter circuit diagram is shown in Fig. 2.2. Inverter state equations, controller states and outputs are given in equations (2.15) - (2.22),

where x_6, x_7, x_8 and x_9 represent d and q -axes inverter output currents and voltages, respectively.

Table 2.1. FREEDM system parameter list.

System and Controller States							
x_1	Rectifier d-axis inductor current	x_7	Inverter q-axis inductor current	$x_{25} - x_{30}$	DC DESD interface converter states	ξ_{13}	DC DRER interface converter controller state
x_2	Rectifier q-axis inductor current	x_8	Inverter d-axis capacitor voltage	$\xi_1 - \xi_3$	Rectifier controller states	ξ_{14}	DC DESD interface converter controller states
x_3	Rectifier capacitor voltage	x_9	Inverter q-axis capacitor voltage	ξ_4	DAB controller state		
x_4	DAB input capacitor voltage	$x_{10} - x_{15}$	AC DRER interface converter states	$\xi_5 - \xi_6$	Inverter controller states		
x_5	DAB output capacitor voltage	$x_{16} - x_{21}$	AC DESD interface converter system states	$\xi_7 - \xi_{10}$	AC DRER interface converter controller states		
x_6	Inverter d-axis inductor current	$x_{22} - x_{24}$	DC DRER interface converter states	$\xi_7 - \xi_{10}$	AC DESD interface converter controller states		
System Parameters							
a_1	Rectifier filter inductor	a_{11}	DAB output capacitor	a_{19}	Inverter filter capacitor	$a_{46} - a_{47}$	DC DRER interface converter controller gains
a_2	Rectifier filter resistor	a_{12}	DAB input resistor	a_{20}	Inverter input filter resistor	$a_{48} - a_{57}$	AC DESD physical parameters
a_3	Rectifier capacitor	a_{13}	Transformer turns ratio	a_{21}, a_{22}	Inverter d-axis gains of controller	$a_{58} - a_{61}$	AC DESD interface converter controller gains
a_4, a_5	Rectifier gains of voltage controller	a_{14}	Transformer switching frequency	a_{23}, a_{24}	Inverter q-axis gains of controller	$a_{62} - a_{75}$	DC DESD physical parameters
a_6, a_7	Rectifier d-axis gains of controller	a_{15}	Transformer inductor	$a_{25} - a_{33}$	AC DRER physical parameters	$a_{76} - a_{77}$	DC DESD converter controller gains
a_8, a_9	Rectifier q-axis gains of controller	a_{16}, a_{17}	DAB PI controller gains	$a_{34} - a_{41}$	AC DRER interface controller gains		

Table 2.1 Continued

a_{10}	DAB input capacitor	a_{18}	Inverter filter inductor	$a_{42} - a_{45}$	DC DRER physical parameters		
System References							
ω_1	Rectifier frequency	L_{AC}	Inverter net output load (Ohms)	r_3	Inverter d-axis reference voltage	r_7	DC DRER maximum power point voltage
ω_2	Inverter frequency	q_1	Rectifier q-axis reference current	r_4	AC DRER converter reference voltage	r_8	DC DRER maximum power point power
P_{rec}	Rectifier net output power	r_1	Rectifier output reference voltage	r_5	AC DRER maximum power point voltage	r_9	AC DESD charging/ discharging current reference
L_{DC}	DAB net output load (Ohms)	r_2	DAB output reference voltage	r_6	AC DRER maximum power point power	r_{10}	DC DESD charging/ discharging current reference
Control Outputs							
d_1	Rectifier d-axis converter duty cycle	d_4	Inverter d-axis converter duty cycle	$d_6 - d_8$	AC DRER converter duty cycles	d_{11}	DC DRER converter duty cycle
d_2	Rectifier q-axis converter duty cycle	d_5	Inverter q-axis converter duty cycle	$d_9 - d_{10}$	AC DESD converter duty cycles	d_{12}	DC DESD converter duty cycle
ϕ_3	DAB converter phase shift ratio						

$$\dot{x}_6 = \frac{1}{a_{18}} d_4 x_5 - \frac{a_{20}}{a_{18}} x_6 + \omega_2 x_7 - \frac{1}{a_{18}} x_8 \tag{2.15}$$

$$\dot{x}_7 = \frac{1}{a_{18}} d_5 x_5 - \omega_2 x_6 - \frac{a_{20}}{a_{18}} x_7 - \frac{1}{a_{18}} x_9 \tag{2.16}$$

$$\dot{x}_8 = \frac{1}{a_{19}} x_6 - \frac{1}{a_{19} L_{AC}} x_8 + \omega_2 x_9 \tag{2.17}$$

$$\dot{x}_9 = \frac{1}{a_{19}} x_7 - \omega_2 x_8 - \frac{1}{a_{19} L_{AC}} x_9 \tag{2.18}$$

$$\dot{\xi}_5 = y_3 - x_8 \tag{2.19}$$

$$\dot{\xi}_6 = y_4 - x_9 \tag{2.20}$$

$$d_4 = a_{21}(y_3 - x_8) + a_{22}\xi_5 \tag{2.21}$$

$$d_5 = a_{23}(y_4 - x_9) + a_{24}\xi_6 \tag{2.22}$$

2.2.4 DRER Model and Controllers

Both the DC and AC energy cells have similar components on the LV side consisting of a PV DRER, Wind DRER, one DESD and a load. The difference in the DC and AC energy cells is in the power electronics interface circuits connecting them to the DC and AC buses. Each component along with its coupling on both the DC and AC energy cells have been modeled separately to capture the detailed physical characteristics which were missing in previous studies. Both PV and wind DRERs have been considered for generality in the FREEDM system, although in reality, only one type is expected to be present in an energy cell. The physics based PV model has been focused in this paper; where the parameters of the nonlinear *I-V* equation is found by adjusting the curve at three points: open circuit, maximum power, and short circuit [49, 50]. The rectifier and inverter average models of the DRERs are matched with the average model of SST's rectifier and inverter to maintain consistency in modeling. Mathematical models and interface circuits of the PV DRERs for both the AC and DC energy cells are provided in the next paragraph. Fig. 2.3 presents the PV DRER interface circuit for AC energy cells. Boost converter is coupled with rectifier circuit to convert the lower DC voltage of the PV system to lower AC voltage. DRER circuit is directly connected to the AC bus through the interface circuit. Mathematical model for the interface is also developed and shown in equations (2.22)-(2.35). The control objective of this model to inject maximum the PV DRER output current to the AC bus voltage. Fig. 2.4 shows the PV DRER interface circuit for DC energy cells. PV panels are directly connected with boost converter

to amplify the panel voltage to DC bus voltage. Based on voltage level of the panels, other DC-DC converters can also be coupled for the interface. Mathematical model for the interface is also developed and shown in equations (2.36)-(2.40).

$$\dot{x}_{10} = \frac{1}{a_{25}} x_{11} - \frac{1-d_6}{a_{25}} x_{12} \tag{2.23}$$

$$\dot{x}_{11} = -\frac{1}{a_{26}} x_{10} + \frac{1}{a_{26}} \frac{u_2}{x_{11}} \tag{2.24}$$

$$\dot{x}_{12} = \frac{1-d_6}{a_{27}} x_{10} - \frac{1}{a_{27}a_{28}} x_{12} + \frac{1}{a_{27}a_{28}} x_{15} \tag{2.25}$$

$$\dot{x}_{13} = -\frac{1}{a_{31}} x_8 - \frac{a_{33}}{a_{31}} x_{13} + \omega_2 x_{14} + \frac{1}{a_{31}} d_7 x_{15} \tag{2.26}$$

$$\dot{x}_{14} = -\frac{1}{a_{31}} x_9 - \omega_2 x_{13} - \frac{a_{33}}{a_{31}} x_{14} + \frac{1}{a_{31}} d_8 x_{15} \tag{2.27}$$

$$\dot{x}_{15} = -\frac{1}{2a_{32}} d_7 x_{13} - \frac{1}{2a_{32}} d_8 x_{14} - \frac{1}{a_{32}} \frac{u_2}{x_{15}} \tag{2.28}$$

$$\dot{\xi}_7 = u_1 - x_{11} \tag{2.29}$$

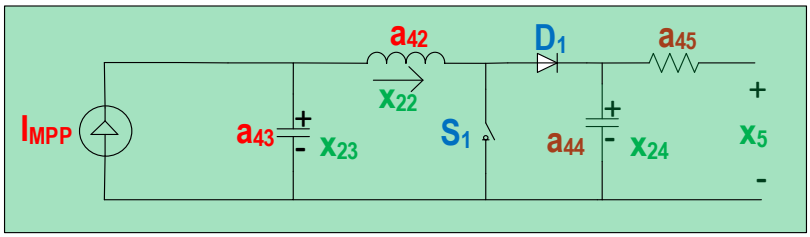

Figure 2.4: PV DRER and boost converter for PV DC interface.

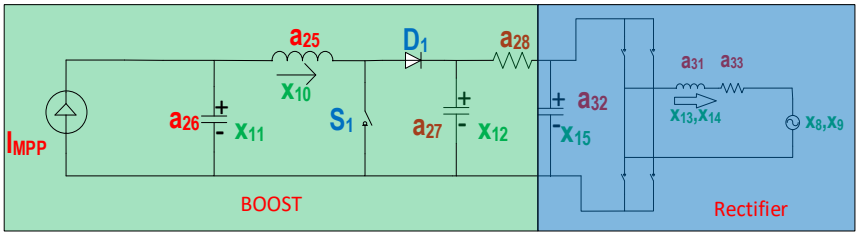

Figure 2.3: PV DRER, boost converter and rectifier for PV AC interface.

$$\dot{\xi}_8 = r_3 - x_{15} \tag{2.30}$$

$$\dot{\xi}_9 = a_{34}(r_3 - x_{15}) + a_{35}\xi_8 - x_{13} \tag{2.31}$$

$$\dot{\xi}_{10} = -x_{16} \tag{2.32}$$

$$d_6 = a_{36}(u_1 - x_{11}) + a_{37}\xi_7 \tag{2.33}$$

$$d_7 = a_{38}(a_{34}(r_3 - x_{15}) + a_{35}\xi_8 - x_{13}) + a_{39}\xi_9 \tag{2.34}$$

$$d_8 = -a_{40}x_{16} + a_{41}\xi_{10} \tag{2.35}$$

$$\dot{x}_{22} = \frac{1}{a_{42}}x_{23} - \frac{(1-d_{11})}{a_{42}}x_{24} \tag{2.36}$$

$$\dot{x}_{23} = -\frac{1}{a_{43}}x_{22} + \frac{u_4}{a_{43}x_{23}} \tag{2.37}$$

$$\dot{x}_{24} = \frac{(1-d_{11})}{a_{44}}x_{22} - \frac{1}{a_{44}a_{45}}x_{24} + \frac{1}{a_{44}a_{45}}x_5 \tag{2.38}$$

$$\dot{\xi}_{13} = u_3 - x_{23} \tag{2.39}$$

$$d_{11} = a_{46}(u_3 - x_{23}) + a_{47}\xi_{13} \tag{2.40}$$

2.2.5 DESD Model and Controllers

The power electronics based interface with bi-directional capability controls the DESD charging/discharging voltage and current for power and energy management of the system. The charging voltage of DESD is typically lower than the DC bus voltage, and hence, a good choice for this interface circuit is a buck converter for the DC energy cell and an inverter coupled buck converter for AC energy cell. However, to allow flexibility in choosing the voltage rating of the battery, a bidirectional buck-boost converter for DC DESD and an inverter coupled with a buck-boost converter is used for AC DESD. Power electronics interface circuits for AC DESD and DC DESD are shown in Fig. 2.5 and Fig. 2.6, respectively. Mathematical models of the AC DESD are given in equations (2.41)-(2.50).

DESD model for the FREEDM system has utilized the detailed storage modeling to capture all the transients [51, 52]. Similar to the DRER, the DESD controller objective is to match the output voltage with AC bus voltage.

$$\dot{x}_{16} = -\frac{1}{a_{48}} x_8 - \frac{a_{50}}{a_{48}} x_{16} + \omega_2 x_{17} + \frac{1}{a_{50}} d_9 x_{18} \tag{2.41}$$

$$\dot{x}_{17} = -\frac{1}{a_{48}} x_9 - \omega_2 x_{16} - \frac{a_{50}}{a_{48}} x_{17} + \frac{1}{a_{48}} d_{10} x_{18} \tag{2.42}$$

$$\dot{x}_{18} = -\frac{1}{2a_{49}} d_9 x_{16} - \frac{1}{2a_{49}} d_{10} x_{17} - \frac{1}{a_{49}a_{51}} x_{18} + \frac{1}{a_{49}a_{51}} * (V_{oc} + x_{20} + x_{21} - x_{18}) \tag{2.43}$$

$$\dot{x}_{19} = -\frac{1}{a_{52}a_{53}} x_{19} + \frac{1}{a_{52}(a_{51} + a_{50})} * (V_{oc} + x_{20} + x_{21} - x_{18}) \tag{2.44}$$

$$\dot{x}_{20} = -\frac{1}{a_{54}a_{55}} x_{20} + \frac{1}{a_{54}(a_{51}+a_{50})} * (V_{oc} + x_{20} + x_{21} - x_{18}) \tag{2.45}$$

$$\dot{x}_{21} = -\frac{1}{a_{56}a_{57}} x_{21} + \frac{1}{a_{56}(a_{51} + a_{50})} * (V_{oc} + x_{20} + x_{21} - x_{18}) \tag{2.46}$$

$$\dot{\xi}_{11} = u_5 - x_{16} \tag{2.47}$$

$$\dot{\xi}_{12} = -x_{17} \tag{2.48}$$

$$d_9 = a_{58}(u_5 - x_{16}) + a_{59}\xi_{11} \tag{2.49}$$

$$d_{10} = -a_{60}a_{17} + a_{61}\xi_{12} \tag{2.50}$$

DC DESD is directly connected to the DC bus and so the rectifier stage is not required. Mathematical models for DC DESD with Buck-Boost converter are provided in equations (2.51)-(2.57).

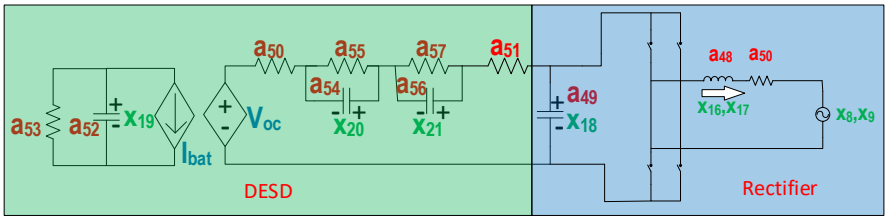

Figure 2.5: DESD and rectifier circuit for AC DESD average model.

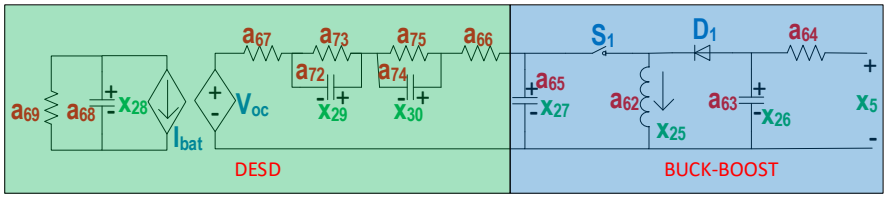

Figure 2.6: DESD and buck-boost circuit for DC DESD average model.

$$\dot{x}_{26} = \frac{1}{a_{63}a_{64}}x_5 - \frac{(1-d_{12})}{a_{63}}x_{25} - \frac{1}{a_{63}a_{64}}x_{26} \tag{2.51}$$

$$\dot{x}_{27} = -\frac{d_{12}}{a_{65}}x_{25} + \frac{(1-d_{12})}{a_{65}(a_{66}+a_{67})} * (V_{oc} + x_{29} + x_{30} - x_{27}) \tag{2.52}$$

$$\dot{x}_{28} = -\frac{1}{a_{68}a_{69}}x_{28} - \frac{1}{a_{68}(a_{66}+a_{67})} * (V_{oc} + x_{29} + x_{30} - x_{27}) \tag{2.53}$$

$$\dot{x}_{29} = -\frac{1}{a_{72}a_{73}}x_{29} + \frac{1}{a_{72}(a_{68}+a_{69})} * (V_{oc} + x_{29} + x_{30} - x_{27}) \tag{2.54}$$

$$\dot{x}_{30} = -\frac{1}{a_{74}a_{75}}x_{30} + \frac{1}{a_{74}(a_{66}+a_{67})} * (V_{oc} + x_{29} + x_{30} - x_{27}) \tag{2.55}$$

$$\dot{\xi}_{14} = u_6 - \frac{(x_5 - x_{26})}{a_{64}} \tag{2.56}$$

$$d_{12} = a_{75}\left(u_6 - \frac{(x_5 - x_{26})}{a_{72}}\right) + a_{76}\xi_{14} \tag{2.57}$$

2.3. Case Studies with the Developed Average Model

Several case studies have been conducted with the developed comprehensive FREEDM system model to evaluate the impact on the output voltage levels in different stages of the system and track performance for the controller setpoints. Results are observed where DC and AC buses are maintained at the set voltage levels with load changes in DC or AC energy cells, start/stop of DRER generation and DESD charging/discharging modes. Summary results of two particular cases are shown in Fig. 2.7. Fig. 2.7 (a) shows that PV generation of 0.5 kW added at t=1 sec from the DC energy cells causes an overshoot in the SST rectifier, DAB and inverter output voltages with energy being fed back to the grid. The energy storage in the charging mode and wind generation unit are connected to the system at t=2 secs and 3.2 secs, respectively. The DC voltage in rectifier and DAB output drops at first, but the controllers are able to maintain the steady-state regulation, also inverter output voltage experiences voltage sag for a shorter time due to faster timescale of the controller. For analyzing the dynamics introduced by the AC energy cell, PV DRER, AC DESD, and wind generation are connected to the system at t=5 secs, 6 secs and 7.2 secs, respectively. Fig. 2.7 (b) shows that the DC bus voltage along with inverter output fluctuates due to addition of the AC energy cell components. Fig. 2.8 shows the system response when the SST operating mode is changed for reversing the power flow with renewable generation and active load reduction. DC bus voltage of the rectifier and DAB show overshoot before settling to the desired regulation points within 0.3 secs.

Fig. 2.9 shows the system response following a 30% voltage sag in the grid voltage from 3.6 kV to 2.52 kV. The controller is able to regulate the output voltage of rectifier, DAB and

inverter with the change in input voltage at t=2 secs. As the DC voltages are regulated precisely, the impact on the inverter output voltage is minimal with grid voltage variations. The system response with variations in output DC load has also been analyzed with the model. Fig. 2.10 shows the response of the regulated voltages after a step change in DC load from 50 ohms to 80 ohms. The controller is able to regulate the output voltage of rectifier, DAB and inverter with the 60% change in active power at t=2 secs. DAB voltage shows a 10% surge due to the step change, but it settles to the regulated voltage of 400 V within 0.15 secs. The robustness of the controller with respect to parameter variation has been verified by changing the filter resistance to observe the impact of physical parameters on controllers. Fig. 2.11 shows the response of the regulated voltage after a step change in input filter resistance of the rectifier from base value of 47 ohms to 80 ohms. The controller is able to regulate the output voltage of rectifier, DAB and inverter with the change in system parameter values at t=2 sec. The rectifier output voltage shows a transient value of less than 0.10% due to the step change; the inverter voltage does not have any noticeable transient. This analysis further shows that the transient voltage responses do not show any significant overshoot/undershoot even with parameter variations up to 80% from base values. It has been found that the rectifier filter resistance determines the feasible operation region of the system which will be further explained in the next section.

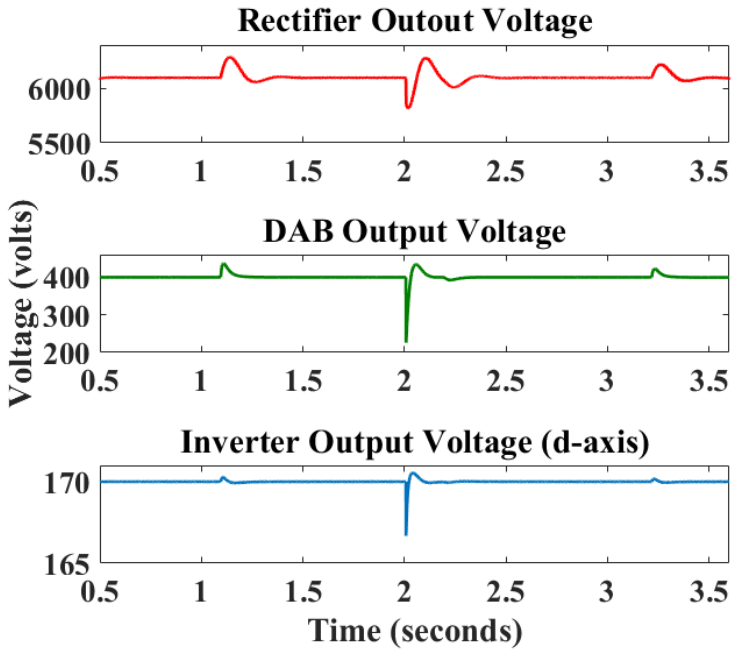

(a)

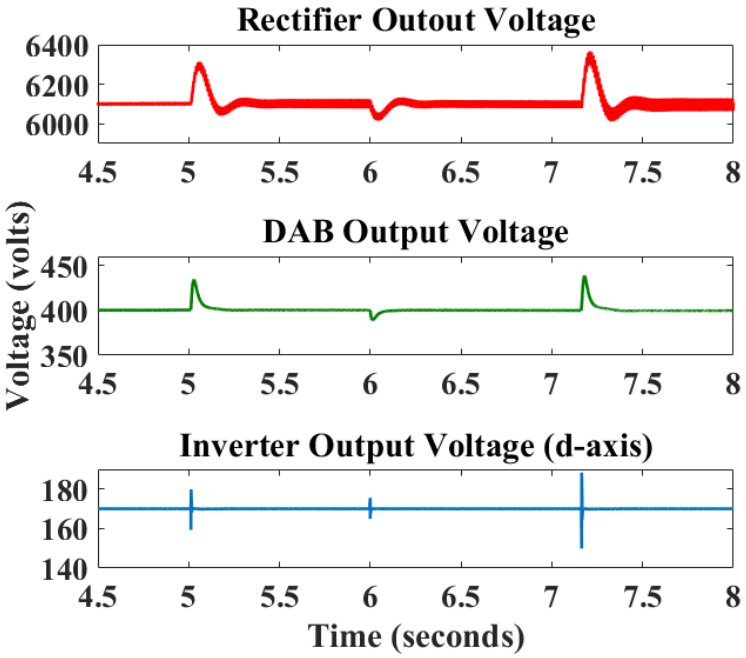

(b)

Figure 2.7: Case studies with 70th order average model.

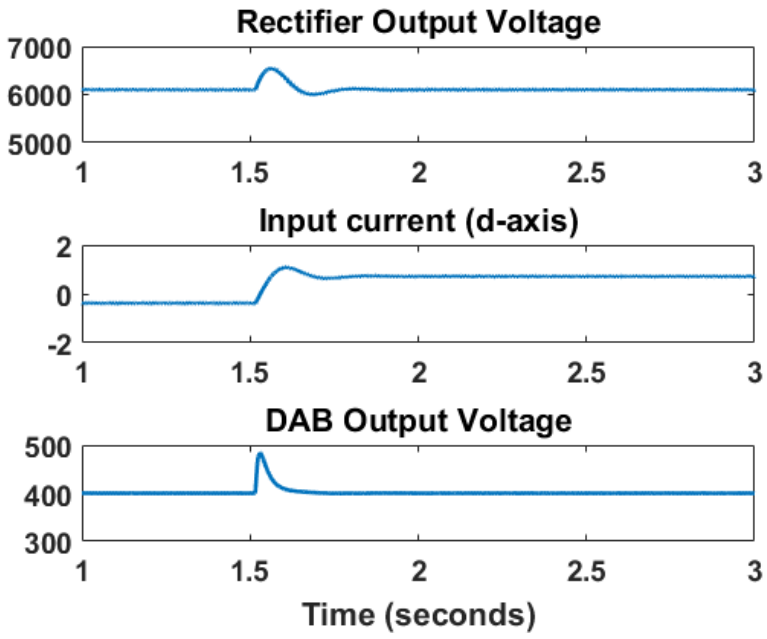

Figure 2.8: Case study with regenerative mode of operation.

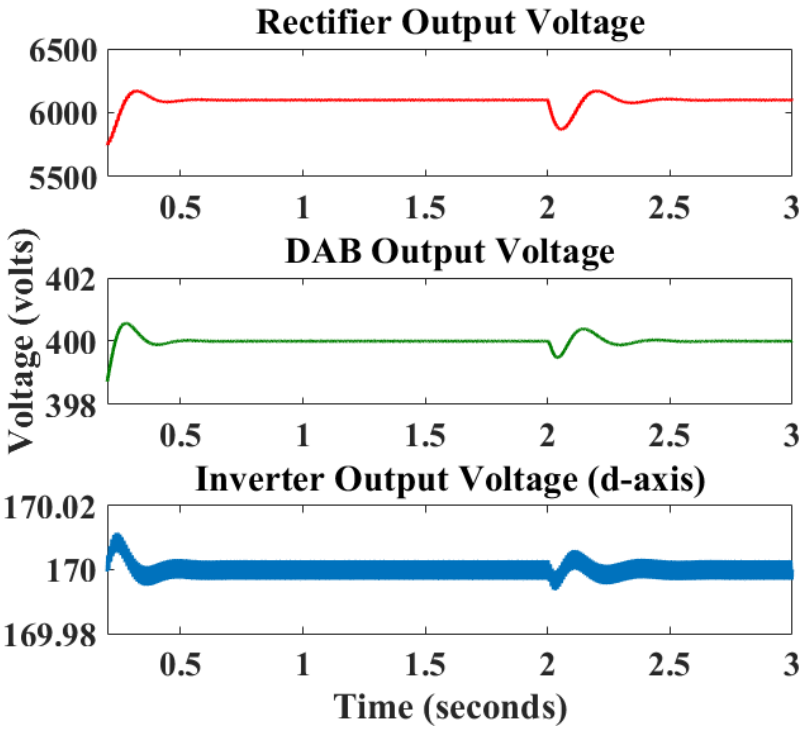

Figure 2.9: Case study with input voltage variation.

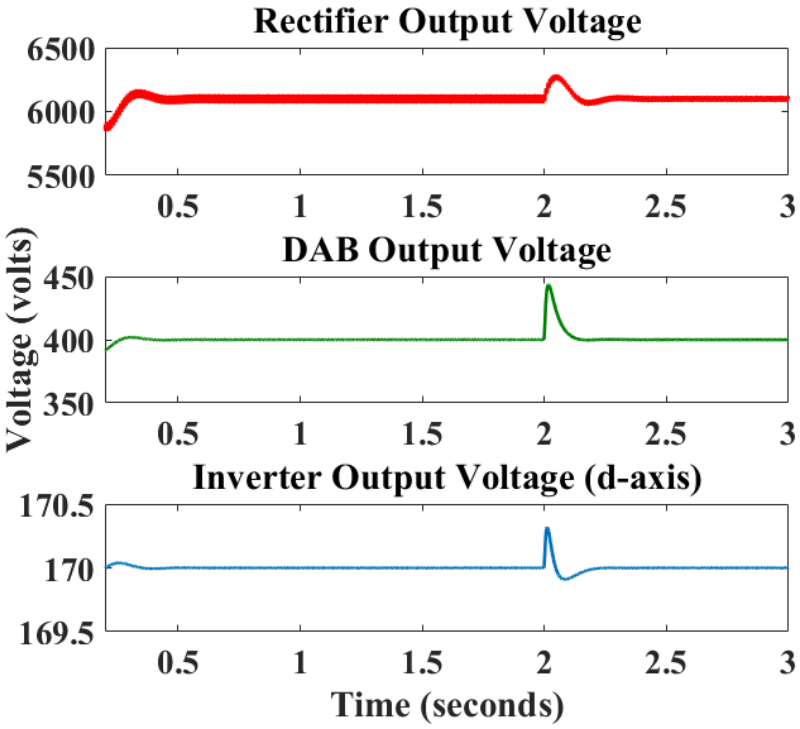

Figure 2.10: Case study with active power variation.

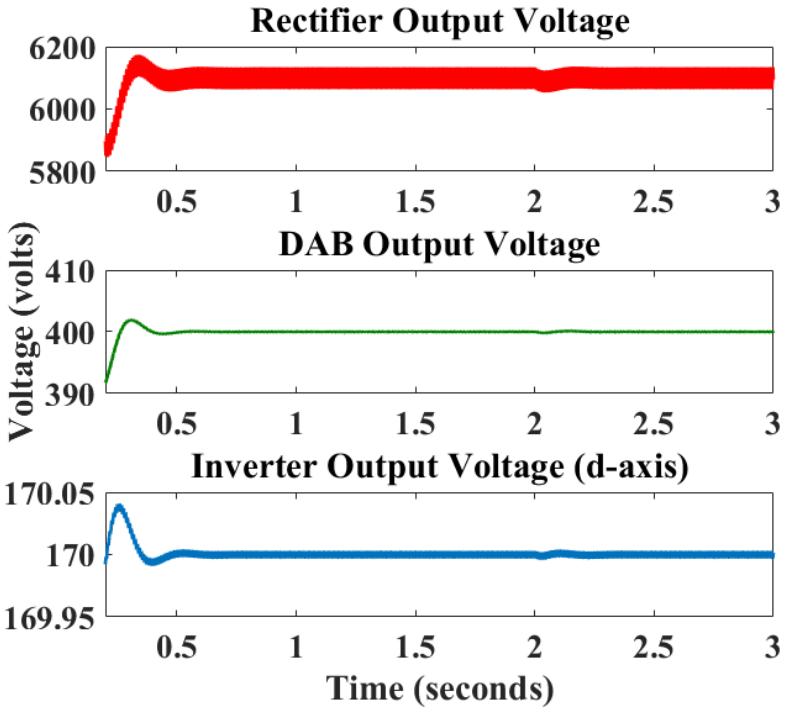

Figure 2.11: Case study with system parameter variation.

2.4. Feasibility and Stability Surface Plots Based on Rectifier Model

The 70th-order nonlinear differential-algebraic state-space model of a single-SST FREEDM power distribution system developed in the previous sections provides the opportunity to derive analytical relationships between physical parameters and feasible operational range. Nonlinear differential-algebraic state-space model of SST developed in the previous sections provides the opportunity to analyze the relationship as previous studies have shown a possible failure in the SST-based power distribution system in the SST farthest from the grid [28]. However, there is no indication of the reason for the failure; since the grid in the simulations has been assumed to be an infinite grid, the system breakdown can be either due to infeasibility or instability. Addressing this issue is one of the research motivation as that will eventually figure out the power bounds of such system, if there is any. Once the feasibility bounds are found for SST, the system parameters can be designed accordingly to provide the required power flow and energy exchange flexibility. Feasibility analysis of the FREEDM system is essential to answer the maximum net power capability that the system can handle. Once the feasibility bounds are known, the system parameters can be designed accordingly to provide the required power flow and energy exchange flexibility. The pair (y_1, I_{DAB}) has been identified to be critical for determining the equilibrium of the nonlinear FREEDM model where I_{DAB} represents the net current flowing through the DAB and y_1 is the *d*-axis grid voltage. Existence and uniqueness of equilibrium are then analyzed utilizing the rectifier state equations (2.1-2.10). Steady state values for the *d*-axis grid current is found (neglecting the sinusoidal terms in equation (2.3) at steady-state), and then, necessary conditions for I_{DAB} to maintain feasibility of SST is derived which is shown in equations (2.58-2.59). Rectifier input resistance a_2 can be designed to provide expanded feasible

operation region for any pair of (y_1, I_{DAB}). Fig. 2.12 shows that reducing a_2 results in expansion of feasible operating region of SST (green, red and white colors indicate the feasible stable, feasible unstable and infeasible region, respectively). It has also been found through analysis that proper choice of the rectifier output DC voltage reference can extend the feasibility bounds of the SST.

$$x_{1,ss} = \frac{-\frac{y_1}{a_2} \pm \sqrt{(\frac{y_1}{a_2})^2 - \frac{8I_{DAB,ss}r_2}{a_2}}}{2} \tag{2.58}$$

$$I_{DAB,ss} \leq \frac{y_1^2}{8a_2r_2} \tag{2.59}$$

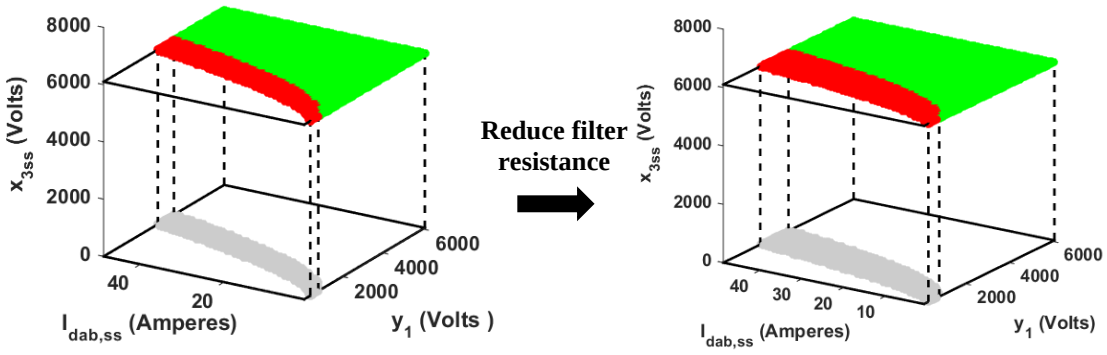

Figure 2.12. Expansion of feasibility region by reducing rectifier resistance.

Red zones represent the unstable regions inside the feasible operational range which can be reduced with the proper tuning of the controller gains. Fig. 2.13 shows the circular relationship between the system parameters and controller gains with the feasibility and stability region, respectively.

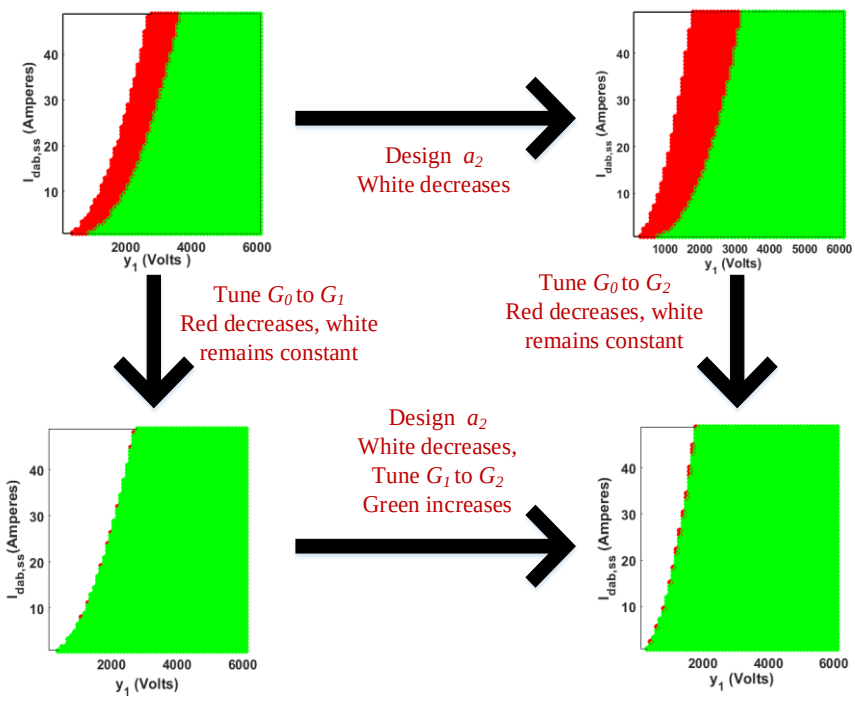

Figure 2.13. Feasibility and stability circle diagram.

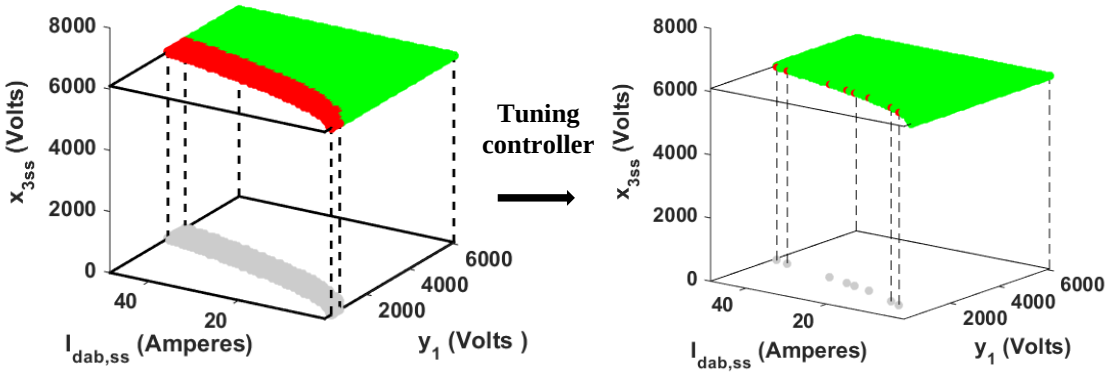

Figure 2.14. Expansion of stability region by retuning the controller gains.

Fig. 2.14 presents a case of the controller tuning to show the expansion of the feasible and stable region.

2.5. Contribution

1. Comprehensive average model of the FREEDM system that includes the SST and energy cells. PV, wind and storage make up the energy cells in the DC and AC buses.

2. Operational bounds for the SST based system to guarantee the feasible operation. The bounds are studied with a simplified SST model with rectifier states and surface plots clearly show the feasible and infeasible regions. Later, controller gains are also tuned to see the impact on the stability of the feasible operational points.

2.6. Conclusions

Dynamic modeling of a solid-state transformer based power distribution system (the FREEDM system) is analyzed for feasibility following the development of a 70^{th}-order state-space system representation. Detailed SST model along with renewable generation and storage systems and their corresponding interface circuits to DC and AC buses are considered in the modeling. The model is then utilized to define the feasible operational bounds for FREEDM system, which is useful for designing the power and energy management controllers. In chapter five, an IEEE 34 bus testbed is used to simulate the feasibility constraint based on the constraints developed in this chapter. The analysis is also critical to study the multiple-SST connected FREEDM system where power and energy sharing capability of the energy cells need to be considered as studied in chapter three. The comprehensive physics-based model and the developed system controllers can be used to evaluate the performance of the proposed distribution system under grid connected and islanded conditions.

CHAPTER 3

POWER SHARING METHODS IN A MULTIPLE SST BASED SYSTEM

3.1. Introduction

3.2. Single SST Feasibility Constraints and Expansion to Multi-SST Case

3.3. Proposed Power Sharing Methods to Maintain Feasibility

3.4. Case Studies with Different Conditions to Verify the Proposed Methods

3.5. Formulation of IPM/IEM Control Separation Based on the Study

3.6. Contribution

3.7. Conclusions

3.1. Introduction

In traditional electric power system, automatic generation control (AGC) adjusts the power output of multiple generators at different power plants to match the changes in the load. Since power grid requires instantaneous balancing of generation and load, continual adjustment of generator outputs is essential. Measurement of system frequency assists in balancing the system; as the frequency increases, load demand is less than the generation, and therefore, generators in the system decelerate. On the other hand, if the frequency decreases, less power is being generated than the instantaneous load demand, and therefore, machines in system accelerate [53]. Although, AGC based control works excellent for the traditional generation system, it does not work efficiently with MG based systems where generation capability exists at the distribution end from renewable resources. With advances in design of more efficient solar panels and wind farms, penetration of renewable resources into the power grid has increased. However, this increase leads to some technical challenges. One of the major drawbacks of this integration is the voltage rise due to the regenerative power flow from the renewable resources into the grid which results in facing instability issues in the system [54, 55]. To address the integration issues of RES, FREEDM system provides an excellent opportunity to integrate renewable resources with the help of power transformer that eliminates the usage of low frequency transformer [21]. SST being a frequency power transformer, has three stages that offers key technologies like flexible interfaces at Low Voltage household ports, supports as an energy transmitter, and enables distributed communication and control protocol. However, physical parameters of the SST pose operations bounds, coming from the non-linear nature of the power converters which is analyzed through the dynamic model in the second chapter. Knowledge about the operation

bounds are necessary to guarantee feasibility of the system by setting appropriate setpoints for every sub-system. Multiple power transformers can be connected in loop/tree configurations where neighboring transformers can support the change of load in any of those through adjusting their input power from grid. In order to find the operation bounds of a multi-SST power distribution system to define the power sharing capability, feasibility analysis for a single SST system is done briefly using its nonlinear dynamic model [56]. Knowledge of the feasible bounds will assist the controller to generate appropriate operating points for power balancing among the neighbors. The analysis is then extended to a multi-SST system to study the associated challenges with multiple SST implementation. Previous studies have found the dynamical model of the SST but there is no analysis on its feasible range [23, 25, and 27]. Moreover, there is no well-defined methods for power sharing between multiple SST systems in the power grid considering the physical constraints coming from the model, itself. In this analysis, based on the average model and feasibility analysis on the single SST, constraints for the multiple SST system in a MG has been developed and then, the analysis is utilized to develop the power sharing method among the SST neighbors. Two different methods have been proposed and simulated by maintaining the node voltage or input current constant after a step change in any SST in the neighborhood. Case studies are observed for this method which will lead to the formulation of IPM and IEM controller study to design a stable controller for multi-SST based system. Proposed power sharing methods are validated in a 9 SST model in a simulation test bed.

3.2. Single SST Feasibility Constraints and Expansion to Multi-SST Case

In this section, a feasibility analysis problem is formulated to find permissible total load that each part of the SST can handle (assuming infinite generation). Dynamic model and duty cycle constraint neglecting the second order grid harmonics for each SST subsystem can be written as equation (3.1) and (3.2), where $\alpha_1$and $\alpha_3$are the system parameters and references, respectively and $\alpha_2 \triangleq \{L_{dc}^* = L_{dc}(t \to \infty), L_{ac}^* = L_{ac}(t \to \infty)\}$ represents the steady-state value of net loads of DC and AC energy cells, respectively.

$$f(\bar{x}, \alpha_1, \alpha_2, \alpha_3) = 0 \tag{3.1}$$

$$g(\bar{x}, \alpha_1, \alpha_2, \alpha_3) \leq 0 \tag{3.2}$$

Dynamical model of a SST coupled to the models of the DC and AC energy cells in the low voltage distribution side is derived in previous chapter. The energy cells comprise of local loads, renewable generation (photovoltaic and/or wind power), and storage devices. Functional FREEDM system with SSTs connected in a tree topology is shown in Fig. 3.1; the circuit diagram of the SST model is provided in Fig. 3.2.

3.2.1. Feasibility Analysis of Rectifier

Front end rectifier is found to be the most critical stage of the SST and so the model of the rectifier is considered as representative of the SST for feasibility analysis. The steady state operating point of the rectifier system can be found by setting $\dot{x}_i = 0$ $(i = 1{:}3)$ and $\dot{\xi}_i = 0$ $(i = 1{:}3)$ in equations (2.1)-(2.6). Substituting d_1 and d_2 from (2.3) and (2.4) into (2.5) and defining the *d*-axis and *q*-axis input voltages of the rectifier as in equations (3.3) and

(3.4).

$$y_1 = v_{grid} + R_{line1}x_1 - X_{line1}x_2 \tag{3.3}$$

$$y_2 = R_{line1}x_2 + X_{line1}x_1 \tag{3.4}$$

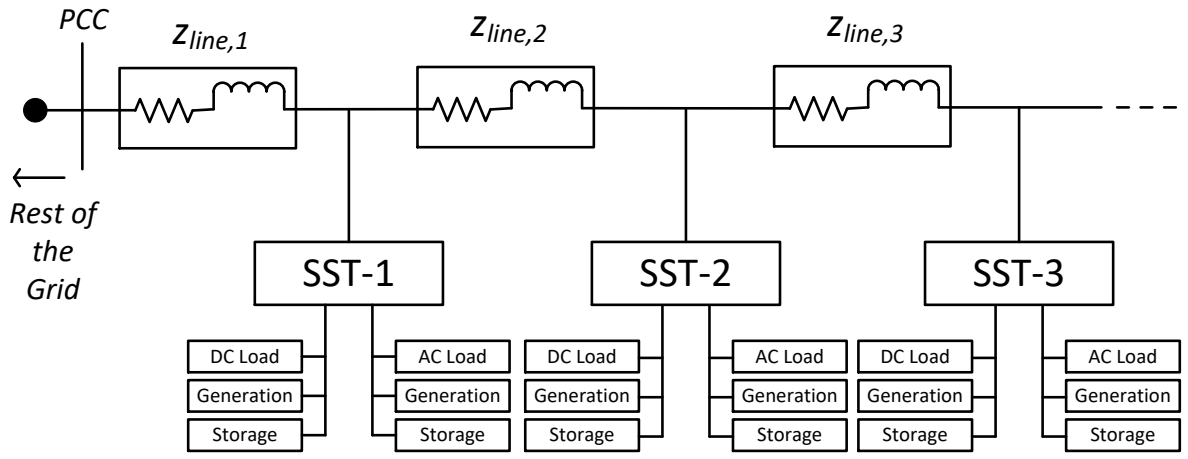

Figure 3.1: FREEDM system functional diagram.

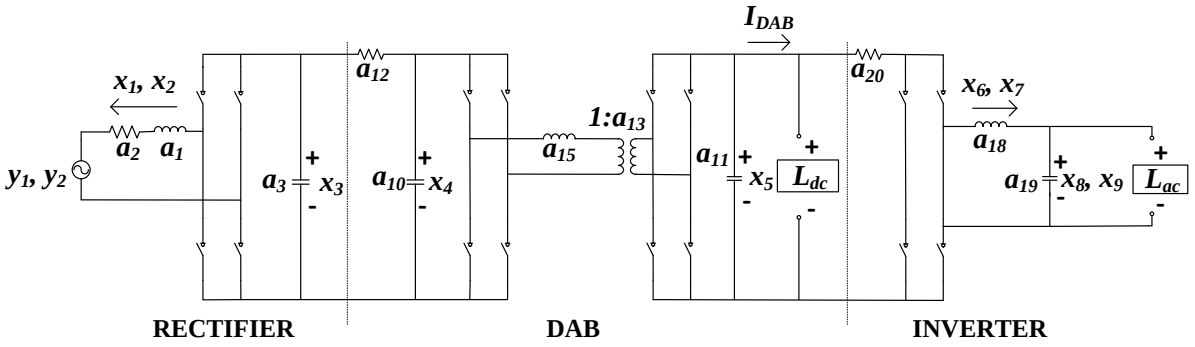

Figure 3.2: Circuit diagram of a solid-state transformer.

System states of the rectifier can be formulated as an equation of circle as shown in (3.5).

$$\left(x_1 + \frac{y_1}{2a_2}\right)^2 + \left(x_2 + \frac{y_2}{2a_2}\right)^2 = \frac{y_1^2 + y_2^2}{4a_2^2} - \frac{2P_{rec}}{a_2} \tag{3.5}$$

Based on the radius of the equation (3.5), the maximum power that can be processed through the rectifier stage of the SST is derived in (3.6).

$$P_{rec,max} = \frac{y_1^2 + y_2^2}{8a_2} \tag{3.6}$$

As the rectifier has power electronics switches and it requires to follow the duty cycle constrains and that can be formulated as an inequality equation as in (3.7).

$$\left(x_1 + \frac{a_2 y_1 + a_1 \omega_1 y_2}{a_2^2 + a_1^2 \omega_1^2}\right)^2 + \left(x_2 + \frac{a_2 y_2 - a_1 \omega_1 y_1}{a_2^2 + a_1^2 \omega_1^2}\right)^2 \leq \frac{r_1^2}{a_2^2 + a_1^2 \omega_1^2}. \tag{3.7}$$

Therefore, the feasibility range of the rectifier is defined as all of the points on the circle given in equation (3.5) that are on or inside the inequality equation given in (3.7). The constraints developed in equation (3.5) is dependent on the net power requirement of each SST and it can be extended to multi-SST case to analyze the feasibility in a microgrid. Feasibility analysis is first extended for multi-SST case considering the rectifier model only and then, the power sharing methods are developed based on that.

3.2.2. Multi-SST Circle Condition to Maintain Feasibility

When multiple SSTs are connected, a power flow algorithm is required to find the input current (and input node voltage) of each SST. However, the setpoints developed by this algorithm must maintain the feasibility of each SST system, i.e., the input voltage of each SST and its corresponding rectifier output DC voltage should satisfy the constraint given in equation (3.7). Steady-state value of the rectifier output voltage determines the radius of the inequality equation (3.7) and it can be adjusted to ensure the feasibility of the system for a particular load demand that will have to be processed by the rectifier stage of the SST. The similar equations can be used for a multi-SST simulation with a simplified model by assuming the full SST as rectifier, only. Fig. 3.3 shows the simplified structure of a multi-SST analysis in tree configuration.

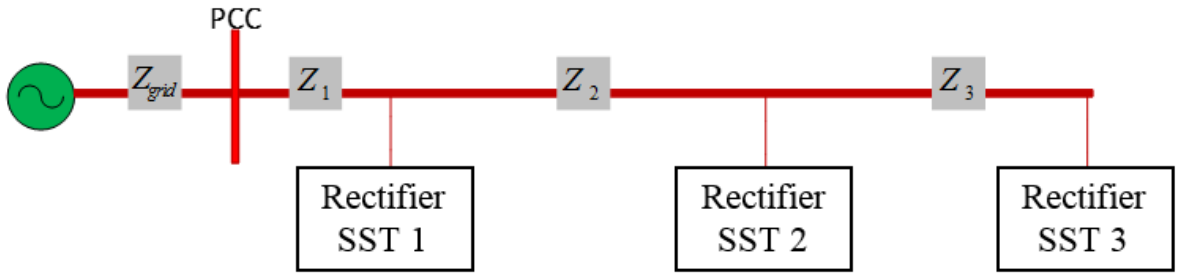

Figure 3.3. Simplified tree configuration with multi-SST.

The 3-SST configuration is used as benchmark for the analytical analysis and further simulation validation. Generally, in an *n*-SST distribution system, aside from the convergence of the power flow solution, there are *n* constraints that need to be satisfied. It should be noted that the solution of the power flow, i.e., the input voltages of each SST in the system is dependent on the net power of all of the SSTs in a network and that will impact the feasibility range. This is the coupling effect of SST loads on the input voltage of any neighboring SSTs. The feasibility constraints in this case will be similar as in equations (3.5) and (3.7) with the exception that the input voltages are not anymore free variable. Input voltage of any SST is expressed in equation (3.10). Feasibility equations for multi-SST cases are given in equations (3.8) and (3.9). The physical meanings of the states are the same as in section 3.2; the subscript i denotes the i^{th} SST, where $i = 1,2,3,\ldots\ldots,n$ and $Z_{line,i}$ refers to i^{th} SST the line impedance.

$$\left(x_{1i} + \frac{y_{1i}}{2a_{2i}}\right)^2 + \left(x_{2i} + \frac{y_{2i}}{2a_{2i}}\right)^2 = \frac{{y_{1i}}^2 + {y_{2i}}^2}{4{a_{2i}}^2} - \frac{2P_{rec,i}}{a_{2i}} \tag{3.8}$$

$$\left(x_{1i} + \frac{a_{2i}y_{1i} + a_{1i}\omega_{1i}y_{2i}}{a_{2i}^2 + a_{1i}^2\omega_{1i}^2}\right)^2 + \left(x_{2i} + \frac{a_{2i}y_{2i} - a_{1i}\omega_{1i}y_{1i}}{a_{2i}^2 + a_{1i}^2\omega_{1i}^2}\right)^2 \leq \frac{r_{1i}^2}{a_{2i}^2 + a_{1i}^2\omega_{1i}^2} \tag{3.9}$$

$$y_{1i} + j * y_{2i} = v_{grid}$$

$$+ Z_{line1} \sum_{k=1}^{n} (x_{1k} + jx_{2k}) + Z_{line2} \sum_{k=2}^{n} (x_{1k} + jx_{2k}) + \cdots$$

$$+ Z_{linei} \sum_{k=i}^{n} (x_{1k} + jx_{2k}) \quad (3.10)$$

3.3. Proposed Power Sharing Methods to Maintain Feasibility

In this section, power sharing methods are analyzed for properly updating the input current setpoints of each SST whenever there is a change in the load demand of one of the SSTs. Our goal is to find the maximum allowable change in the power that can flow through any i^{th}SST, due to such a change in the load so that the overall system can remain within a feasible zone of operation. A follow-up question is how should the input references of each SST change to handle this change in power flow? The envisioned architecture of the FREEDM distribution grid model consists of two layers of decision-making units - namely, IEM and IPM. The IEM layer is responsible for generating accurate load forecasts based on weather data, economic dispatch, and feedback information from various customers through their smart meter data, etc., over an interval of every 15 to 20 minutes. The IPM, on the other hand, is responsible for regulating the DC and AC link output voltages and input currents of each SST to comply with any change in the load. Loads can change through three distinct scenarios, as follows and is shown in Fig. 3.4:

Case 0: Unpredicted small changes in load

Grid operators generally have reliable knowledge about the upper and lower bounds for the net loads in the system. If the load of any SST changes at any time while remaining within

these bounds then the internal control methods such as droop control or small manipulations in the power generated by the batteries connected to this SST can maintain feasible operation of the system without any further need for updating the current setpoints.

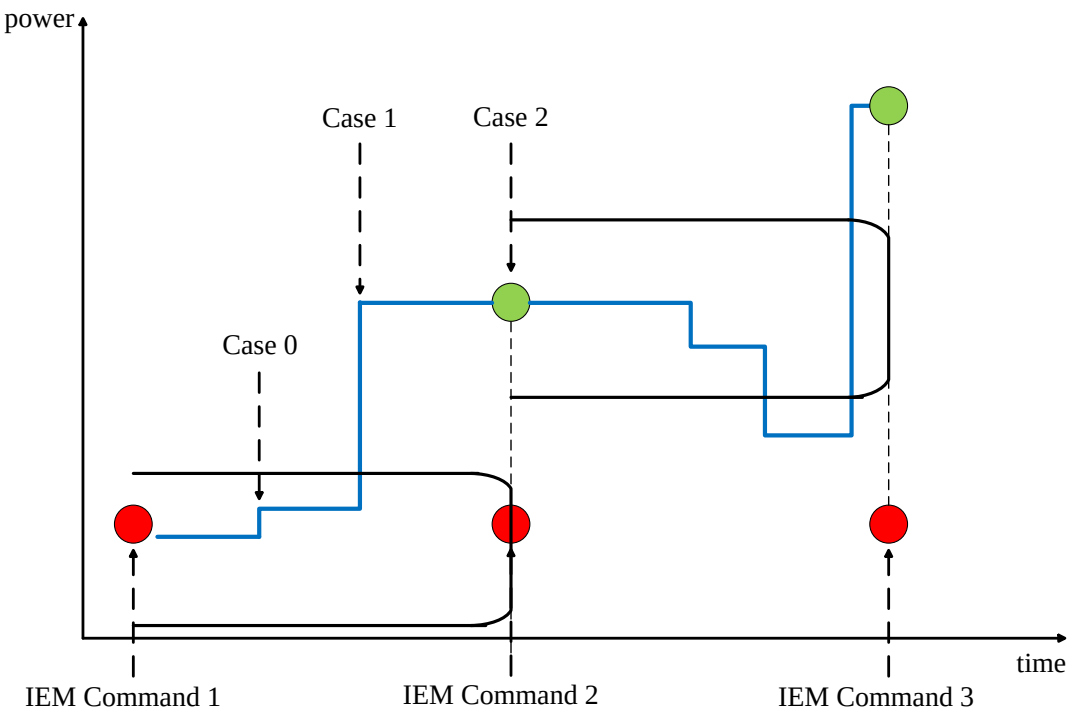

Figure 3.4. Different cases with change in power.

Case 1: Unpredicted large changes in load

If the load changes suddenly by a large amount in an unpredicted fashion then neither droop control will be able to compensate for this large change neither IPM will have enough time to recalculate the setpoints by solving a large power flow problem. In this situation, the IPM must override the IEM commands instantaneously to maintain the feasibility of the system. We next state two power sharing methods between SSTs by which this can be made possible.

Case 2: Predicted large changes in load

Typically, the IEM unit can predict changes in the loads fairly accurately 15 to 20 minutes in advance. Thus, if a large change in load is anticipated then the IEM must run a constrained

power flow algorithm for the entire grid model over this 15 minute interval, and compute new setpoints for the voltages and currents of every SST.

3.3.1. Method 1: Power Sharing with Constant Input Current

In order to avoid the complexity of running power flow algorithms as in Case 1 when there is a change in power of a SST, other SSTs can help the SST in need by reducing their net power while keeping their input current setpoint the same as before. Net power of the neighboring SSTs has to satisfy the maximum power constraints with their updated input voltages. Firstly the circle expression for the multiple SSTs according to equation 3.8 to 3.10 are considered to maintain the feasibility in developing these power sharing methods. The node voltage of the SSTs are expressed in equation (3.11) for a radial network of FREEDM system as shown in Fig. 3. 5.

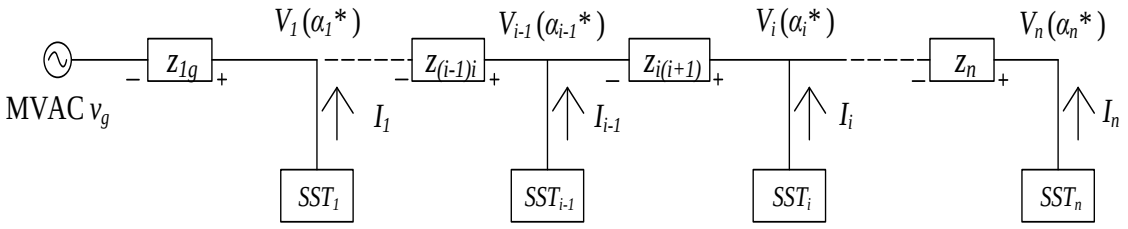

Figure 3.5. Radial network of FREEDM system.

$$V_1 = V_g - Z_1(I_1 + I_2 + .. + I_i + .. + I_n)$$

$$V_2 = V_1 - Z_2(I_2 + .. + I_i + .. + I_n)$$

……..

……..

$$V_{i-1} = V_{i-2} - Z_{i-1}(I_{i-1} + I_i + .. + I_n)$$

$$V_i = V_{i-1} - Z_i(I_i + I_{i+1} + .. + I_n)$$

……..

$$V_n = V_{n-1} - Z_n I_n \tag{3.11}$$

With a change in power in the i^{th} SST, the current of that SST will change and other will also change due to the subsequent change in the voltage if the net power remains the same in all the other SSTs in the network as shown in equation (3.12).

$$V_1' = V_g' - Z_1(I_1' + I_2' + .. + I_i' + .. + I_n')$$

$$V_2' = V_1' - Z_2(I_2' + .. + I_i' + .. + I_n')$$

……..

……..

$$V_{i-1}' = V_{i-2}' - Z_{i-1}(I_{i-1}' + I_i' + .. + I_n')$$

$$V_i' = V_{i-1}' - Z_i(I_i' + I_{i+1}' + .. + I_n')$$

……..

……..

$$V_{n-1}' = V_{n-2}' - Z_n(I_{n-1}' + I_n')$$

$$V_n' = V_{n-1}' - Z_n I_n' \tag{3.12}$$

However, the system will never reach to solution without a power flow solver if all the node voltage and currents are getting changed and the system will become oscillatory. Power flow solver has a significant computation delay which is impractical to run during the IPM operation. To avoid the complexity of running the power during the IEM commands, in method one the node current of the other SSTs except the i^{th} SST remain unchanged as shown in equation (3.13).

$$V_1' = V_g' - Z_1(I_1 + I_2 + .. + I_i' + .. + I_n)$$

$$V_2' = V_1' - Z_2(I_2 + .. + I_i' + .. + I_n)$$

……..

……..

$$V'_{i-1} = V'_{i-2} - Z_{i-1}(I_{i-1} + I'_i + .. + I_n)$$

$$V'_i = V'_{i-1} - Z_i(I'_i + I_{i+1} + .. + I_n)$$

$$V'_{i+1} = V'_i - Z_{i+1}(I_{i+1} + I_{i+2} + .. + I_n)$$

……..

……..

$$V'_{n-1} = V'_{n-2} - Z_n(I_{n-1} + I_n)$$

$$V'_n = V'_{n-1} - Z_n I_n \tag{3.13}$$

It can be shown from equations (3.11) to (3.13), to maintain the current of each nodes same as before; the voltage difference of each node will be a function of the change in current of i^{th} SST and is shown in equations (3.14) – (3.15).

$$\Delta V_m = \Delta V_i; \qquad for\ m \in \{1, \ldots\ldots, n\} \neq i \tag{3.14}$$

$$\Delta y_{1m} + j\Delta y_{2m} = \Delta y_{1i} + j\Delta y_{2i} = \ (\Delta x_{1i} + j\Delta x_{2i}) \sum_{p=1}^{m} r_k + j\ x_k \tag{3.15}$$

Assuming that the *q*-axis input current of SST_i remains unchanged ($x'_{2i} = x_{2i}$), the change in x_{1i} can be found by reducing the feasibility equations given by (3.8) for the two conditions before and after the change. This would result in a second order polynomial shown in (3.16) relating the change in *d*-axis current of SST_i (Δx_{1i}) to the change in the net power ($\Delta P_{rec,i}$), system parameters, and current operating point of the system.

$$\left(a_{2i} + \sum_{k=1}^{i} R_{line,k}\right)\Delta {x_{1i}}^2 + \left\{2a_{2i}x_{1i} + y_{1i} + \sum_{k=1}^{i} R_{line,k}\, x_{1i} + \sum_{k=1}^{i} X_{line,k}\, x_{2i}\right\}\Delta x_{1i}$$

$$+ 2\Delta P_{rec,i} = 0 \tag{3.16}$$

The maximum allowable change in the power ($\Delta P_{rec,i_{max}}$) can be found based on the discriminant of this equation.

$$\Delta P_{rec,i_{max}} = \frac{\left\{2a_{2i}x_{1i} + y_{1i} + \sum_{k=1}^{i} R_{line,k}\, x_{1i} + \sum_{k=1}^{i} X_{line,k}\, x_{2i}\right\}^2}{8\left(a_{2i} + \sum_{k=1}^{i} R_{line,k}\right)} \tag{3.17}$$

Since the goal is to keep the other current setpoints unchanged, this Δx_{1i} will be the only change in the current of SSTs which would cause a change in the voltages of all of the SSTs (based on KCL and KVL). These new SST input voltages should be such that the net power of each SST is less than its maximum capability shown in (3.6). Additionally, rectifier output DC voltage for each SST should be updated as shown in equation (3.11) to guarantee feasibility for each individual SST.

3.3.2. Method 2: Power Sharing with Constant Node Voltage

An alternative method of maintaining feasible operation is to keep constant node voltage of all other SSTs by changing the steady-state values of their input currents. That is, if the power flow of the i^{th} SST changes in steady-state then the input voltage of k^{th} SST where $k \neq i$ will be kept constant. After a few circuit calculations, the change in the voltage phasor for any m^{th} SST, $(m = 1{:}\,n)$ can be derived as in equation (3.18).

$$\Delta y_{1m} + j\Delta y_{2m} = \sum_{p=1}^{m} Z_{line,p} \sum_{l=p}^{n} \Delta x_{1l} + j\Delta x_{2l} \quad (m = 1{:}\,n) \tag{3.18}$$

Note that the implicit assumption here is that the SSTs are connected over a line topology as shown in Fig. 3.7. With a change in power of i^{th} SST, the goal is to keep the input voltage of other SSTs constant, i.e., $\Delta y_{1k} + j\Delta y_{2k} = 0$ $(k = 1{:}\,n, k \neq i)$ which will result in equation (3.19).

$$\Delta x_{1m} + j\Delta x_{2m} = 0 \quad (m \geq i + 2 \;\&\; m \leq i - 2) \tag{3.19}$$

$$\Delta x_{1(i+1)} + j\Delta x_{2(i+1)} = -\frac{Z_{line,i}}{Z_{line,i} + Z_{line,i+1}}(\Delta x_{1i} + j\Delta x_{2i}) \quad (3.20)$$

$$\Delta x_{1(i-1)} + j\Delta x_{2(i-1)} = -(\Delta x_{1i} + j\Delta x_{2i}) - \left(\Delta x_{1(i+1)} + j\Delta x_{2(i+1)}\right) \quad (3.21)$$

In this case, with a change in the power of i^{th} SST, the input current setpoints of $(i-1)^{th}$ SST, i^{th} SST and $(i+1)^{th}$ SST change and the other setpoints remain the same. Using equations (3.8), assuming that the *q*-axis input current of i^{th} SST remains unchanged as in method 1, the following equation (3.22) can be derived.

$$\begin{aligned}(a_{2i} + \{R_i(1-\alpha) + \beta X_i\})\Delta x_{1i}{}^2 \\ + (\{2a_{2i} + R_i(1-\alpha) + \beta X_i\}x_{1i} + y_{1i} + \{X_i(1-\alpha) - \beta R_i\}x_{2i})\Delta x_{1i} \\ + 2\Delta P_{rec,i} = 0 \end{aligned} \quad (3.22)$$

where $\alpha = Re\left\{\frac{Z_{line,i}}{Z_{line,i}+Z_{line,i+1}}\right\}$ and $\beta = Im\left\{\frac{Z_{line,i}}{Z_{line,i}+Z_{line,i+1}}\right\}$.

The discriminant of (3.22) gives the maximum allowable change in the power $\Delta P_{rec,i_{max}}$ of SST_i such that the system can maintain its feasibility.

$$\Delta P_{rec,i_{max}} = \frac{\left((2a_{2i}x_{1i} + \{R_i(1-\alpha) + \beta X_i\}x_{1i} + y_{1i} + \{X_i(1-\alpha) - \beta R_i\}x_{2i})\right)^2}{8(a_{2i} + \{R_i(1-\alpha) + \beta X_i\})} \quad (3.23)$$

It should be noted that if the change is in the power of the n^{th} SST in the system, then $\alpha = \beta = 1$.

3.4. Case Studies with Different Conditions to Verify the Proposed Methods

Simulation results applying the two proposed power sharing methods to a nine SST system is presented. The parameters of the SSTs are based on Gen 2 SST [57]. The load data of each SST and the line data are provided in Table 3.1.

Figures 3.6, 3.7 and 3.8 show the simulation results of applying method one to the nine SST system. Fig. 3.6 shows the net power flowing through each SST when a step changes is performed in SST_1. As discussed in section 3.3.1, the neighbors will share the power change in any SST to make the system operated within the feasible bounds and also, power flow is not required to perform. As the power level changes, it will impact the voltage and current of the SST_2 - SST_9. In method 1, the expectation is to keep the input current constant by updating the node voltage of the SST. Fig. 3.7 shows the change in node voltage of SST_2 and SST_7 to adjust the change in power, however, the input current of SST_2 and SST_7 are same as before which is shown in Fig. 3.8.

Table 3.1 Simulation data of the nine SST system validation.

	Net Power (kW)	Line Impedance (Ohms)
SST_1	1 (0-1s) 10 (1-2s) 6 (2-3s)	$Z_{lineo1} = 0.653 + i\ 0.651$
SST_2	10	$Z_{line12} = 0.438 + i\ 0.437$
SST_3	1	$Z_{line23} = 8.16 + i\ 8.14$
SST_4	1	$Z_{line34} = 9.49 + i\ 9.74$
SST_5	1	$Z_{line45} = 7.53 + i\ 7.51$
SST_6	1	$Z_{line56} = 0.0037 + i\ 0.0027$
SST_7	1	$Z_{line67} = 0.906 + i\ 0.481$
SST_8	1	$Z_{line78} = 25.52 + i\ 13.546$
SST_9	1	$Z_{line89} = 7.284 + i\ 13.865$

Next chapter will deal with the system sizing of the storage such that, neighboring SSTs can support the change in power of any SST in the system following the method simulated. Voltage and current profiles form the Figures 3.7 and 3.8 validate the proposed method 1 of sharing the power with neighboring SSTs in the network by keeping the input current constant in all the SSTs other than the one that has change in power. Figures 3.9, 3.10 and 3.11 show the simulation results by applying method two to the same nine SST system for validation purposes. Fig. 3.9 shows the net power flowing through each SST when a step changes is performed in SST_1. As discussed in section 3.3.2, only the immediate neighbors will share the power change in any SST to make the system operated within the feasible bounds in method 2. Thus the power level will only change for SST_2, there will no impact on SST_7 as that is not an immediate neighbor of SST_1. Fig. 3.11 eventually shows that the power set point for the SST_7 remains the same where it changes for SST_2. In method 2, the expectation is to keep the node voltage current by updating the input current of the SST. Fig. 3.10 shows the node voltage does not change in the steady-state for SST_2 and SST_7 though there is change in power in SST_1. However, the input current of SST_2 is changed but there is no change in SST_7 that verifies the approach applying by method 2. Next chapter will deal with the system sizing of the storage such that, immediate neighboring SSTs can support the change in power of any SST in the system following the method simulated. Power, voltage and current profiles form the Figures 3.9, 3.10 and 3.11 validate the proposed method 2 of sharing the power with immediate neighboring SSTs in the network by keeping the node voltage constant in all the SSTs other than the one that has change in power.

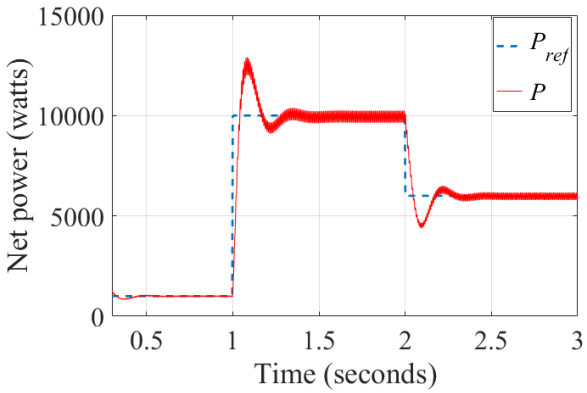

(a) Power profile of SST-1

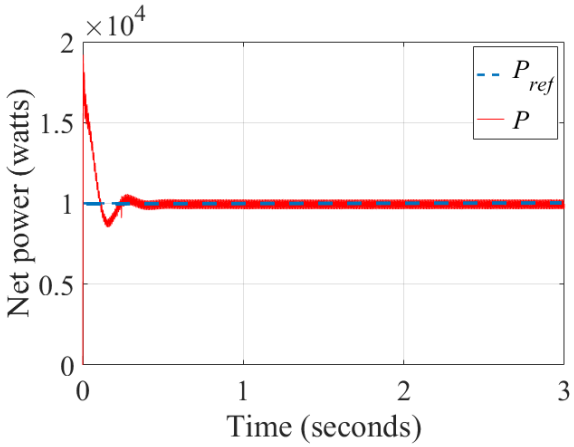

(b) Power profile of SST-1

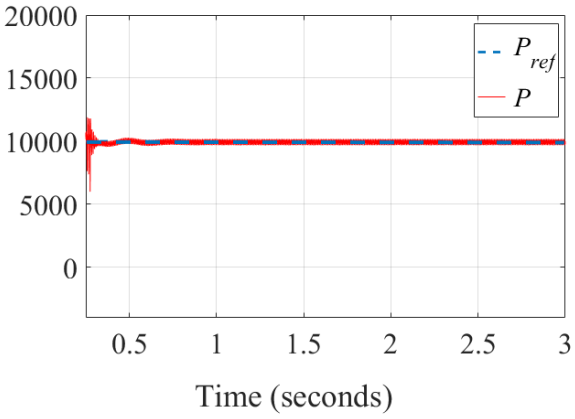

(c) Power profile of SST-7

Figure 3.6. Net power of each SST by applying method one.

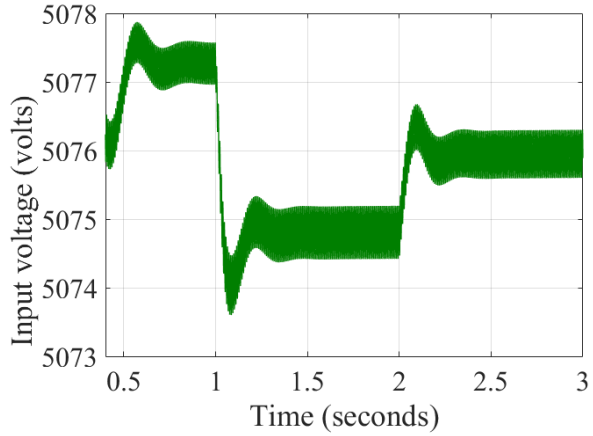

(a) Voltage profile of SST-1

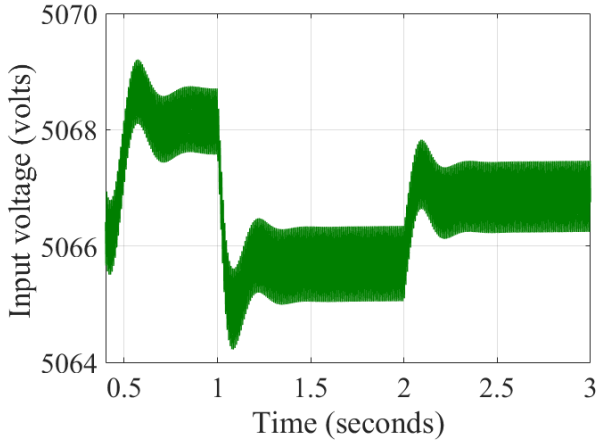

(b) Voltage profile of SST-2

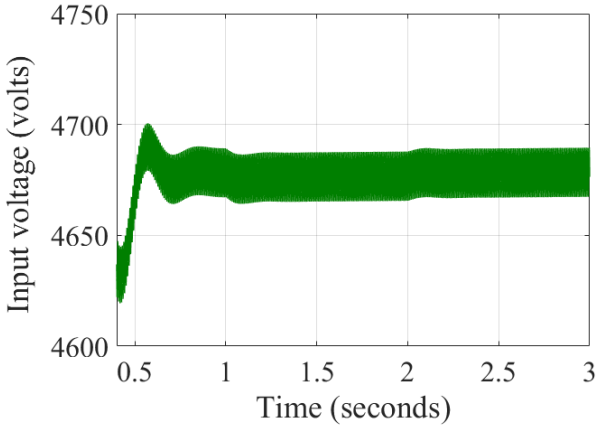

(c) Voltage profile of SST-7

Figure 3.7. Input voltage of each SST by applying method one.

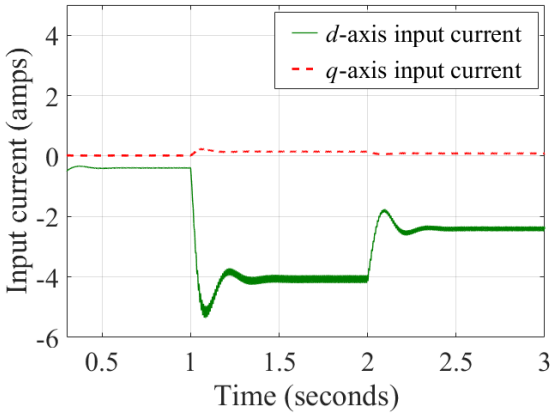

(a) Current profile of SST-1

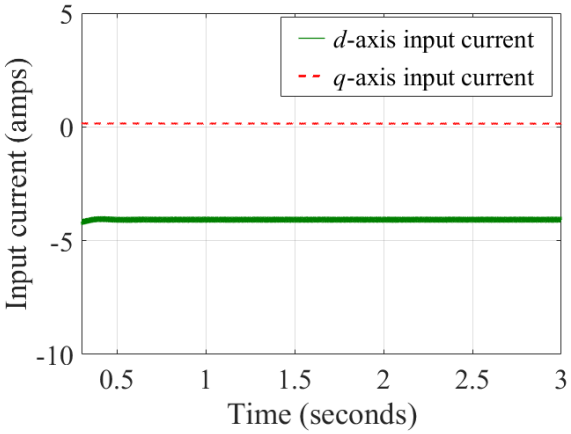

(b) Current profile of SST-2

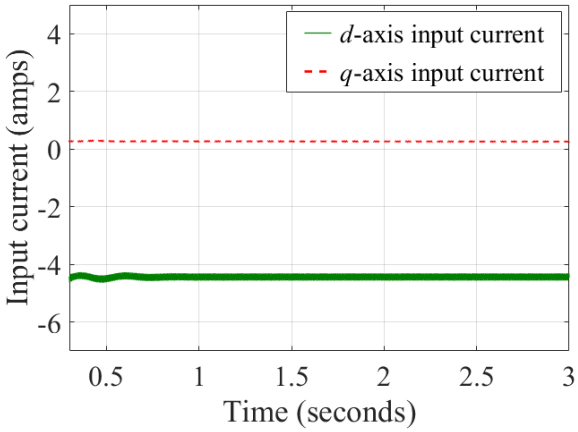

(c) Current profile of SST-7

Figure 3.8. Input current of each SST by applying method one.

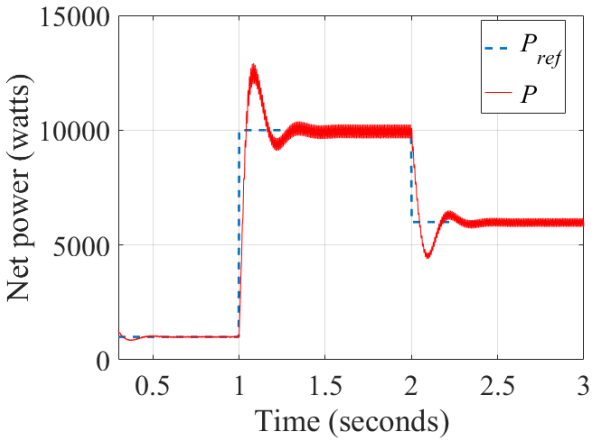

(a) Power profile of SST-1

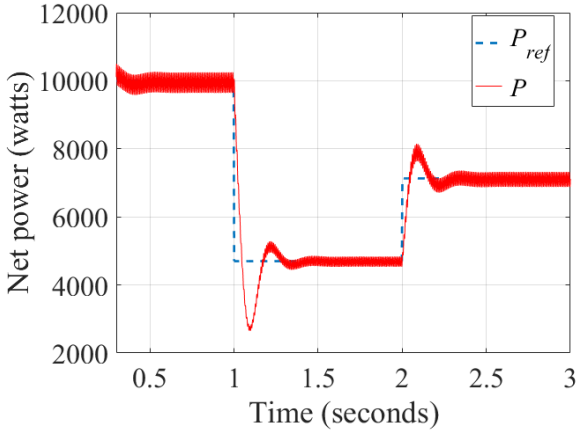

(a) Power profile of SST-2

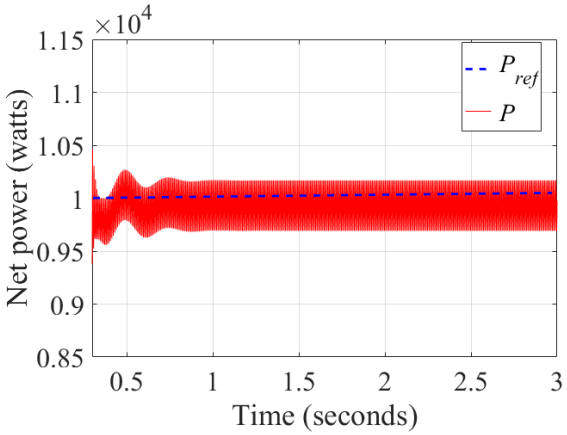

(a) Power profile of SST-7

Figure 3.9. Net power of each SST by applying method two.

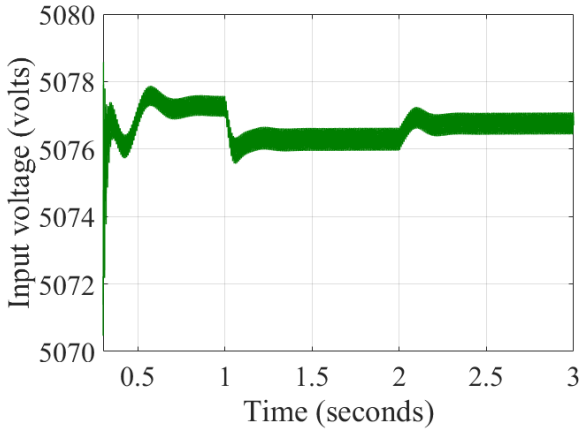

(a) Voltage profile of SST-1

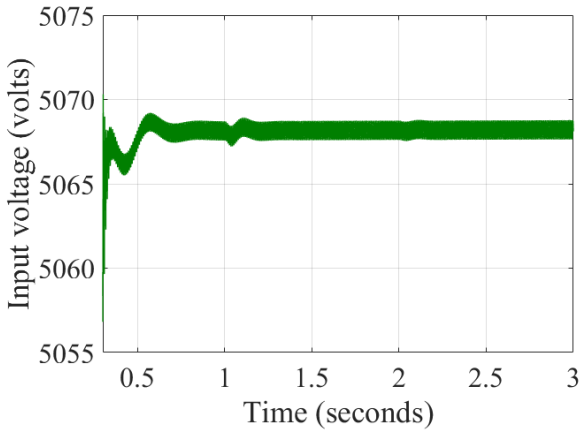

(b) Voltage profile of SST-2

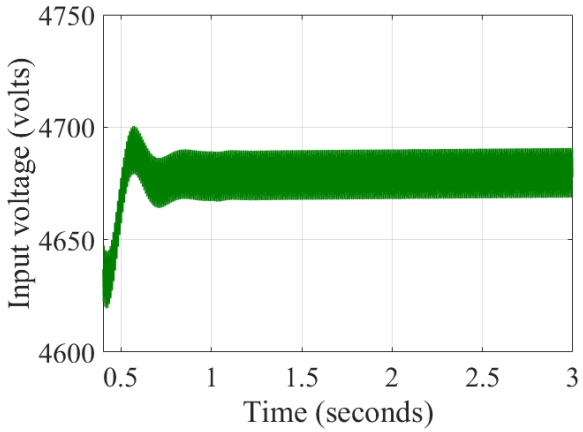

(c) Voltage profile of SST-7

Figure 3.10. Input voltage of each SST by applying method two.

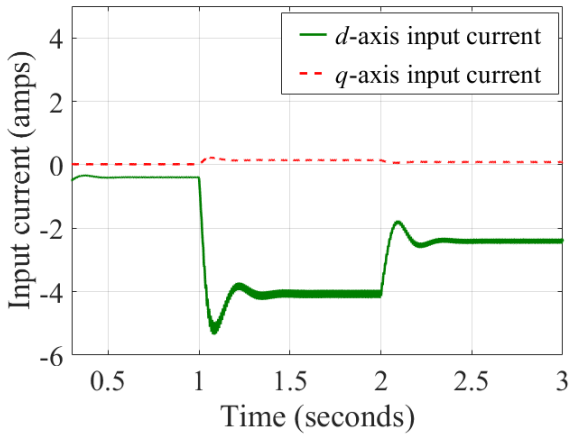

(a) Current profile of SST-1

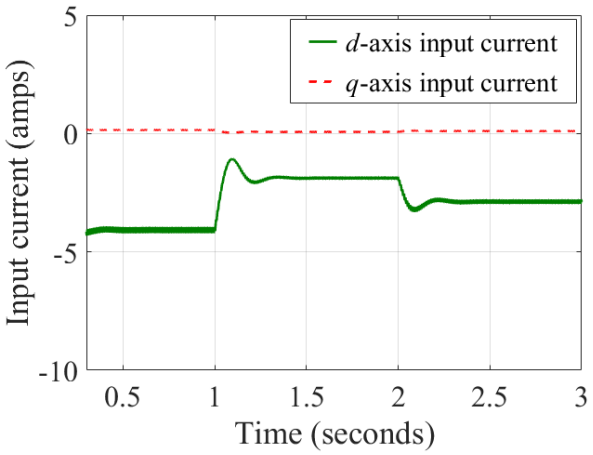

(b) Current profile of SST-2

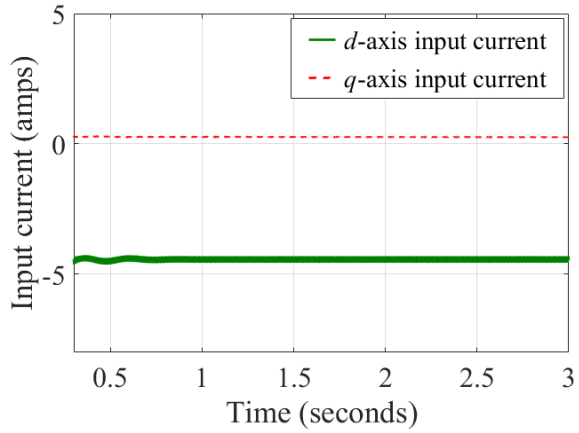

(c) Current profile of SST-7

Figure 3.11. Input current of each SST by applying method two.

3.5. Formulation of IPM/IEM Control Separation Based on the Study

Power sharing methods developed in this chapter along with the system level constraints will lay out the formulation of the two controller layer designing process associated with the FREEDM system. These layers are IEM and IPM controller with designated purposes of maintaining the high level energy balance and power balance in the system, respectively. IPM unit is responsible for regulating DC and AC MG output voltages and input current of each SST system instantaneously to balance any change of power in the system. IPM controller regulates the bus voltages to either a fixed value or to a value within an allowable range using a droop controller. This controller should be robust to power variations in the energy cells connected to both DC and AC MGs. On the other hand, IEM unit is responsible for providing setpoints for the DRER and DESD in the system in every 15-20 minutes to maintain the optimum energy balance. These setpoints are chosen based on weather forecast data, economic constraints, load demand and real-time feedback from MGs in the system. A systematic diagram of a three SST system with a centralized IEM and IPM is shown in Fig. 3.12. As it can be seen in the figure, the power levels of the MGs along with the state of charge (SOC) of the DESDs and input current of SSTs are required to feed back to the IPM controller using a communication line. The input current and DC and AC bus voltages are used in the controllers in the IPM to regulate them to their reference values while energy cells data is fed back to the IEM to provide new setpoints for the system. However, the net power of energy cells at any instant of time may not match the predicted power from IEM and then IPM will have to overwrite the command to match that.

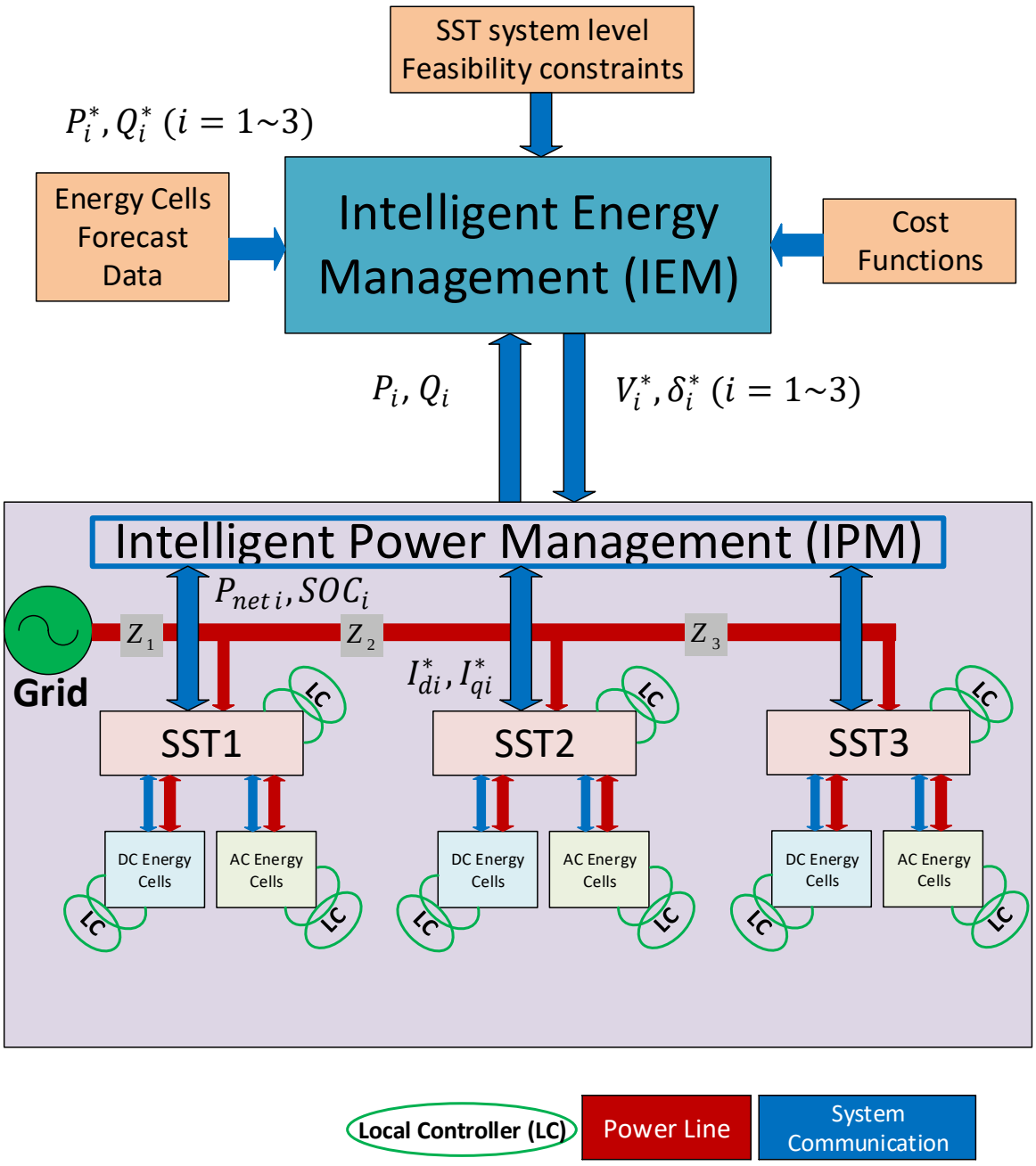

Figure 3.12. Control architecture of FREEDM system.

When extra amount of power is required in either DC or AC MGs (due to extra amount of load or reduced DRER generation), current flow through the DAB increases that is captured by a sag in the DC bus voltage. Similarly, voltage rise is visible in the bus voltage when the power requirement gets decreased. Using a resilient controller to changes in power results in

the voltage settling back to its reference value. However, the current that is flowing from DC bus gets changed due to the change in power and the input current reference of the SST (flowing from the grid) also needs to get adjusted according to that. IPM controller has to match those excess or less power requirements by updating the setpoints of the system instantaneously, therefore, IPM needs to override the IEM command whenever no internal control (such as droop control) can make the system work using its previous setpoints. This process has been illustrated in Fig. 3.13.

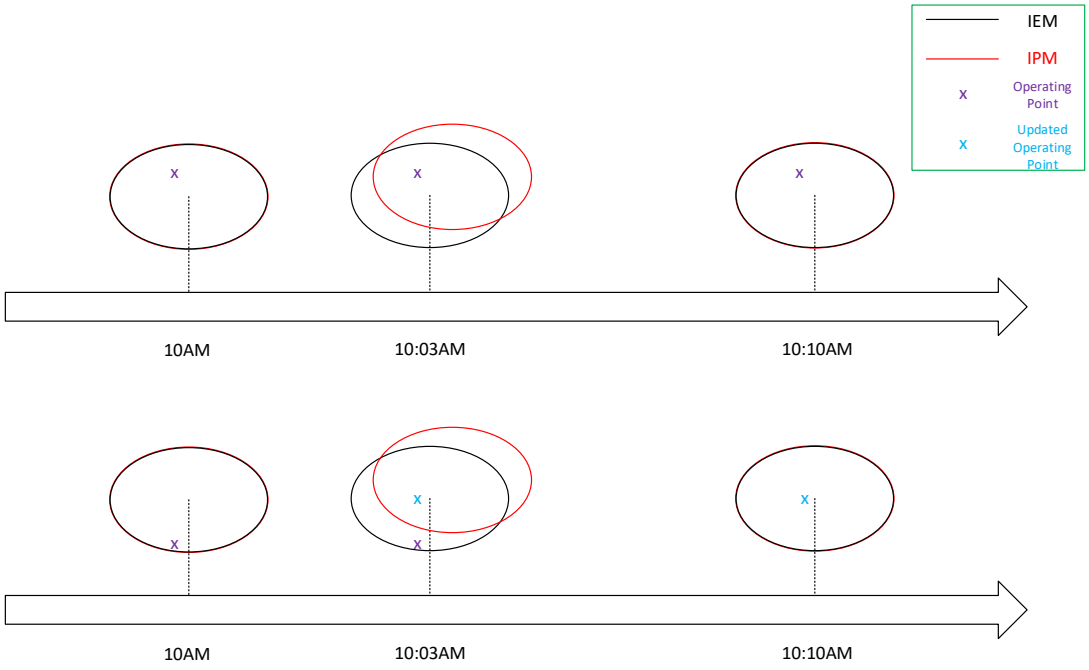

Figure 3.13. Control interaction between IEM and IPM.

This particular section illustrates the problem formulation for the IEM and IPM controller so that those controller design take in consideration the system level feasible constraints. Controller can be designed in different ways by decentralized or distributed and that will be a part of the future study based on the findings of this particular chapter. Fig. 3.14 presents the control structure considering the power sharing through a cloud interface in between IPM and IEM layers.

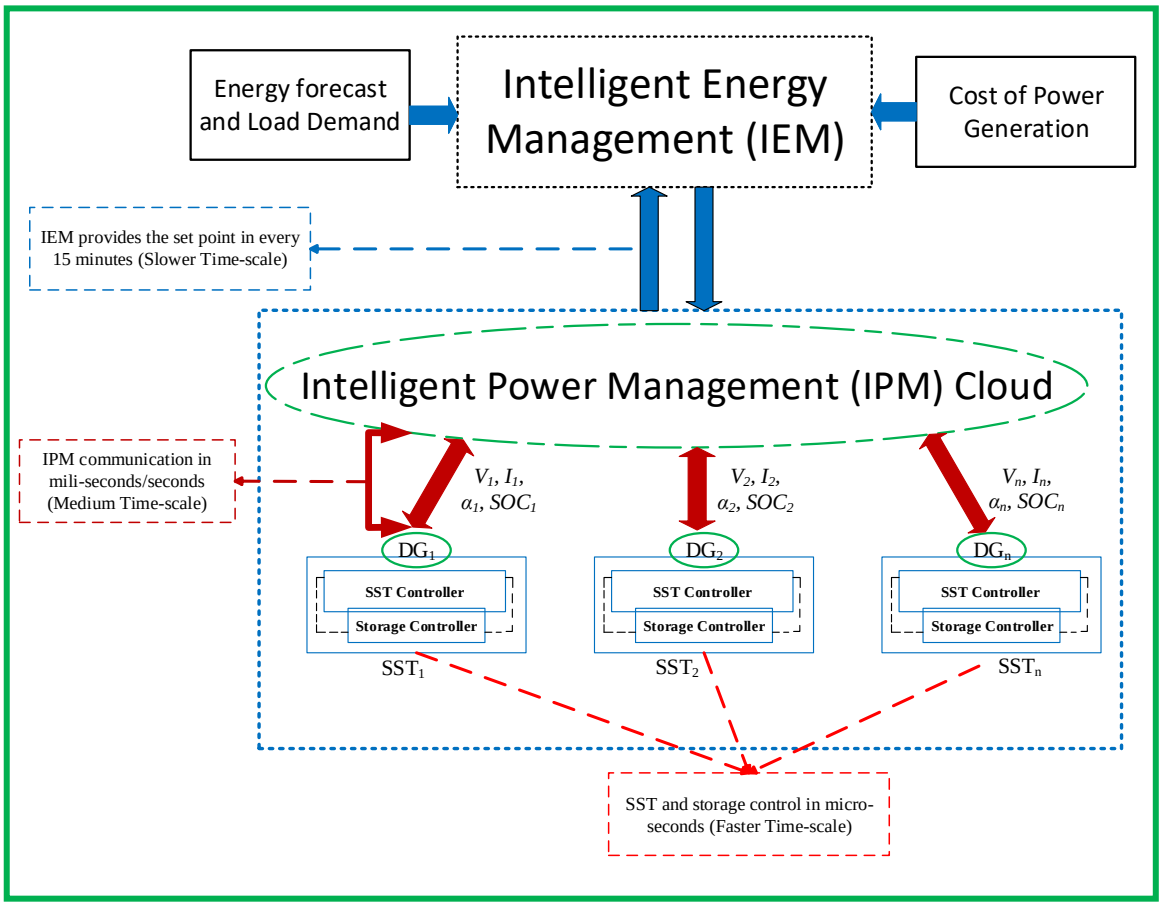

Figure 3.14. Timescale separation of the controller in FREEM system.

The cloud communication can be much slower compared to the micro-second timescale of the IPM controllers for grid side and microgrid control. However, it is important to reduce the communication delay as much as possible to get rid of the transient oscillations when the system will operate under wrong operations set point. Storage controllers are developed in the next section to implement for the power sharing methods considering the control structure in Fig. 3.14.

3.6. Contribution

1. Extend the individual constraints for the rectifier stage of single SST to multi-SST case in tree configuration and demonstrate the interaction of the feasibility constraints to maintain feasibility in a microgrid.

2. Develop the power sharing methods to support any instantaneous change in any SST in the network. These methods will play important role for the implementation of the SST in the distribution grid with added value. Validation results are also achieved for such methods in a three SST network.

3. Formulation of the intelligent energy and power level controller for FREEDM system which lays down the architecture for the storage controller development presented in the next chapter.

3.7. Conclusions

With advances in the RES, more of these resources penetrate the traditional power grid. However, this penetration causes some performance and stability problems such as voltage rise, no control on reactive power, and other grid interconnection issues. Setpoint controlled energy routers such as the SST based FREEDM system can replace the traditional transformers in the distribution grid to solve these problems with their flexibility on power control through sharing the resources among neighbors. In order to utilize these setpoint based systems, feasibility bounds are essential to be known that will guarantee the true commands are generated for power sharing algorithm. This chapter takes SST as an example of the setpoint based energy routers to derive its physical model, and then, utilize the model to identify the bounds those have been imposed by the non-linearity of this power

transformer and its duty cycle constraints. SST's front-end rectifier output voltage reference is found to be the deciding factor in extending the feasibility bounds of the system. As multiple SST systems are connected in a tree configuration, power sharing methods are proposed to maintain the feasibility of the system when there is a change in the load of any of the SSTs. Finally, two main layers of FREEM system control network have been introduced (IEM and IPM) and their interaction based on different levels of load change in the system are formulated to implement the power sharing methods, both in predicted and unpredicted power change cases.

CHAPTER 4

MICROGRID STORAGE CONTROL IN FREEDM SYSTEM

4.1. Introduction

4.2. Energy Storage in FREEDM System

4.3. Input-output Controller for the Energy Storage

4.4. Storage Controller for Power Sharing Methods

4.5. Validation of the Storage Controller

4.6. Contribution

4.7. Conclusions

4.1. Introduction

Distributed RES and storage are the critical part of FREEDM system as the developed power sharing methods in previous chapter are heavily dependent on the dynamic operation of these. RES generation can be predicted from the weather pattern that will be beneficial for the IEM level controller, however, the unpredictability of the load demand can only be supported by the proper storage control in the microgrid (MG) side for a stable operation of the distribution grid. Traditionally, storages are controlled considering different operational benefits, though fewer initiatives are taken to design storage controller based on system feasible operational bounds and power sharing in MG. Storage control in MGs are approached from a probabilistic view to support the variation of renewables [36]. Storage and wind generators are controlled together to optimize the sizing of the storage, though this kind of approach does not consider the operational constraints arise from the power electronics converter in the system. Several researches study the impact of sizing and control of the energy storage along with RES for an efficient operation in MGs without considering any power sharing capability [58, 59, and 60]. Storage is also studied to support the voltage fluctuation in the grid system with higher penetration of PV energy [61, 62, and 63]. Storage system is designed to support the reactive power with residential PV system that improves the power quality of the grid system [61]. Power fluctuation impacts the stability of the distribution network which can also be mitigated by the use of storage system [62, 64]. Optimized algorithms are proposed to size and control the storage system to reduce the system cost, though it does not guarantee the operational feasibility of MGs [65, 66, 67, and 68]. Besides, multi-objective optimization and dynamic programming are used to design the storage controller that helps to support different tariff plans for achieving maximum benefits

[69, 70, 71, and 72]. The missing part of the literature is the development of the energy storage control with respect to feasibility bounds of interfaced converter, like SST in our case. The necessity of using storage becomes evident in situations when maintaining the desired voltage and current setpoints at the points of common coupling in MG networks is extremely important for the sake of steady-state electrical performance and locational marginal pricing. These setpoints are usually direct functions of the load demands and renewable generation, meaning that as those change periodically then the voltage and current setpoints require to be updated accordingly. In FREEDM system, IEM forecasts load demand and generation, solves power flow, and sends out new setpoints at an interval of every 15-20 minutes so that the primary controllers of each MG can update their setpoint settings to guarantee stable operation at the new operating point. The trouble, however, arises when a sudden large change in load/generation occurs in a completely unpredicted way at any time between the ticks of this 15 minute interval. If the deviation is small then droop controllers may still be able to maintain stability, but for large deviations neither will droop work, nor will the IEM have enough time to solve for the new controller setpoints. The role of the storage unit in such scenario is then to handle the difference in net power in the microgrid. Nevertheless, using just one single battery can be quite uneconomical.

This chapter takes into the consideration of appropriate controller design for energy storage system in the DC energy cell to support the dynamic variation in SST based MG and then to enable the proposed power sharing methods in a distribution network with multiple SSTs. Efficient control of the storage system considering the feasibility bounds and sharing methods will lead to maximized utilization of storage system. Besides, the grid system will be further stable and can be used for controller start up in the islanding operation [73, 74, 75,

and 76]. Battery control problem is formulated based on the comprehensive model developed in chapter two and subsequent power sharing analysis in the chapter three. IEEE 34 bus distribution network is used to validate the storage control for various combinations of the RES and storage. Power fluctuations are investigated in such system to provide further stability with the storage system. In the chapter five, power sharing methods that have been proposed in chapter three are verified in IEEE 34 bus based nine-SST system with the developed energy storage controller of this chapter.

4.2. Energy Storage in FREEDM System

Having the storage units can simplify the control design and improve stability in the SST microgrid. As customary, the control in FREEDM system are performed in two layers as shown in Fig. 3.16, each of them operating at different timescale. The fast time-scale control corresponds to the local controllers with which each MG device is endowed, called Intelligent Power Management (IPM) controllers in FREEDM systems. These controllers drive the devices to a given operation point. On the other hand, a slow time-scale controller—known as Intelligent Energy Management (IEM) layer in FREEDM systems—are in charge of providing the setpoints to the IPM controllers. These setpoints satisfy the system power flow and other physical and economic constraints. The IPM cloud is responsible for updating the set points through power sharing in between the IEM commands, if requires. Fig. 4.1 illustrates the power changes in the FREEDM system during operation. The blue line corresponds to the setpoints fixed by the IEM layer. When given in terms of power, this operation point can be readily translate in terms of currents and voltages. Ideally, the FREEDM system would operate on that point until a new command is provided by the IEM layer. However, this is not realistic since, as shown in the Fig. 4.1, the blue line

might deviate in any direction from the desired operation point. This erratic behavior P^*_{dab} (the net load of the DAB) is due to the variations in L_{dc} affecting the desired operation of the system. To further explain this scenario, let the closed-loop system model be represented by the following equation (4.1).

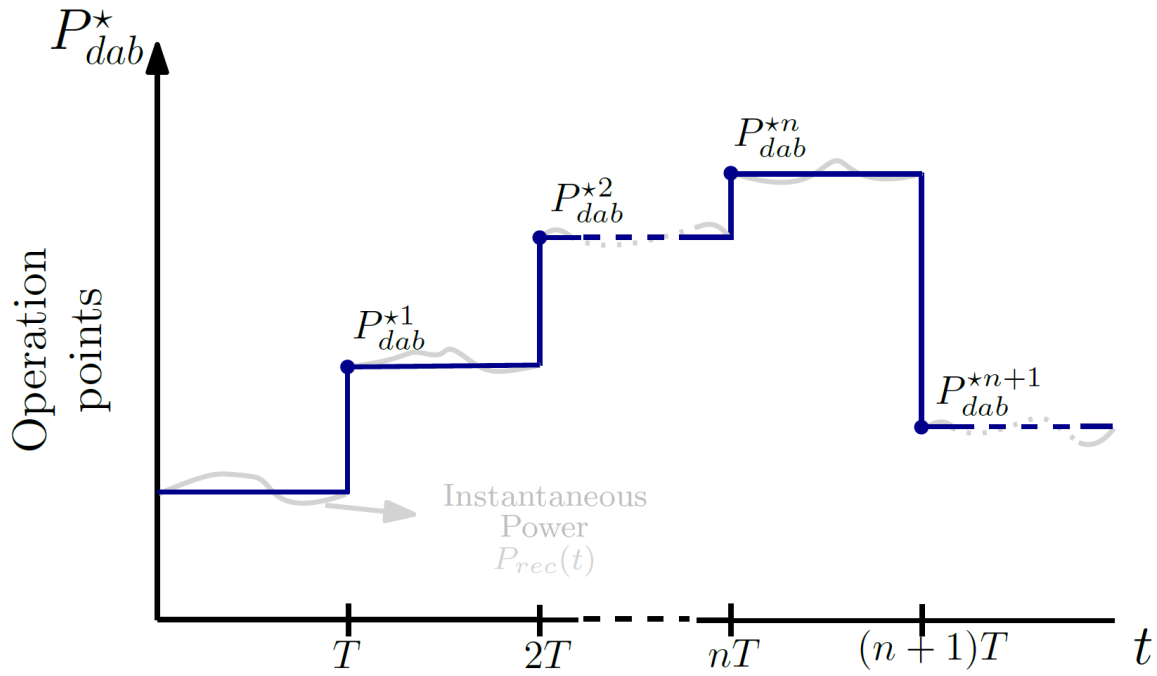

Figure 4.1. Power change scenario in FREEDM system.

$$\dot{x} = f(x, \alpha, u_n) \tag{4.1}$$

Where x is the state (currents and voltages) of the microgrid and x^*_n is the operation point at the n^{th}-update, u_n is the nominal control input vector depending on the operation points and the microgrid net load—i.e. the load seen by the grid. The controller u_n is designed such that x^*_n is an asymptotically stable equilibrium point. This implies that-

$$0 = f(x, \alpha, u_n) \tag{4.2}$$

Any mismatch in the net load invalidates the latter equality. This means that equation (4.2) does not reach the equilibrium as shown in equation (4.3).

$$f(x, \alpha + \varepsilon, u_n) \neq 0 \tag{4.3}$$

Therefore, x_n is not anymore an equilibrium point for the system. Since in a realistic situation, the net load is frequently changing, this mismatching issue is a standard behavior between the intervals $t \in nT, (n+1)T$ with T, the update time as in Fig. 4.1. As a result, the system states of the SST will not merge to the desired equilibrium point. Including storage units in the microgrid adds a degree of freedom permitting to manage the net load changes, assisting to the system stabilization. A simplified representation of the SST driven microgrid is depicted in Fig. 4.2. Both the DC and AC buses in the SST can be integrated with storage, however, in practice the storage will be tied to either one of these buses and so, the DC bus is only considered throughout this section as shown in Fig. 4.2. Rectifier system equations (2.1)-(2.3) are modified to represent in terms of the states of the flow of the current as shown in equations (4.4) – (4.6) and the second harmonics terms are neglected for the steady state analysis. I_{rec} is the net current flown from the rectifier for the rest of the system.

$$\dot{x}_1 = -\frac{a_2}{a_1}x_1 + w_1 x_2 + \frac{1}{a_1}d_1 x_3 - \frac{1}{a_1}y_1 \tag{4.4}$$

$$\dot{x}_2 = -w_1 x_1 - \frac{a_2}{a_1}x_2 + \frac{1}{a_1}d_2 x_3 - \frac{1}{a_1}y_2 \tag{4.5}$$

$$\dot{x}_3 = -\frac{1}{a_3}(d_1 x_1 + d_2 x_2) - \frac{I_{rec}}{a_3} \tag{4.6}$$

Steady-state equations can be written as below from the equations above.

$$-a_2 x_1 + a_1 w_1 x_2 + d_1 x_3 - y_1 = 0 \tag{4.7}$$

$$-a_1 w_1 x_1 - a_2 x_2 + d_2 x_3 - y_2 = 0 \tag{4.8}$$

$$d_1 x_1 + d_2 x_2 + \frac{I_{rec}}{a_3} = 0 \tag{4.9}$$

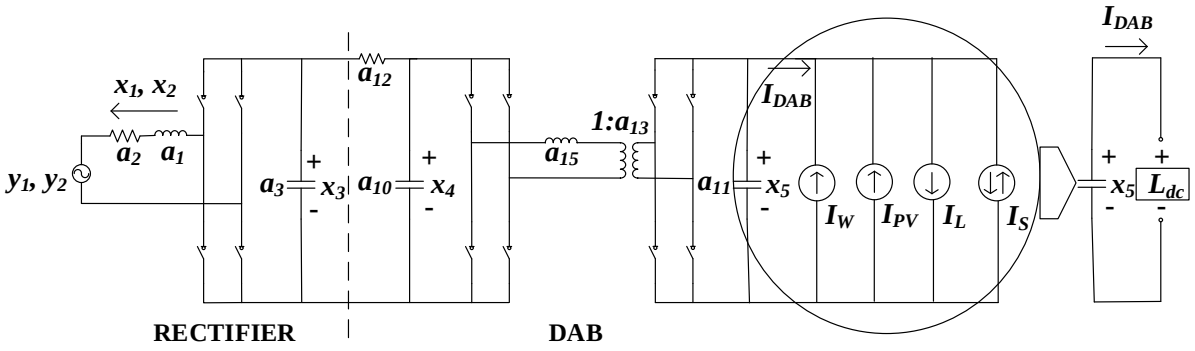

Figure 4.2. SST configuration for energy storage controller.

Replacing with the steady-state values of the rectifier states equations (4.7 – 4.9), equation (4.10) can be formed to find the constraints for the maximum current that can be flown through the rectifier stage of SST.

$$a_2x_1^2 + a_2x_2^2 + y_1x_1 + y_2x_2 + 2r_1I_{rec} = 0$$

$$(x_1\sqrt{a_2} + \frac{y_1}{2\sqrt{a_2}})^2 + (x_2\sqrt{a_2} + \frac{y_2}{2\sqrt{a_2}})^2 = \frac{{y_1}^2 + {y_2}^2}{4a_2} - 2r_1I_{rec}$$

$$(x_1 + \frac{y_1}{2a_2})^2 + (x_2 + \frac{y_2}{2a_2})^2 = \frac{{y_1}^2 + {y_2}^2}{4{a_2}^2} - \frac{2r_1I_{rec}}{a_2} \tag{4.10}$$

Equation (4.10) is very similar to the equation (3.5) and the maximum current that can be flown through the rectifier stage can be find form the radius of the circle equation.

$$I_{rec,max} = \frac{{y_1}^2 + {y_2}^2}{8a_2r_1} \tag{4.11}$$

Considering an ideal lossless system and the steady-state value of the states, equation (4.12) will translate the maximum current flowing through to the rectifier to the maximum current for the DAB stage.

$$r_1 * I_{rec} = r_2 * I_{DAB}$$

$$I_{DAB,max} = \frac{({y_1}^2 + {y_2}^2)}{8a_2r_2} \tag{4.12}$$

Similar constraints can be found utilizing the DAB system equations (2.9)-(2.10).

$$x_4{}^2 - x_4 x_3 + I_{DAB} a_{12} x_5 = 0 \tag{4.13}$$

For a real solution of the equation (4.10), the constraints in equation (4.14) will have to be maintained.

$$x_3{}^2 - 4\, I_{DAB} a_{12} x_5 \geq 0$$

$$I_{DAB} \leq \frac{x_3{}^2}{4 a_{12} x_5} \sim \frac{r_1{}^2}{4 a_{12} r_2} \tag{4.14}$$

Equations (4.12) and (4.14) will lead to the formation of the maximum current that can be passed through the DAB stage of the SST, it is important to mention here that the duty cycle constraints are not considered here.

$$I_{DAB,max} = \min\left(\frac{(y_1{}^2 + y_2{}^2)}{8 a_2 r_2}, \frac{r_1{}^2}{4\, a_{12} r_2}\right) \tag{4.15}$$

Effectively, $y_2 \cong 0$ and so the maximum current flowing through the DAB can be written as in equations (4.16).

$$I_{DAB,max} = \min\left(\frac{y_1{}^2}{8 a_2 r_2}, \frac{r_1{}^2}{4 a_{12} r_2}\right) \tag{4.16}$$

To simplify the problem formulation, current that is flowing through the DAB can be summed up as the net currents drawn by various segments of the system. DAB current is the combination of the current that is flowing through the DRER, DESD and local loads in the DC MG as shown in Fig. 4.2. Equation (4.17) presents the sum of the current flowing through the DAB stage of the SST where DESD current is considered positive while charging and negative while discharging.

$$I_{dab} = I_{bat} - I_{load} + I_{DRER} \tag{4.17}$$

Based on the power changes scenario explained in chapter three, storage controller is developed in the next sections for the first case where the storage will take care of the all the local variations due to change in any current in MG. Next, the developed controller is utilized to implement the power sharing methods of chapter three.

4.3. Input-output Controller for Energy Storage

Storage DESD model consists of electro-chemical battery system which is translated into state equations in terms of an equivalent electrical circuit [51, 52]. DESD model of chapter two is modified to represent as a general model such that the developed controller can be used with any DESD model as the controller requires to be independent of the storage model. A DC-DC bidirectional converter is used to integrate the storage to the DC bus similar to the chapter two, however, the DAB Converter is considered in the present analysis to utilize the DC-DC converter of the SST. The interface circuit is shown in Fig. 4.3. The model equations utilized for the controller development are expressed in equations (4.18)-(4.22).

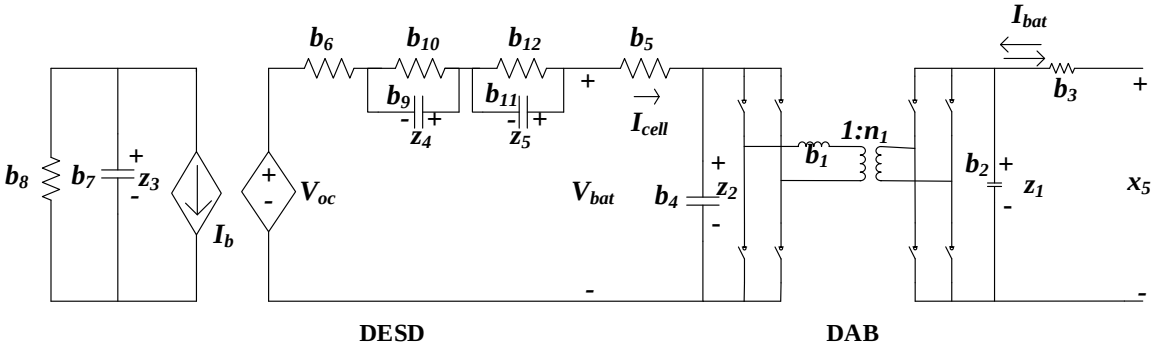

Figure 4.3. DESD interface circuit with DC-DC converter.

$$\dot{z}_1 = -\frac{z_1 - x_5}{b_3 b_2} + \frac{\phi_{bat}(1-\phi_{bat})n_1}{2b_1 b_2 f_s} z_2 \tag{4.18}$$

$$\dot{z}_2 = -\frac{\phi_{bat}(1-\phi_{bat})n_1}{2b_1 b_4 f_s} z_1 + \frac{V_{bat} - z_2}{b_5 b_4} \tag{4.19}$$

$$\dot{z}_3 = -\frac{z_3}{b_7 b_8} + \frac{I_{cell}}{b_7} \tag{4.20}$$

$$\dot{z}_4 = -\frac{4}{b_9 b_{10}} + \frac{I_{cell}}{b_9} \tag{4.21}$$

$$\dot{z}_5 = -\frac{z_5}{b_{11} b_{12}} + \frac{I_{cell}}{b_{11}} \tag{4.22}$$

The system parameters with DESD model and the converter are expressed as ($b_1 - b_{13}$), the phase shift ratio of the converter (ϕ_{bat}) is formulated as feedback gain, u_d and can be expressed as the following:

$$u_d = -\frac{\phi_{bat}(1-\phi_{bat})n_1}{2b_1 f_s} \tag{4.23}$$

The current from the storage is defined as I_{cell} which is defined according to the power balance between the battery and DC bus.

$$I_{cell} = \frac{I_{bat} x_5}{V_{bat}} \tag{4.24}$$

It is important to mention that the storage states dynamics ($z_3 - z_5$) are not dependent on the controller sates ($z_1 - z_2$) rather the dependence comes from I_{bat} which makes the controller design independent of the storage model. Although a detailed analytical model in this study, any storage model is compatible with the developed controller in the next section. Consistent with the physics of the system, the output battery voltage V_{bat} is always bounded. In fact, the battery system includes protection devices to limit the battery operation within an appropriate current and voltage range, avoiding damage on the equipment. Thus, for all time, the assumption has been made that $|V_{bat}| < V_{bat}^{max}$.

4.3.1. Controller Derivation for Energy Storage

When operating, it is required that the net output power in the distribution grid of the i^{th} SST operates at the constant value set by the IEM as shown in equation (4.25).

$$P^*_{dab,i} = I^*_{dab,i} x^*_{5i} \tag{4.25}$$

Here, $P^*_{dab,i}$ represents the power drawn by the DAB stage of the i^{th} SST as we consider the storage controller for all the SSTs in the network. Since the dc link voltage x^*_{5i} is in practice regulated by the DAB converter as discussed in chapter two, the control objective of the DESD is then to regulate the output current to $I^*_{dab,i}$. Representing the DRERs and DESD as current sources as in Fig. 4.4, the next relation follows from the KCL as shown in equation (4.26), like equation (4.17).

$$I_{dab,i} = I_{pv,i} + I_{wind,i} + I_{bat,i} - I_{load,i} \tag{4.26}$$

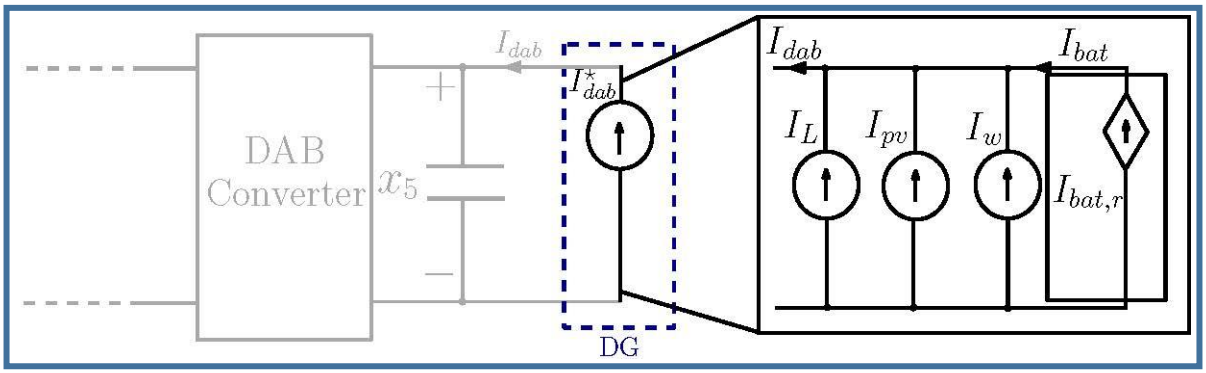

Figure 4.4. Simplified structure of the DC microgrid.

In steady-state operation, equation (4.26) can be written as:

$$I^*_{dab,i} = I_{pv,i} + I_{wind,i} + I^r_{bat,i} - I_{load,i} \tag{4.26}$$

Where, $I^r_{bat,i}$ is the storage output reference current required to maintain $I_{dab,i} = I^*_{dab,i}$, subtracting equation (4.26) to (4.25), following relation can be obtained.

$$I^r_{bat,i} = I_{bat,i} - I_{dab,i} + I^*_{dab,i} \tag{4.27}$$

Thus, the controller introduced in the next paragraph drives $I_{bat,i} \rightarrow I^r_{bat,i}$, as long as the battery capacity permits to do so. During this convergence, a transient tracking error $\delta_{bat,i} \coloneqq I_{bat,i} - I^r_{bat,i}$ is exhibited. This fact is depicted in Fig. 4.4 which corresponds to the circuit diagram of the closed-loop system. Note that $\delta_{dab,i} \coloneqq I_{dab,i} - I^r_{dab,i}$ represents the transient error of $I_{dab,i}$ while converging to $I^*_{dab,i}$. The controller design is presented in this section based on input-output linearization [77]. As a first step, we write $\delta_{bat,i}$ in terms of the system variables in equation (4.28).

$$\delta_{bat,i} = I_{bat,i} - I^r_{bat,i} = \frac{z_{1i} - x_{5i}}{b_{3i}} - I^r_{bat,i} \tag{4.28}$$

Then, the time derivative of the error signal is derived in equation (4.29) as the relative degree respect to $\delta_{bat,i}$ is one.

$$\dot{\delta}_{bat,\imath} = \frac{1}{b_{3i}}(\dot{z_{1\imath}} - \dot{x_{5\imath}}) - \dot{I^r_{bat,\imath}} = \frac{1}{b_{2i}b_{3i}^2}(x_{5i} - z_{1i}) + \frac{1}{b_{2i}b_{3i}} z_{2i} u_{d,i} - \frac{\dot{x_{5\imath}}}{b_{3i}} - \dot{I^r_{bat,\imath}} \tag{4.29}$$

As part of the procedure, the right side of the equation (4.29) is equaled to a proportional constant of the error term, $\delta_{bat,i}$ where $k_{p,i} > 0$.

$$-\frac{k_{p,i}}{b_{2i}b_{3i}}\delta_{bat,i} = -\frac{k_{p,i}}{b_{2i}b_{3i}}\left(\frac{z_{1i} - x_{5i}}{b_{3i}} - I^r_{bat,i}\right)$$

$$\frac{1}{b_{2i}b_{3i}^2}(x_{5i} - z_{1i}) + \frac{1}{b_{2i}b_{3i}} z_{2i} u_{d,i} - \frac{\dot{x_{5\imath}}}{b_{3i}} - \dot{I^r_{bat,\imath}} = -\frac{k_{p,i}}{b_{2i}b_{3i}}\left(\frac{z_{1i} - x_{5i}}{b_{3i}} - I^r_{bat,i}\right) \tag{4.30}$$

Therefore, from equation (4.30), the expression for the $u_{d,i}$ can be found as shown in equation (4.31).

$$u_{d,i} = \frac{1}{z_2 i}\left[\frac{1}{b_{3i}}(1 - k_{p,i})(z_{1i} - x_{5i}) + k_{p,i} I^r_{bat,i} + b_{2i}b_{3i}\dot{I^r_{bat,\imath}} + b_{2i}\Psi_{x_{5i}}(t, \phi_{3i})\right] \tag{4.31}$$

Defining a new $\Psi_{x_{5i}}(t, \phi_{3i})$ function as the time derivative of $\dot{x_{5\imath}}$ from equation (2.12) as the following:

$$\Psi_{x_{5i}}(t,\phi_{3i}) = \frac{\phi_{3i}(1-\phi_{3i})a_{13i}}{2a_{11i}a_{14i}a_{15i}}x_{4i} - \frac{1}{a_{11}}I_{dab.i} \tag{4.32}$$

Finally, the duty cycle that is required for the DESD converter to track the current reference can be found substituting equation (4.31) into equation (4.23).

$$\frac{\phi_{bat,i}(1-\phi_{bat,i})b_{12i}}{2b_{13i}b_{1i}}$$

$$= \frac{1}{z_{2i}}\left[\frac{1}{b_{3i}}(1-k_{p,i})(z_{1i}-x_{5i}) + b_{2i}b_{3i}\dot{I^r_{bat,\iota}} + k_{p,i}I^r_{bat,i} + b_{2i}\dot{x_{5\iota}}\right] \tag{4.33}$$

Eventually, equation (4.33) corresponds to quadratic equation with the phase shift ratio, $\phi_{bat,i}$ as the variable and the roots are the following:

$$\phi_{bat,i} = \begin{cases} -\frac{1}{2} \pm \frac{1}{2}\sqrt{1-4h_i} & u_{d,i} \in \left[0, \frac{n_i}{8f_{s,i}b_{1i}}\right] \\ -\frac{1}{2} - \frac{1}{2}\sqrt{1-4h_i} & u_{d,i} \in \left[-\frac{n_i}{f_{s,i}b_{1i}}, 0\right] \end{cases} \tag{4.34}$$

$$h_i = \frac{2f_{s,i}b_{1i}}{n_i}u_{d,i} \tag{4.35}$$

The implementation diagram is depicted in Fig. 4.5. Notice that, to calculate $I^r_{bat,i}$, measurements of currents $I_{dab,i}$; $I_{bat,i}$ and voltage x_{5i} are required. To obtain the time-derivative of $I^r_{bat,i}$, the signal is passed through a low-pass filter to eliminate noise. To have admissible duty cycle values between -1 and 1, a saturation block has been added.

4.3.2. Stability of Energy Storage Controller with Multiple SSTs

As the DESD system has relative degree of one with respect to $\delta_{bat,i}$, it is critical to proof the system is stable with the developed controller and do so, stability of the overall system is addressed in the proposition below.

Fact 1: Signal $I_{bat,i}^{r}$ and $I_{bat,\iota}^{r\cdot}$ are bounded and, for any operation around the equilibrium point, x_{5i} and ϕ_{3i} are also bounded.

Boundedness of x_{5i} and ϕ_{3i} follows proving, in the sequel, stability of the multi-SST system around the equilibrium. At this point, that assertion is taken as a fact. In the same way, as currents $I_{wind,i}$, $I_{pv,i}$ and $I_{load,i}$ are bounded currents and so the generated power by the DRERs and consumed by the load is also limited, $I_{bat,i}^{r}$ is also bounded.

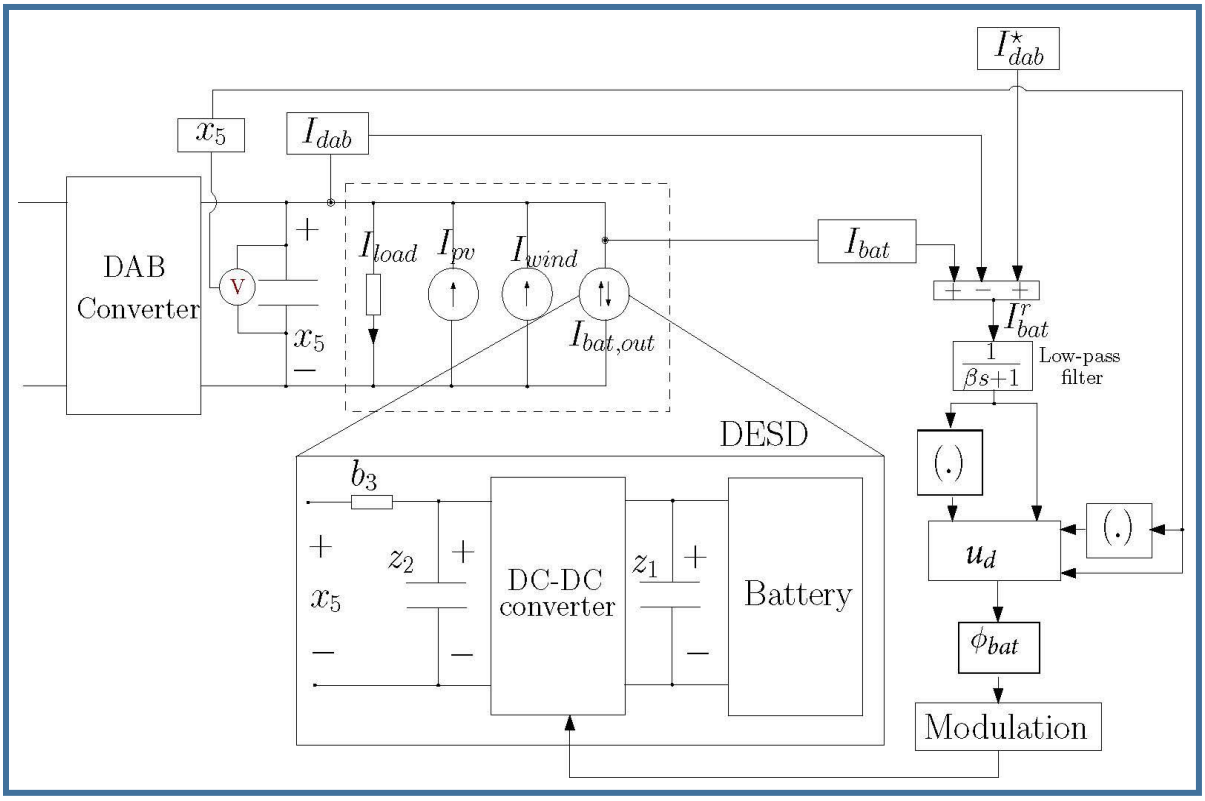

Figure 4.5. Controller implementation diagram.

Since, renewable sources are also coupled to the DC grid with filters, it is reasonable to consider $I_{bat,\iota}^{r\cdot}$ to be bounded.

Proposition 1: Consider the DESD system in equations (4.18-4.19) in closed-loop with feedback gain ($u_{d,i}$), the following function $p_i(t)$ is defined:

$$p_i(t) = z_{1i}\left[\frac{1}{b_{3i}}(1-k_{p,i})(z_{1i}-x_{5i}) + b_{2i}b_{3i}\dot{I^r_{bat,\iota}} + k_{p,i}I^r_{bat,i} + b_{2i}\dot{x_{5\iota}}\right] \quad (4.36)$$

Then, the following claims can be made,

C1. The tracking error $\delta_{bat,i}$ is exponentially convergent, namely,

$$\delta_{bat,i}(t) = \lim_{t\to\infty}\delta_{bat,i}(t_0)\exp(-\frac{k_{p,i}}{b_{3i}b_{2i}}t) \quad (4.37)$$

C2. There exists a bound $|p_i(t)| \le p_{max,i}$ such that for all initial conditions $(z_{1i}(0), z_{2i}(0)) \in \hat{\mathrm{R}}^2$ with $z_{2i}(0) > \frac{1}{2}V^{min}_{bat,i} - \frac{1}{2}\sqrt{V^{min\,2}_{bat,i} - 4b_{4i}p_{max,i}}$ and $V^{min\,2}_{bat,i} - 4b_{4i}p_{max,i} \ge 0$, the system trajectories are bounded. Moreover, there exists parameters $f_{s,i}$, b_{1i} and n_i such that:

$$u_{d,i} \in \left[-\frac{n_i}{f_{s,i}b_{1i}}, \frac{n_i}{8f_{s,i}b_{1i}}\right] \quad (4.38)$$

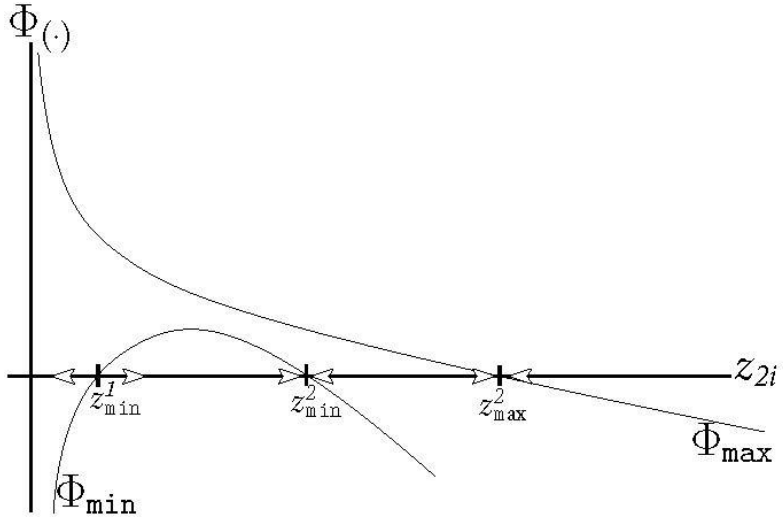

Figure 4.6. Plot for the stability functions.

Proof: The closed-loop system is formed by the error dynamics together with the feedback gain as follows:

$$\dot{\delta_{bat,\iota}} = -\frac{k_{p,i}}{b_{2i}b_{3i}}\delta_{bat,i} \quad (4.39)$$

$$\dot{z_{2i}} = -\frac{z_{2i}}{b_{4i}b_{5i}} - \frac{p_i}{b_{4i}z_{2i}} + \frac{V_{bat,i}}{b_{4i}b_{5i}} \tag{4.40}$$

Thus, claim C1 immediately follows. Next, using the Fact 1, boundedness of z_{1i} can be concluded and subsequently, the existence of $p_{max,i}$ follows. Similarly for $z_{2i} > 0$,

$$\Phi_{min}(z_{2i}) < \dot{z_{2i}} < \Phi_{max}(z_{2i}) \tag{4.41}$$

Where the definitions of the functions Φ_{min} and Φ_{max} are provided below.

$$\Phi_{min}(z_{2i}) = -\frac{z_{2i}}{b_{4i}b_{5i}} - \frac{p_{max,i}}{b_{4i}z_{2i}} + \frac{V_{bat,i}^{min}}{b_{4i}b_{5i}} \tag{4.42}$$

$$\Phi_{max}(z_{2i}) = -\frac{z_{2i}}{b_{4i}b_{5i}} + \frac{p_{max,i}}{b_{4i}z_{2i}} + \frac{V_{bat,i}^{max}}{b_{4i}b_{5i}} \tag{4.43}$$

The corresponding plots of the functions are shown in Fig. 4.6 where the points z_{min}^1 and z_{min}^2 are the roots of equation (4.42), and z_{max}^2 is a root of equation (4.43).

$$z_{min}^{1,2} = \frac{1}{2}V_{bat,i}^{min} \pm \frac{1}{2}\sqrt{{V_{bat,i}^{min}}^2 - 4b_{4i}p_{max,i}} \tag{4.44}$$

$$z_{max}^2 = \frac{1}{2}V_{bat,i}^{max} \pm \frac{1}{2}\sqrt{{V_{bat,i}^{max}}^2 + 4b_{4i}p_{max,i}} \tag{4.45}$$

The following systems are considered for the boundedness proof:

$$\dot{z_{2i,min}} = \Phi_{min}(z_{2i,min}) \tag{4.46}$$

$$\dot{z_{2i,max}} = \Phi_{max}(z_{2i,max}) \tag{4.47}$$

Thus, by the Comparison Lemma [78], for all $z_{2i}(t) > 0$, it follows that

$$z_{2i,min}(t) < z_{2i}(t) < z_{2i,max}(t) \tag{4.48}$$

For all $z_{2i,min}(0) > z_{min}^1$, $z_{2i,min}(t)$ is stable, remains positive and converges to z_{min}^2. Similarly, for all $z_{2i,max}(0) > 0$, $z_{2i,max}(t)$ stays positive and converges to z_{max}^2. The, with z_{min}^1, claim C2 follows, furthermore, z_{2i} is always positive. Finally, since $z_{2i}(t)$is never zero, $u_{d,i}$ is bounded and so, there exists free parameters satisfying equation (4.38).

Besides, the local stability of the storage system, it is also required to proof that the designed controller maintains the global stability and does not have any impact on the microgrid network being a completely decentralized local controller. To show the stable operation of the SST microgrid, dynamic models of rectifier and DAB in chapter two are considered. However, to express the system equations completely in term so the system states, equations (2.3) and (2.12) are changed to the following for any i^{th} SST:

$$\dot{x}_{3i} = -\frac{1}{2a_{3i}}(d_{1i}x_{1i} + d_{2i}x_{2i}) - \frac{x_{3i} - x_{4i}}{a_{3i}} \tag{4.49}$$

$$\dot{x}_{5i} = \frac{\phi_{3i}(1-\phi_{3i})a_{13i}}{2a_{11i}a_{14i}a_{15i}}x_{4i} - \frac{1}{a_{11i}}I^*_{dab,i} - \frac{1}{a_{11i}}\delta_{bat,i} \tag{4.50}$$

For equation (4.49), second order harmonics are neglected as the analysis is based on the fundamental frequency response (the full model with the harmonics are considered in the simulation) and for equation (4.50), current $I_{dab,i} = I^*_{dab,i} + \delta_{bat,i}$ is considered. Eventually, the closed loop of the each SST with rectifier and DAB is formed by 9 physical and controller states. For the sake of simplicity, the proof here is analyzed considering two SSTs. As it is clear from equation (4.50) that the SST dynamics are connected in cascade with storage dynamics and the overall system dynamics for SST and storage can be expressed as follows:

$$\begin{bmatrix} \dot{\eta} \\ \dot{\delta}_{bat} \end{bmatrix} = \begin{bmatrix} \phi(\alpha_c, \eta) \\ K_P\delta_{bat} \end{bmatrix} + \begin{bmatrix} P \\ 0 \end{bmatrix}\delta_{bat} \tag{4.51}$$

For the storage controller, only the dynamics due to the error term is considered as z_{2i} dynamics is stable and no other system dynamics of matrix equation (4.51) depends on it. $\phi(\alpha_c, \eta)$: $\hat{\mathrm{R}}^{18} \rightarrow \hat{\mathrm{R}}^{18}$ is a nonlinear function representing the feedback system depending on the rectifier and DAB converter of each MG and their control variables, $\eta^T = [\eta_1^T \quad \eta_2^T] \in$

$\hat{\mathrm{R}}^{18}$ and constant vector α_c stands for controller parameters, namely, the proportional and integral gains. For two SST model, $i = \{1,2\}$, $\eta_1^T = [x_i^T \quad \xi_i^T]$ and $x_i^T = [x_{1i} \ldots x_{5i}]$ and $\xi_i^T = [\xi_{1i} \ldots \xi_{4i}]$. For the storage, $\delta_{bat}^T = [\delta_{bat,1} \ \delta_{bat,2}]$ and the constant matrix $P = \left[\frac{1}{a_{11,1}} v_5 \quad \frac{1}{a_{11,2}} v_{14}\right] \in \hat{\mathrm{R}}^{18*2}$ ($v_j \in \hat{\mathrm{R}}^{18}$ is a vector of the Euclidean basis where its j^{th} element equals one) and $K_P = diag\ (-\frac{k_{p,1}}{b_{21}b_{31}}, -\frac{k_{p,2}}{b_{22}b_{32}})$. A standard procedure to study the system stability is by means of a local analysis around the equilibrium point of interest. Then, the linearization of (4.51) corresponds to the following matrix formulation.

$$\begin{bmatrix} \dot{\delta\eta} \\ \dot{\delta_{bat}} \end{bmatrix} = \begin{bmatrix} \Psi & P \\ 0 & K_P \end{bmatrix} \begin{bmatrix} \delta\eta \\ \delta_{bat} \end{bmatrix} \tag{4.52}$$

The linearization matrix, $\Psi \in \hat{\mathrm{R}}^{18*18}$ is evaluated at the equilibrium point as shown in equation (4.53).

$$\Psi = \frac{\delta\phi(\eta)}{\delta\eta} \mid_{\eta=\eta^*} \tag{4.53}$$

It is obvious from equation (4.52) that the eigenvalue of linear system will be $eig\{\Psi\} \cup \{-\frac{k_{p,1}}{b_{21}b_{31}}, -\frac{k_{p,2}}{b_{22}b_{32}}\}$. So, if the PI gains of the SST which is the vector α_c is selected such that $Re\ [eig\{\Psi\}] < 0$, then the closed loop stability of the SST with storage will follows. The similar analysis can be extended for the n-SST system. This section eventually confirms that the storage controller will not create any issues in terms of stability in the microgrid as long as the SST controllers are stable.

4.4. Storage Controller for Power Sharing Methods

This section is intended to develop storage controller that not only mitigates/eliminates the variations due to the inclusion of renewable energy sources in individual SST but also supports the power sharing through SST in case of sudden load changes when running the power flow is not practical. Broadly, load change during the IPM operation in FREEDM can be categorized in two cases as shown in Fig. 4.7 (detailed version of Fig. 3.4). The local storage at each SST will support as long as the power change scenario is within the case 0 bound and the storage in other SSTs will come into support when it goes beyond case 0. In previous section, the storage controller is designed considering the storage is capable of managing the local power demand in order to maintain $I_{dab,i} = I^*_{dab,i}$ despite of the variations in the renewable resources and load; this means that no external assistance is needed. If the net load increases then the storage can discharge and provide the slack. Otherwise, the storage can charge and consume the slack when load drops. As long as the local storage capacity is sufficient to support the load changes in MG, $I_{dab,i}$ will converge to $I^*_{dab,i}$ and the total input power seen by the rectifier $P_{rec,i}$ will remain the same which is defined as following:

$$P_{rec,i} = \frac{x_{5i}^2}{L_{dc,i}} + \frac{(x_{3i} - x_{4i})^2}{a_{13i}} \tag{4.54}$$

$L_{dc,i}$ which is the equivalent power load representing the energy cell components can be defined as $\frac{x_{5i}}{I_{dab,i}}$. However, as the capacity of the i^{th} storage reaches to the saturation then $I_{dab,i}$ will not converge to $I^*_{dab,i}$ which will require the support from the other SSTs in the network. Generally, as the required power to compensate the local changes overpasses the storage limitations, the required excess load can be assisted by storage devices installed in

other SSTs in the network. When the local storage fails to support the change then $L_{dc,i}$ is changed which eventually changes $P_{rec,i}$ and subsequently the change is seen in the node voltage and input current of the SSTs as shown in (3.8). Any change in x_{1i} or y_{1i} of i^{th} SST will also impact other SSTs in the network and so the power setpoints require recalculation through power flow solver. To avoid this complexity and delay of power flow solver, power sharing methods for multi-SST systems are developed in chapter three to properly update the input current and node voltage of each SST whenever there is a change in the load demand of one of the SSTs.

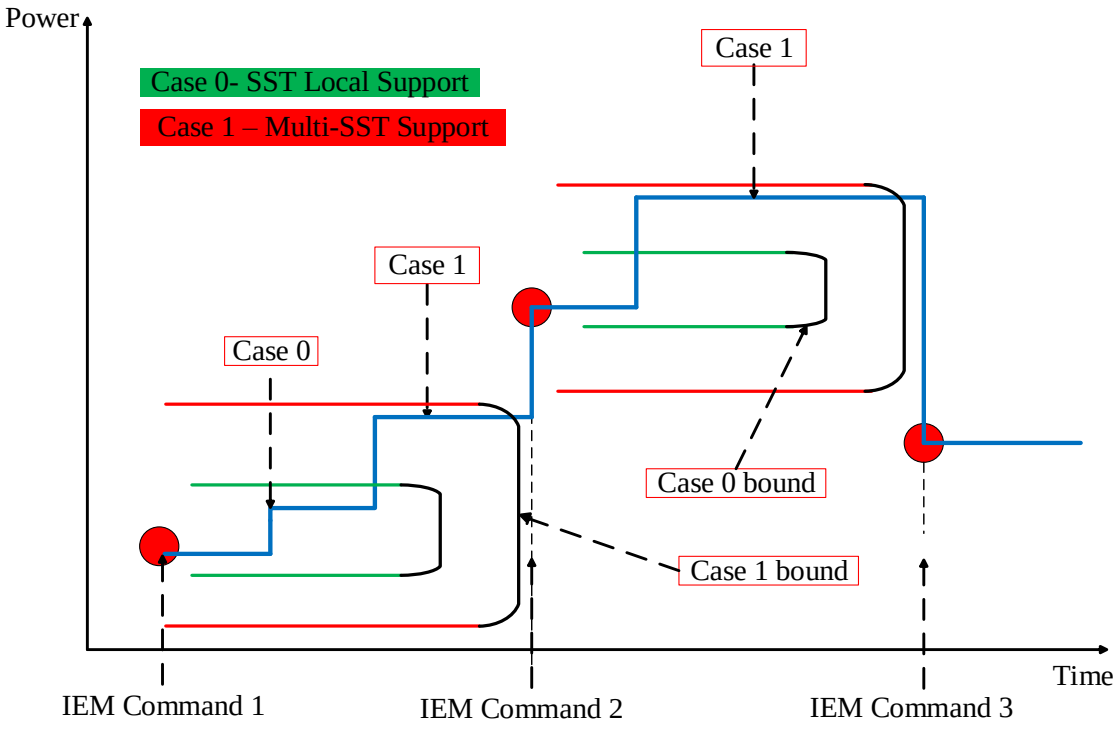

Figure 4.7. Load change cases in FREEDM system.

However, the implementation of the power sharing was not discussed and the developed storage controller is extended to enable power sharing methods in a multi-SST network. The main question here is - how can the controllers be utilized for multiple storage units so that the slack created from the load in one MG can be cooperatively fulfilled by itself as well as

its neighboring MGs. In the following subsections, actuation of the storage controller for the both power sharing methods are described briefly.

4.4.1. Storage Controller Implementation for Power Sharing Method 1

In this method, the input current of the other SSTs remain unchanged as there is a sudden big change in i^{th} SST that cannot be supported by the local storage unit which is described in details in chapter 3, section 3.3.1. The voltage of all the SSTs update to new value as a function of the change in power of i^{th} SST. The analytical expressions of the change in input current of i^{th} SST is expressed in equation (3.17) and change in voltage of the i^{th} SST can be written as follows

$$\Delta y_{1i} + j\Delta y_{2i} = (\Delta x_{1i} + j\Delta x_{2i}) \sum_{k=1}^{i} (r_k + jx_k)\,. \tag{4.55}$$

For method one, the voltage drop of all other SSTs in the network will be same as the i^{th} SST for maintaining the same input current. Based on this change in node voltage, $P_{rec,j}$, $j \to \{1 \dots n\}, j \neq i$ will be updated following (3.8) and then $I^{*}_{dab,j}$ for all the SSTs will be updated as follows:

$$I^{*}_{dab,j} = \frac{P_{rec,j} - \dfrac{(x_{3j} - x_{4j})^2}{a_{13j}}}{x_{5j}} \tag{4.56}$$

Based on this new $I^{*}_{dab,j}$, $I^{r}_{bat,j}$ for all other SSTs will be updated as follows which is similar to equation (4.26).

$$I^{r}_{bat,j} = I^{r}_{bat,j} - I_{pv,j} - I_{wind,j} + I_{load,j} \tag{4.57}$$

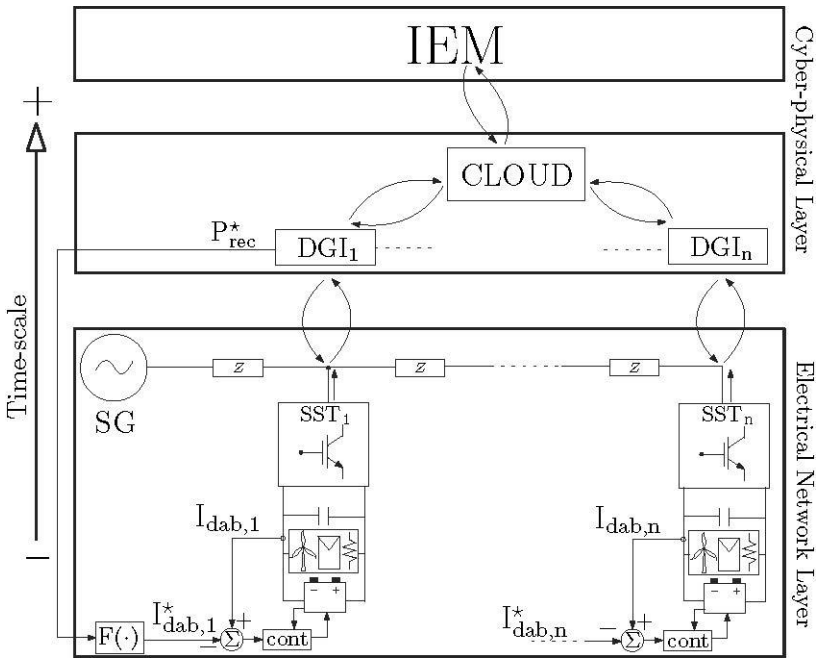

Figure 4.8. Power sharing implementation in cyber-physical layer.

Based on this updated values of $I^{r}_{bat,j}$, the change in power of i^{th} SST will be compensated by the whole network. The implementation diagram of the power sharing for both methods are shown in Fig. 4.8. The IPM cloud interface will be responsible for calculating the updated $P_{rec,j}$ for all the SSTs in the network based on the change in i^{th} SST, in this way of implementation, operation data like node voltage, input current, and battery health (SOC) require to be passed to the central cloud through the distributed grid intelligence (DGI) located at east SST. The computational delay can provide incorrect setpoints and the system might see some oscillations during those period which is demonstrated in the simulation proof of this concept in chapter five. However, other than the communication delay, the setpoint calculation is instantaneous and can be done in faster time scale of 5µs.

4.4.2. Storage Controller Implementation for Power Sharing Method 2

An alternative method two can maintain feasible operation through constant node voltage of all other SSTs when there is any change in i^{th} SST which cannot be supported by the local storage. However, it is found that to maintain the voltage same as it was before, only the input current references of $(i-1)^{th}$ SST, i^{th} SST and $(i+1)^{th}$ SST change and the other setpoints remain the same as described in section 3.3.2. The updated input current set points for the neighboring SSTs are a function of the current of the i^{th} SST. $I^{*}_{dab,j}$ and then $I^{r}_{bat,j}$ similar to method one will be updated for method two to compensate for the changes in the i^{th} SST. However, in this method only the immediate neighbors share the burden and it is not justified to ask for support to the immediate neighbors in case of a sudden big change when all of the neighbors are equipped with the storage system. Although, this method allows uninterrupted operation in the grid network as the total power seen by the distribution grid remains unchanged. We provide results with both methods in this work and the simulations results are provided in the chapter five. In this case, only the information from the neighbors will be required as the immediate neighbors get impacted by method two.

4.5. Validation of the Storage Controller

The proposed storage controller is next validated using simulations on a radial 9-bus distribution feeder model containing a total of 9 SSTs, one at each bus similar to section 3.4. The tie-line impedances of this model are based on the IEEE 34 bus distribution system (details of the IEEE 34 bus are provided in chapter five), and are provided in Table 3.1. The SST models are considered to be identical to each other. First, results are provided to observe

the tracking performance of energy storage with added stochastic uncertainties to the loads and distributed sources through the wind and solar energy. Then, results with the designed controller are explained in chapter five to enable the power sharing in case of sudden big change in the system.

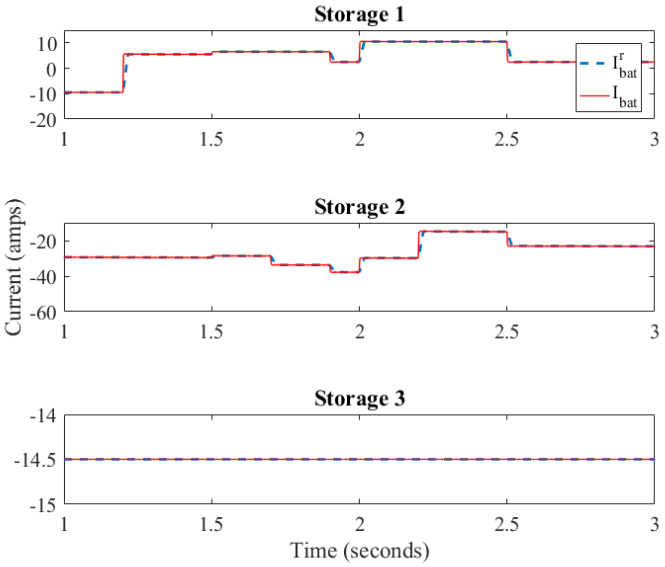

Figure 4.9. Storage profile for SST 1 to SST 3.

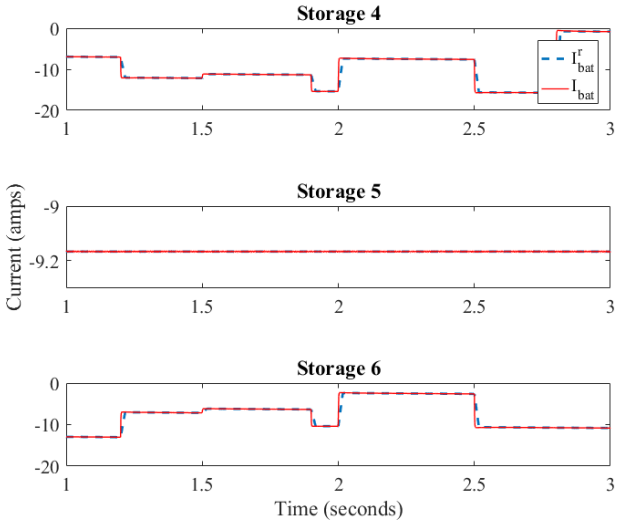

Figure 4.10. Storage profile for SST 4 to SST 6.

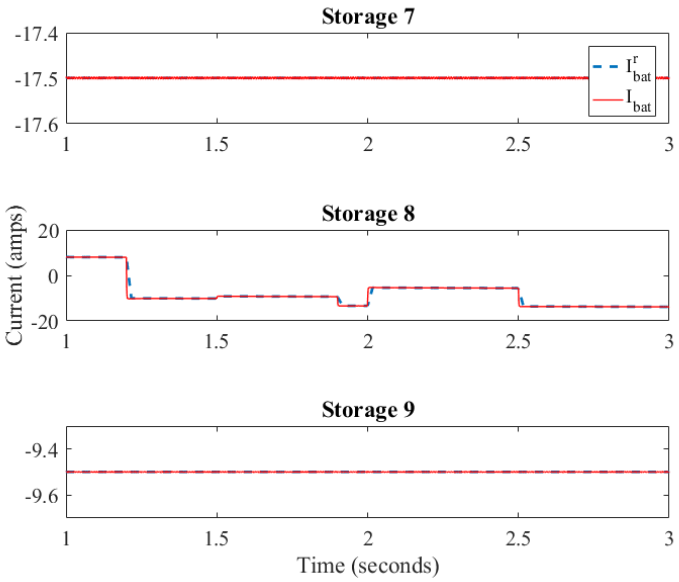

Figure 4.11. Storage profile for SST 7 to SST 9.

The simulation starts with a nominal load of 1 kW at time t = 0 sec in SST 1, 3, 4, 5, 6 and 7. SST 2 starts with 10 kW and SST 8 and 9 with -1 kW. Load and renewable generation are changed in all the SSTs except the SST 3, 5, 7 and 9. The storage response to the dynamic I^r_{bat} is observed in Figures 4.9, 4.10, and 4.11. It is found for all the SSTs, the storage current is perfectly following the reference for any changes in the system. The dotted and solid line present the I^r_{bat} and I_{bat} respectively in the figures. When there is no change in the system then I^r_{bat} remains the same flat line as shown for storage 3, 5, 7 and 9. One of the purpose of designing this controller is to regulate the DC bus voltage steadily with all the changes in the system, Figures 4.12 to 4.14 show that the DAB output voltage for SST 1 to 9 are regulated steadily at the desired 400 volts even though there are variations in the MG. It is important to notice here with a traditional PI controller, DC bus voltage has transient overshoot as shown in chapter two in Fig. 2.7 where the storage controller doesn't cancel out the impact of sudden change in power for renewable generation or load changes.

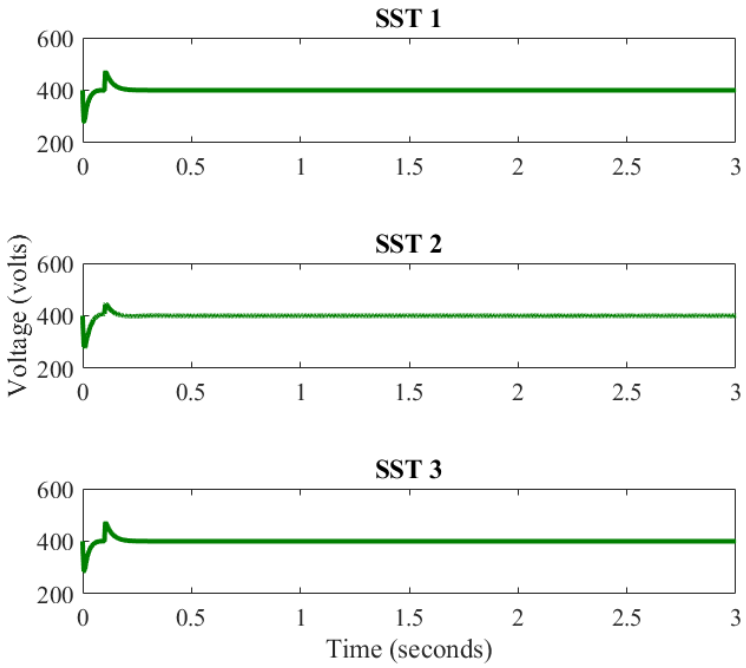

Figure 4.12. DAB output voltage profile for SST 1 to SST 3.

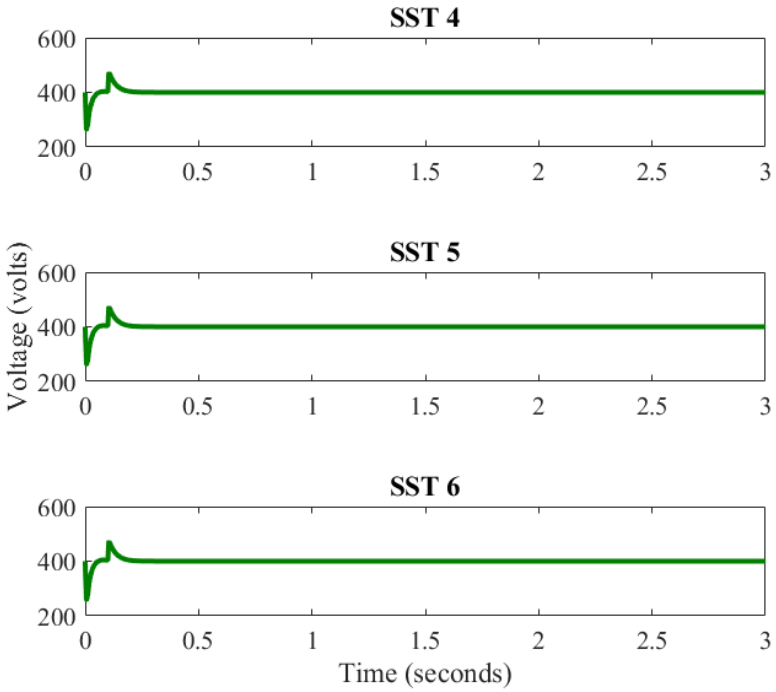

Figure 4.13. DAB output voltage profile for SST 4 to SST 6.

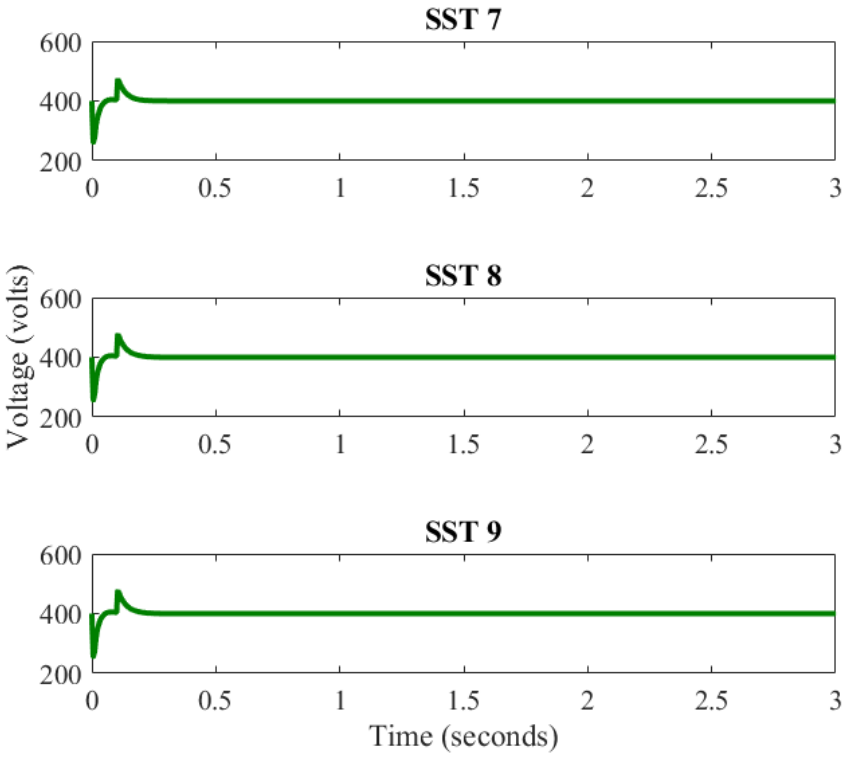

Figure 4.14. DAB output voltage profile for SST 7 to SST 9.

Developed input-output controller maintains the steady-state regulation of the SST states by adjusting the reference current of the storage as a function of time which will be beneficial for the grid side management with high penetration of renewables. Rectifier output voltage of all the SSTs are also observed in Figures 4.15 to 4.17 to show that the steady-state regulation of the rectifier is maintained to its desired regulation point of 6100 volts. Rectifier output voltage is critical to maintain the grid stability and the results show that even with random load change and renewable generation, the storage controller is able to assist in regulation of the SST states. In the next chapter, power sharing results with the developed controller are provided for the large scale simulation considering IEEE 34 bus with 9 SSTs.

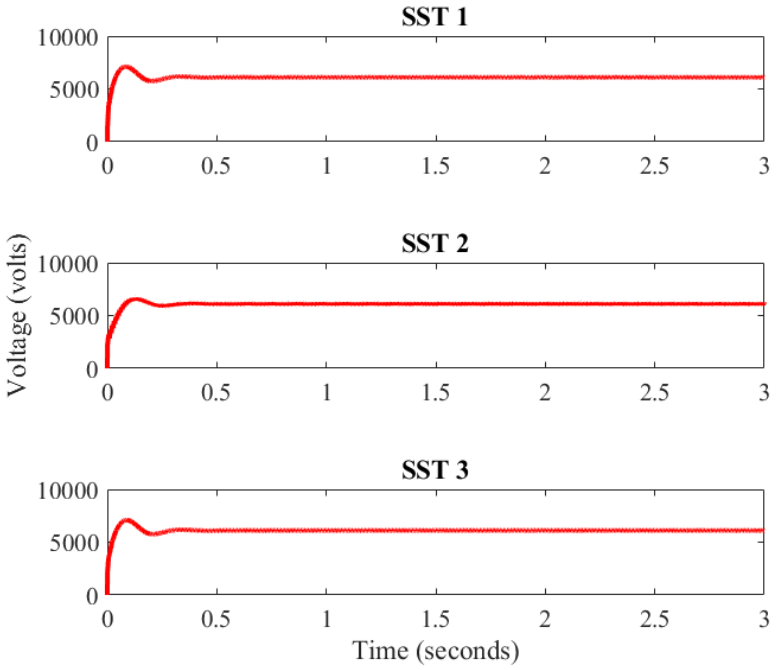

Figure 4.15. Rectifier output voltage profile for SST 1 to SST 3.

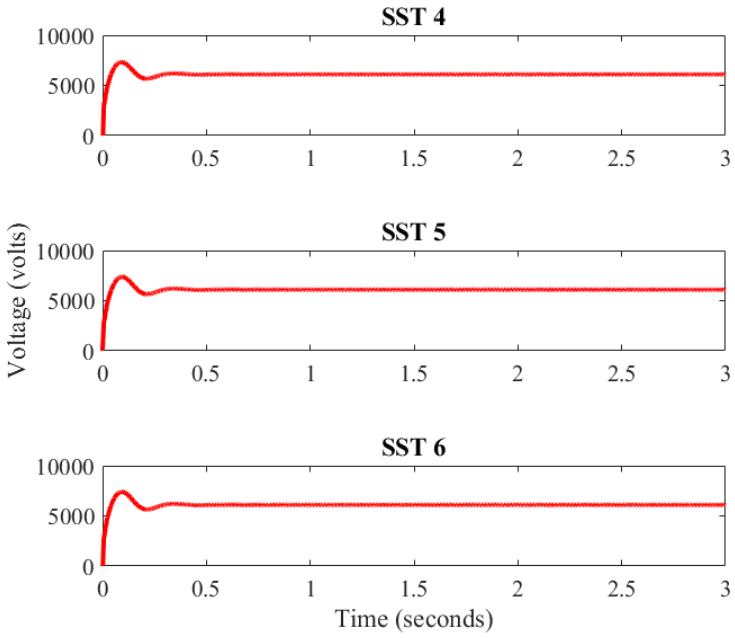

Figure 4.16. Rectifier output voltage profile for SST 4 to SST 6.

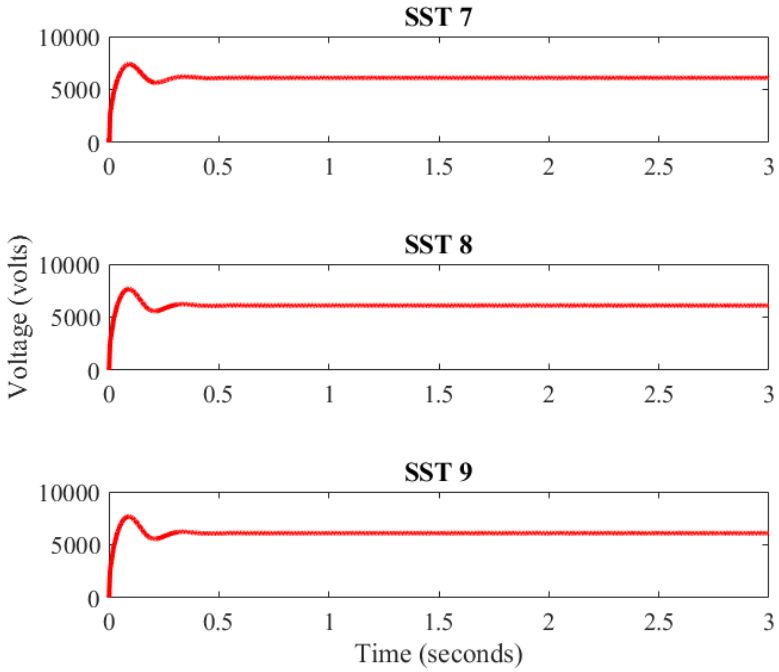

Figure 4.17. Rectifier output voltage profile for SST 7 to SST 9.

4.5. Contribution

1. Design of storage controller for FREEDM system based on nonlinear input-output method to compensate the dynamic variation of the load change and renewable generation. The controller is developed such that the steady-state regulations of the SST can be maintained without any transient.

2. Extension of the developed controller to enable the power sharing methods of chapter three. The storage controller supports power sharing when the local storage is unable to handle the changes. The power sharing methods with storage controller will not require to run the power flow during the IPM operation.

3. Stability of the controller is proven locally and then proof is provided showing that the developed controller does not impact the global stability of the connected SST network as long as the SST controller is stable.

4. Controller design is validated in a 9 SST connected network where the dynamic variation of load and renewable generation are added to observe the storage response with the controller. Also, the steady-state regulation of the SST states are observed with the storage controller which shows the flat regulation of the SST states can be achieved even with presence of dynamic variation in the MG.

4.6. Conclusions

Energy storage is becoming an integral part of the MG in present power grid structure. Bulk energy storage is deployed in many utilities in recent years, besides, distribution sited storage solution is also getting notable interest for improving the grid stability by local control. Energy storage in the residential houses can also support the power grid acting as an additional slack to consume extra power or providing it as required. Efficient control of the energy storage can also reduce the maintenance cost for the transmission grid with high penetration of renewables. For all these benefits, dynamic control of the storage becomes a critical topic of interest where the storage will not only provide the support as back-up power but also assist in maintaining steady-state regulation of the power electronic interface circuits connected to the grid. This chapter proposes a framework for dynamic storage control considering the intermittent behavior of the renewable energy and sudden load change. Most importantly, MG structure and dynamic model of the power processing units like SST are also considered in the proposed work to coordinate all the components required for storage integration. Storage control is also then extended for the power sharing methods developed in chapter three which can be useful in implementing virtual power plant (VPP) concept with FREEDM system. Proof of the stability is provided to show that the MG stability will be uncompromised with the developed controller as long as the power electronics interface

circuit is stable. This work will have further impacts in finding the communication framework required for future mass penetration of storage with renewable energy as communication delay plays an important role in setting up accurate operational points.

CHAPTER 5

SYSTEM SIMULATION IN IEEE 34 BUS DISTRIBUTION NETWORK

5.1. Introduction

5.2. IEEE 34 Bus System Model and Description

5.3. Feasibility Analysis in IEEE 34 Bus

5.4. Implementation of Power Sharing Methods in IEEE 34 Bus

5.5. Contribution

5.6. Conclusions

5.1. Introduction

A large scale system simulation (LSSS) testbed has been built for a distribution network considering the IEEE 34 bus system [28]. PSCAD platform is used to build the distribution network where 40 single-phase SSTs are placed in different phase nodes of the different feeders. The system distributed generator, energy storage, and SSTs are based on the average models as developed in chapter two.

LSSS testbed is used to verify the FREEDM system feasibility constraints obtained from fundamental analysis of chapter two. Then the modified version of the bus is used to verify the power sharing methods in chapter three with the energy storage controller of chapter four. The controller is applied in the modified IEEE 34 bus model to verify the power sharing methods in this chapter. The system level simulation is important to validate the developed controller for a practical comparison and can be utilized in hardware implementation.

5.2. IEEE 34 Bus System Model and Description

SSTs are connected in single phases of a 7.2 KV (3 PH, L-N) distribution feeder. Each SST is rated for 20 KVA (rating is defined by the hardware parameters). Voltage levels for DC and AC buses are maintained at 400 V DC and 120 V AC, respectively. Fig. 5.1 shows the simplified model that is used to build the IEEE 34 bus system for the analysis. Simulation analysis is carried out to observe the feasibility conditions that is discussed in chapter two.

Each node of the network consists of the average model of SST with energy cells as shown in node 810 in Fig. 5.2.

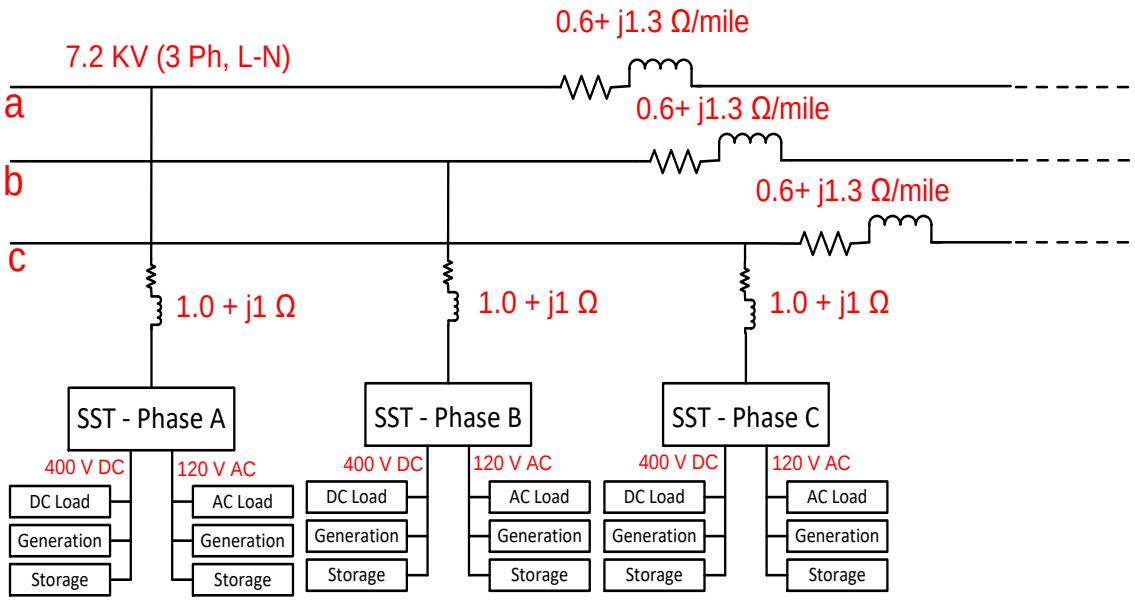

Figure 5.1: PSCAD circuit model for the IEEE 34 bus with SSTs.

5.3 Feasibility Analysis in IEEE 34 Bus

The comprehensive single-SST average model has been incorporated in an IEEE 34 bus large scale system simulation (LSSS) testbed in a PSCAD platform with multiple SSTs for a scaled analysis of the system. The developed multi-SST simulation model is used to find the feasible operating bounds of the system considering the coupling and interaction among multiple SSTs in the distribution system. The LSSS testbed shown in Fig. 5.2 has 26 nodes where each node has one or more SSTs in different phases with the configuration shown in Fig. 2.2. Fig. 5.3 represents a screen shot of the developed model in PSCAD. There are a total of 40 SSTs connected in the various nodes of the LSSS testbed. In this LSSS testbed, only PV DRER is considered along with DESD. Simulation analysis has been carried out to validate the feasibility conditions analyzed in the chapter two through analytical means. Feasibility constraints developed from the theoretical analysis are verified with LSSS model

in this chapter for a full model with microgrid. The local loads are set as 10 Ω (ohms) both in the DC and AC cells for the system simulation in each SST.

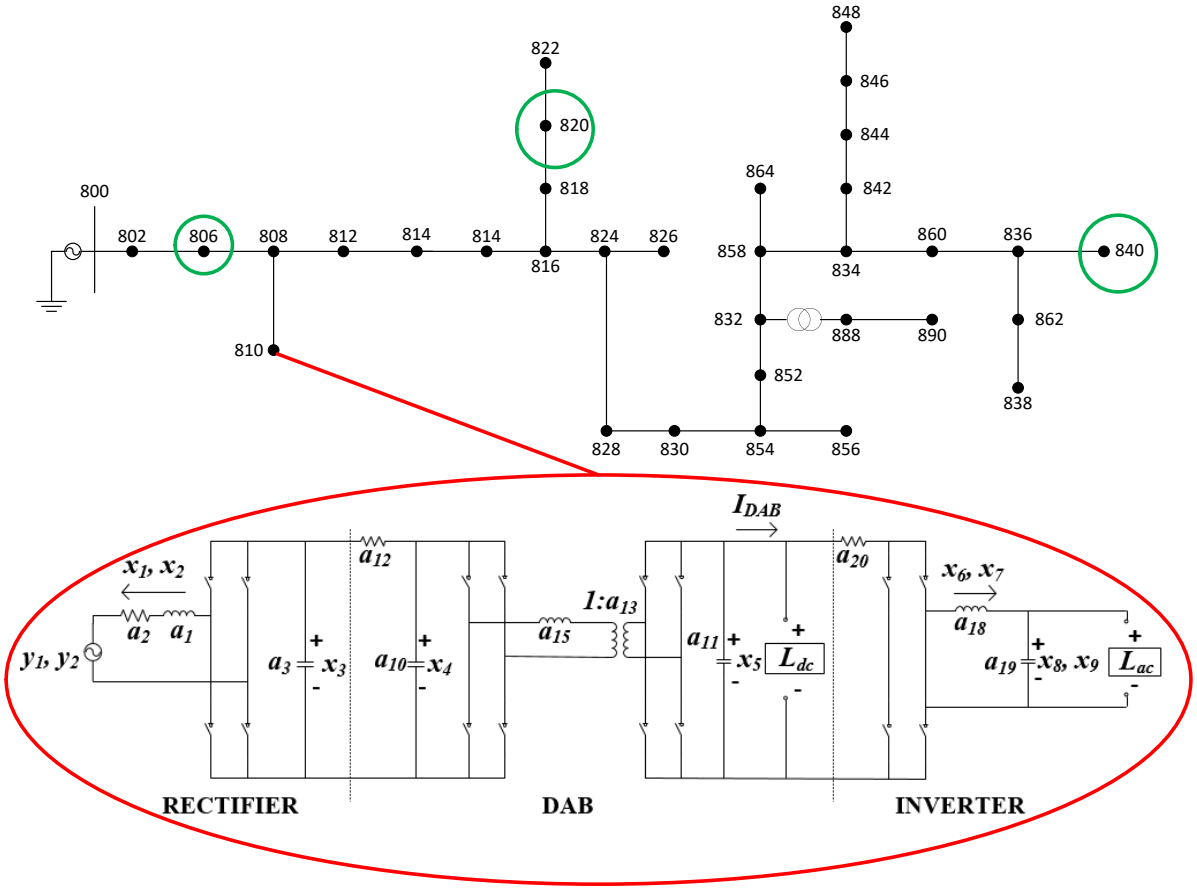

Figure 5.2: PSCAD schematic model for the IEEE 34 bus with SSTs.

Fig. 5.4 presents the simulation analysis results for the nearest (806), middle (820) and farthest (840) feeders from the point of common coupling (PCC) in Fig. 5.2. SST input voltage (*d*-axis) and rectifier output voltages of the three feeders are shown in Figures 5.4 and 5.5 as representative system variables. The rectifier output voltage in feeder 806 is being regulated at its desired value of 6100 V; the small variations are due to the changes of DRER and DESD currents into the system. The rectifier output voltage for the mid-network feeder 820 shows higher levels of dynamic variations due to the current changes in the DRERs and DESDs.

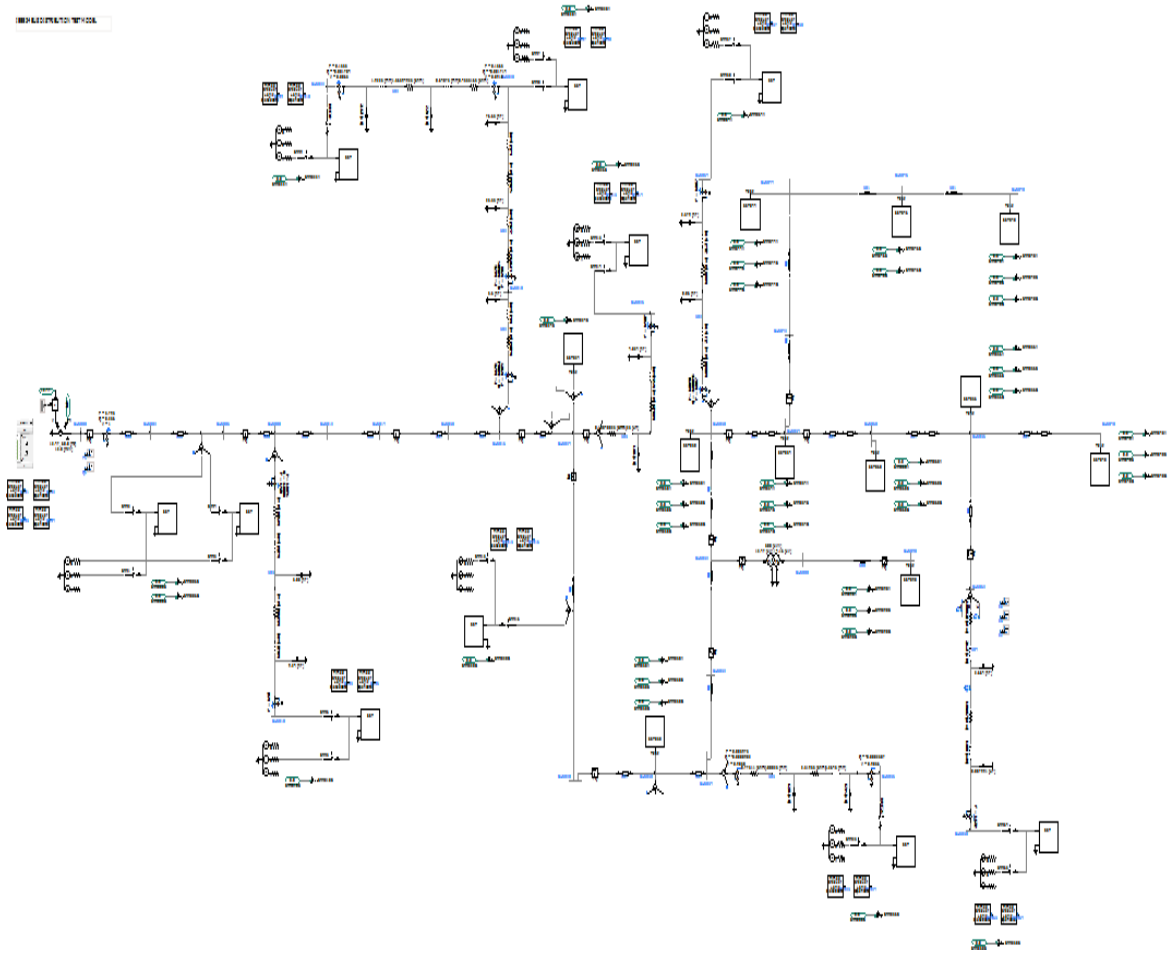

Figure 5.3: Screenshot of the LSSS model in PSCAD.

Although the rectifier input voltage decreases, the net load for the SST at node 820 is still within the feasibility bound, and hence, it does not fail. The results for the farthest feeder 840 shows that the input voltage keeps decreasing, and at t = 2.5 sec, the operation fails when the voltage reaches a level that is lower than that required to maintain feasible operation. The failure at feeder 840 is due to the violation of feasibility constraint as the net load in the system (~20 kW/ 50 amps) is more than the system can handle (~10.2 kW/ 25.5 amps) with the reduced input voltage. The results show that the feeder which is farthest from the grid suffers from infeasibility due to voltage loss in the feeder network. As the voltage level decreases at distant nodes, the maximum current that can be drawn by the DAB stage

exceeds the limits forcing the SST to enter an infeasible operating region. To study the effect of parameter values on system feasibility, the rectifier filter resistance has been reduced by one-third to increase the feasibility range (~30 kW/ 80 amps) with the same voltage level. Fig. 5.6 (a) shows the results for the DAB voltage before the resistance is changed which fails to maintain the desired set point of 400 V. Fig. 5.6 (b) and Fig. 5.6 (c) show that the rectifier and DAB output voltages with changed resistance value are regulated and the system is within the feasibility range with node voltage as in Fig. 5.5 (c) and similar net load. The controller gains need to be further tuned to reduce the dynamic variations seen in the output voltages.

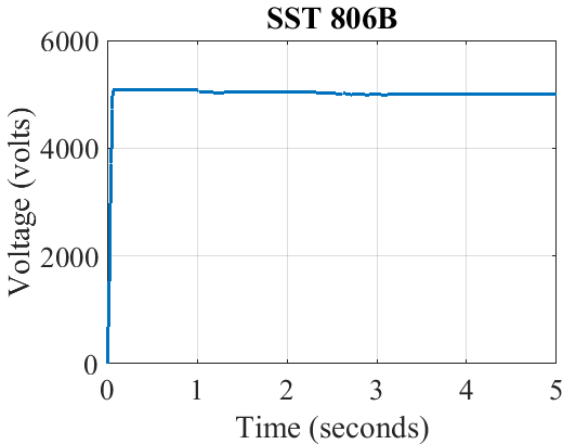

(a) Feeder 806 input voltage (*d*-axis)

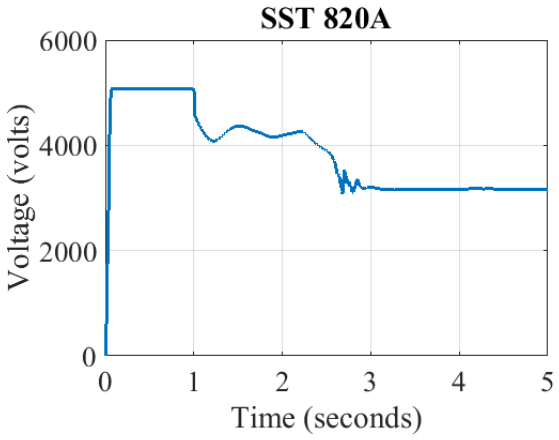

(b) Feeder 820 input voltage (*d*-axis)

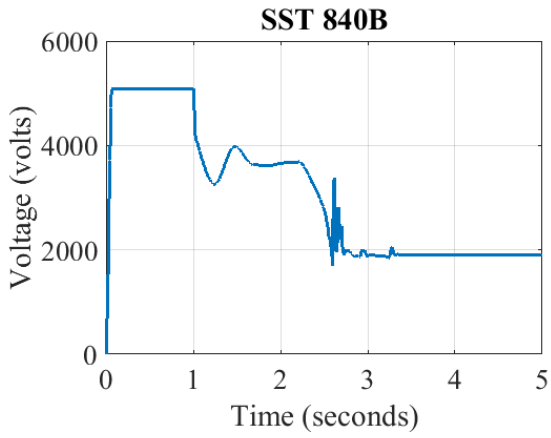

(c) Feeder 840 input voltage (*d*-axis)

Figure 5.4: SST input voltage (*d*-axis) in IEEE 34 bus simulation.

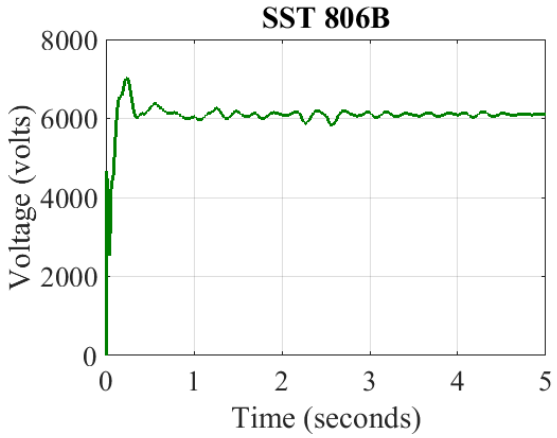

(a) Feeder 806 rectifier output voltage

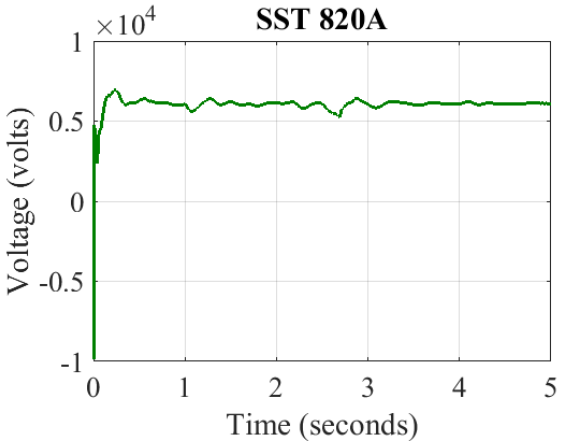

(b) Feeder 820 rectifier output voltage

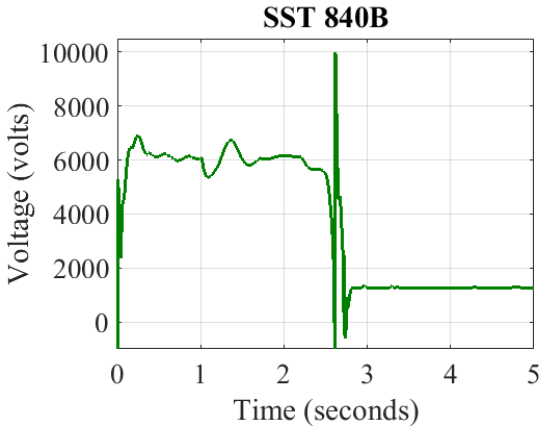

(c) Feeder 840 rectifier output voltage

Figure 5.5: Rectifier output voltage in IEEE 34 bus simulation.

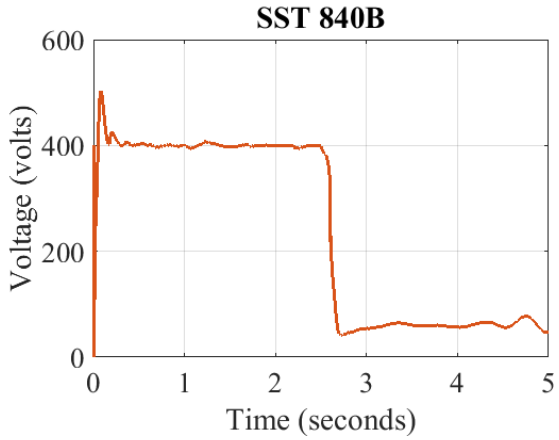

(a) Feeder 840 DAB output voltage before change in resistance

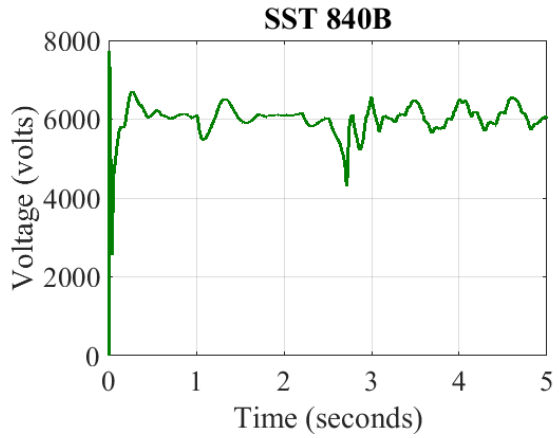

(b) Feeder 840 rectifier output voltage after change in resistance

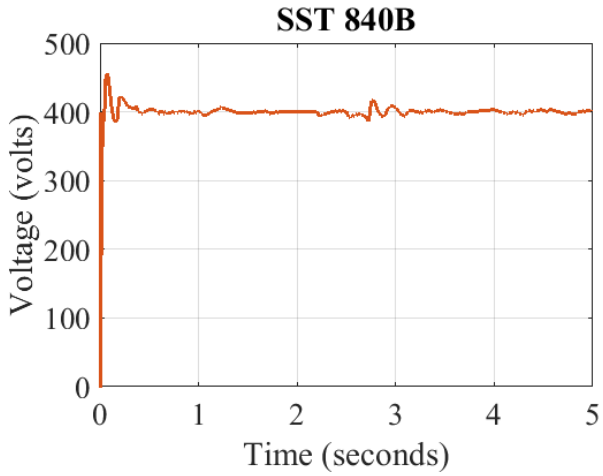

(c) Feeder 840 DAB output voltage after change in resistance

Figure 5.6: Failure analysis for distant SST in IEEE 34 bus.

The key parameters affecting the feasibility range of a multi-SST power distribution system can be obtained with the presented models and analysis. The results from the nonlinear simulation model correlate well with the results seen earlier in the surface plots in chapter two. The parameters can be tuned appropriately in the design stage to enhance the feasibility region, and also to determine the operation bounds required for controller design. A similar approach for design and analysis can be used for any physical hardware used in traditional microgrid. The operation bounds provide the critical information on when system will fail due to feasibility violation rather than because of a controller instability issue.

5.4. Implementation of Power Sharing Methods in IEEE 34 Bus System

In this simulation, power sharing is validated with method one and method two. The implementation diagram for both the methods are shown in Figures 4.6 and 4.7. The modified IEEE 34 bus (9 SSTs) model parameters are same as the parameters in Table 3.1.

5.4.1. Storage Controller with Method 1

In this subsection, developed energy storage controller is used to validate the power sharing method one where input current remains same for all the neighboring SSTs except i^{th} SST. To validate the controller actuation, a sudden change in the net power happens at t = 0.6 sec in SST 5 as the storage capacity is full to absorb more power. Storage currents are plotted in Figures 5.7 to 5.9 for all 9 SSTs due to the change in power of SST 5.

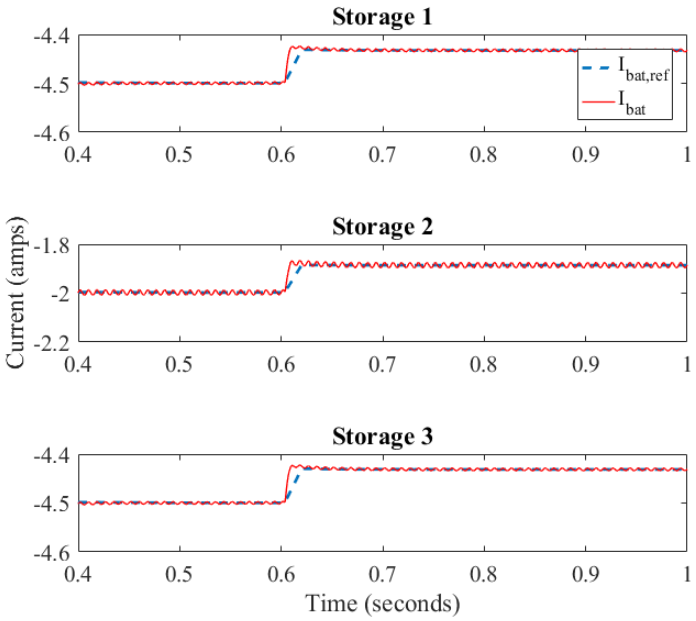

Figure 5.7: Storage response of SST 1 to 3.

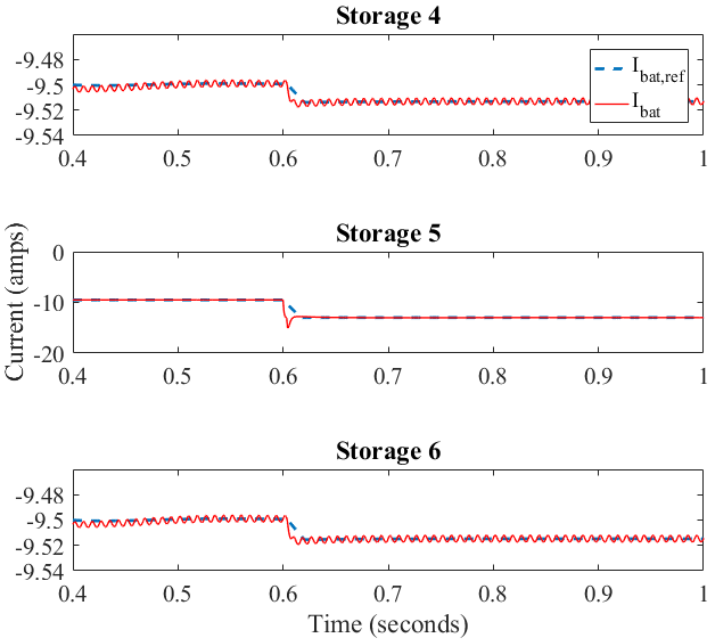

Figure 5.8: Storage response of SST 4 to 6.

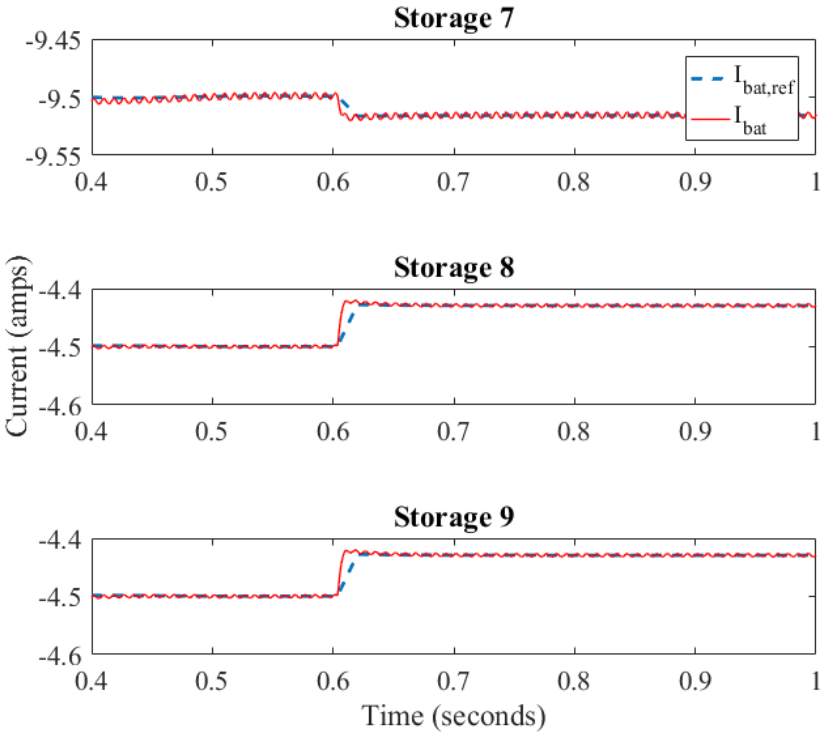

Figure 5.9: Storage response of SST 7 to 9.

For this case study, the wind and PV currents are kept constant for all the SSTs and I_{bat}^{r} of every SST are flat lines as there was no variation in the load demand or renewable generation before t = 0.6 second, and then due to change in power in SST 5, I_{bat}^{r} gets updated for all the SSTs and actual I_{bat} follows. The convergence times of the regulation is around 5 ms, also each SST-storage are capable of supporting the change as shown in Figures 5.7 to 5.9. The ripples present in the response of I_{bat} is due to the second harmonics of the DC bus voltage. Updated P_{rec} for all the SSTs are also shown in Figures 5.10 to 5.12 where the red dotted line represents the reference and green one indicate the real $P_{rec}(t)$. The ripples in $P_{rec}(t)$ are due to the second order harmonics of fundamental frequency component of the grid side as shown in equations (2.3). Based on the change in net power, corresponding storage of the SSTs reference are being updated as shown in Figures 5.7 to 5.9. $P_{rec}(t)$ of the SST 5 shows

transient response when the big load change happens as the SST is not capable of compensating the change and settles to the required power set point as soon as power sharing method provides the new power setpoint for all other 8 SSTs in the network. As shown in the figure, update of setpoint can be calculated in one time step of the storage control (in μ seconds) and the system is guaranteed to maintain the feasibility without compromising the grid stability.

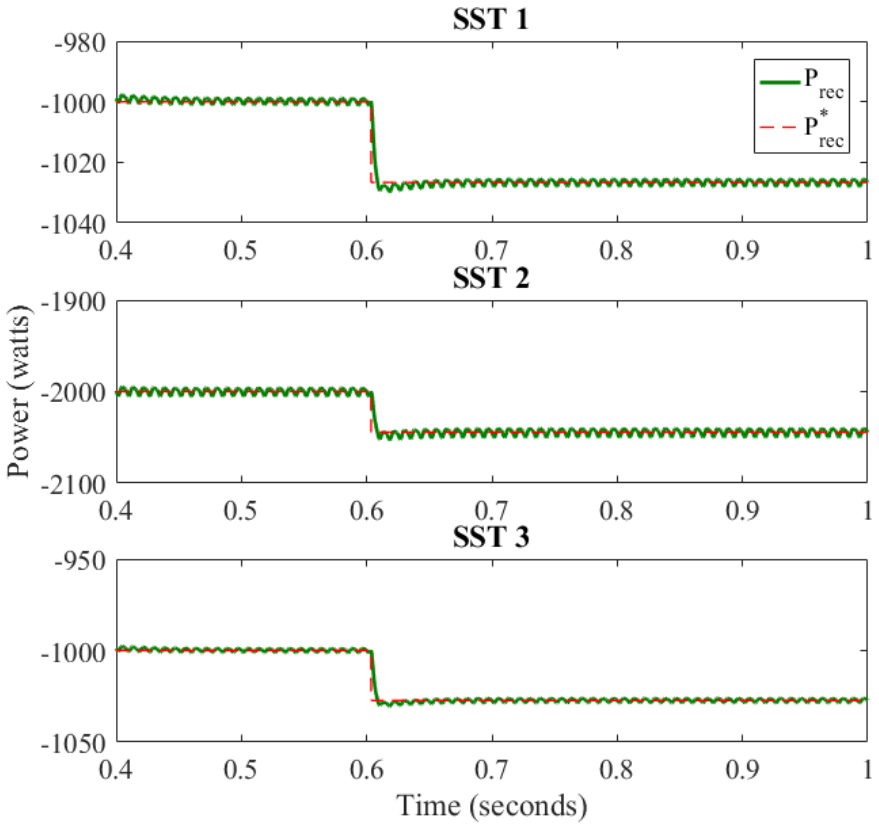

Figure 5.10: Power profile of SST 1 to 3.

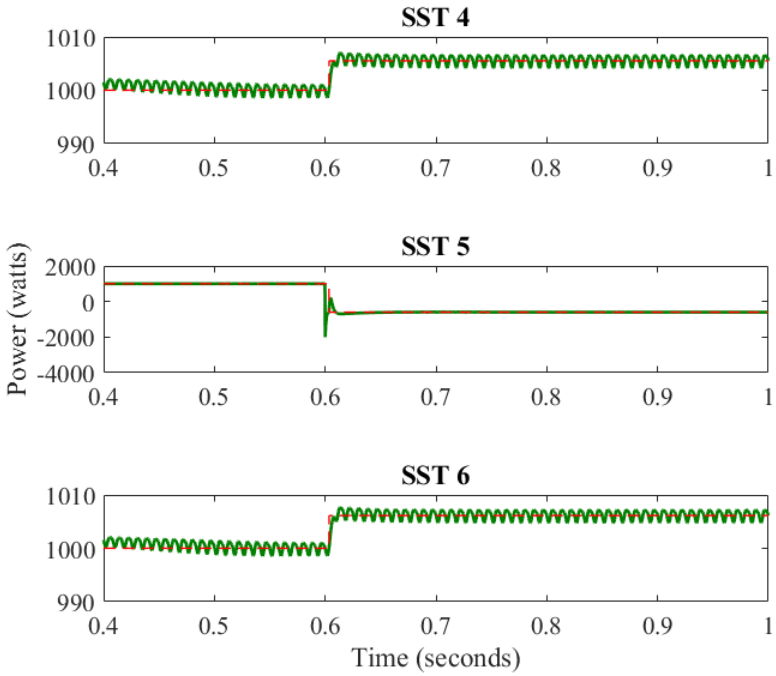

Figure 5.11: Power profile of SST 4 to 6.

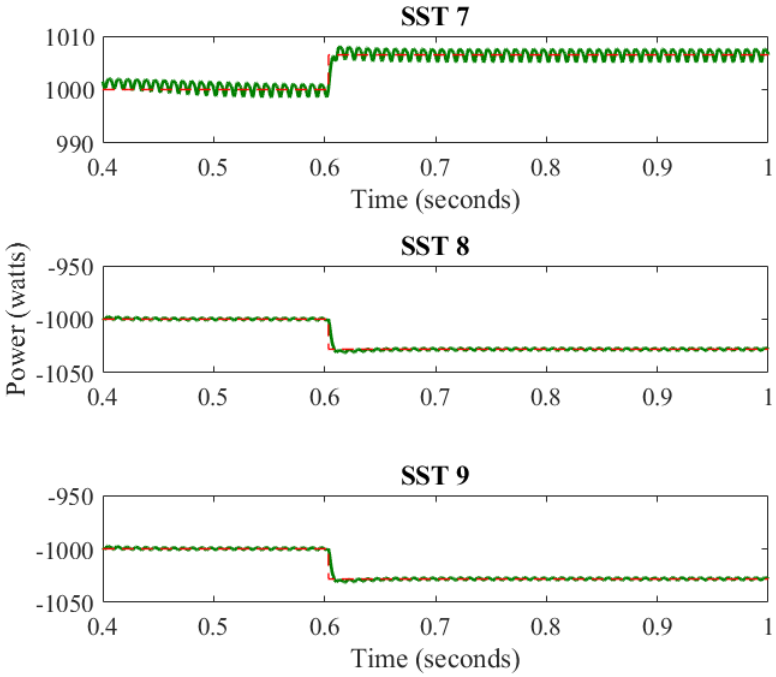

Figure 5.12: Power profile of SST 7 to 9.

Results are also provided in Figures 5.13 and 5.14 to show the state response of the SST during the power setpoint update due to the power sharing. DAB output voltage for the SST 4 to 6 are shown in the Fig. 5.13 where the SST 5 shows a transient value of 2.5% due to change in power, however, the DAB output voltage of other SSTs don't see any significant transient disturbance as the new setpoint calculation is done with one step of the storage controller. Similar responses have been observed for other SSTs in the system, however, those are not provided to avoid repetition.

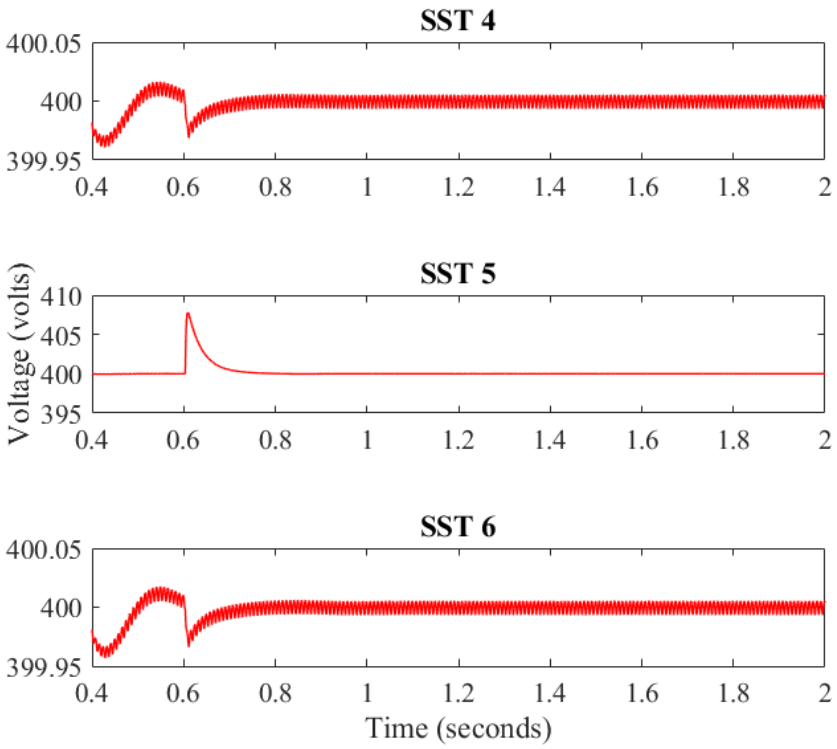

Figure 5.13: DAB output voltage of SST 4 to 6.

Rectifier output voltage response is also provided besides the DAB voltage due to the power sharing in Fig. 5.14. Rectifier output voltage for the SST 7 to 9 are shown in the Fig. 5.14 where all the SSTs show that the steady-state regulation is well maintained to the desired output voltage of 6100 volts. Again, the oscillations in the response are due to the second

order harmonics of the fundamental grid frequency which captures the AC side variation. Rectifier output voltage except SST 5 show the similar response as in Fig. 14 and so those are not provided.

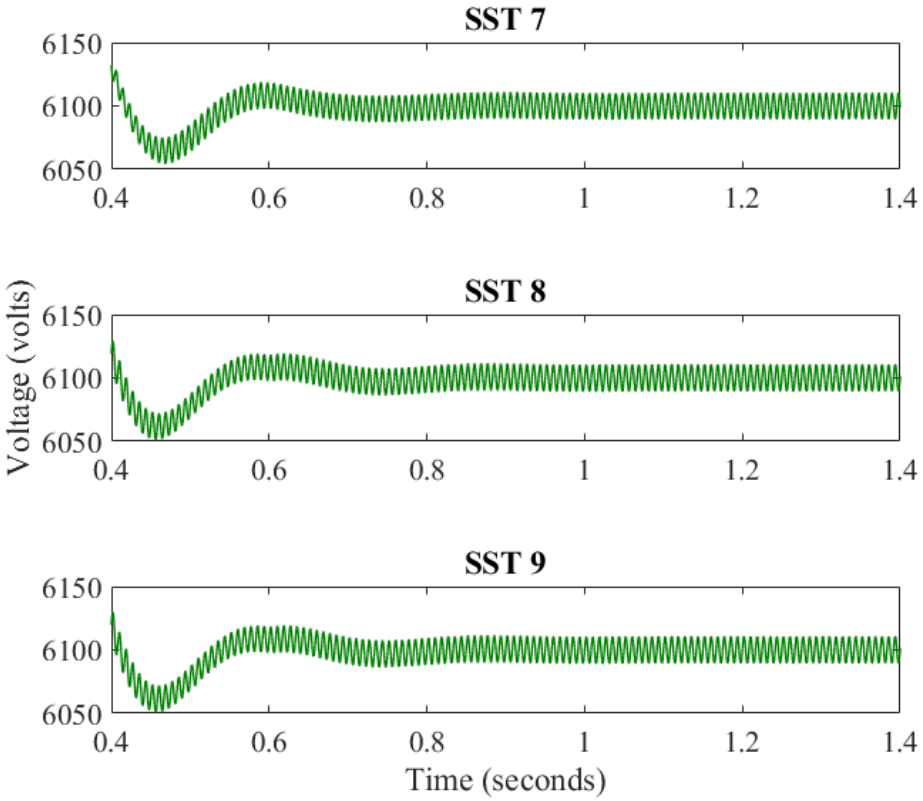

Figure 5.14: Rectifier output voltage of SST 7 to 9.

As it shows that the setpoint calculation for power sharing is instantaneous, and hence the control is actuated immediately after the load changes. As a next step, a scenario in which the operation points are not updated immediately is simulated after the change in load happens in SST 5. This is intended to emulate a realistic scenario in which a computational delay is present while calculating the new setpoints. The results for the storage response are shown in Figures 5.15 to 5.17. As it is observed, the impact of waiting for the new set points are visible through the oscillations in I_{bat}^{r} and subsequently in storage response actual I_{bat}. These results

highlight the importance of the communication network and data transfer in SST based MG network as accurate I_{bat}^{r} cannot be calculated if there is any kind of delay present in the system. Power profiles for the SSTs with a delay in setpoint calculation are provided in Figures 5.18 to 5.20. As expected, P_{rec}^{*} fluctuates to settle to the desired new setpoint with a delay and power profile also follows that to maintain the power balance of the system, which is a must for every instant of time. As soon as the reference is set to the correct point, the system response is flat line with regular second order harmonics. This delay also affects the steady-state regulation of the SSTs as shown in Figures 5.21 and 5.22. Plots are provided for DAB output voltage in Fig. 5.21 for the same SSTs as in Fig. 5.13 and it can be observed that unlike Fig. 5.13, the regulation of SST 4 and 6 also get affected due to the delay in setpoint calculation. Similar observation is found in Fig. 5.22.

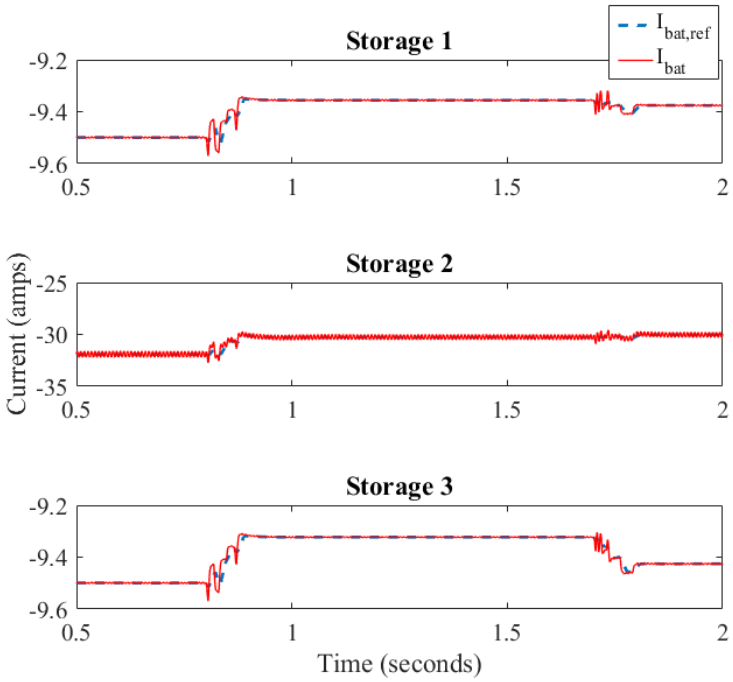

Figure 5.15: Storage response of SST 1 to 3.

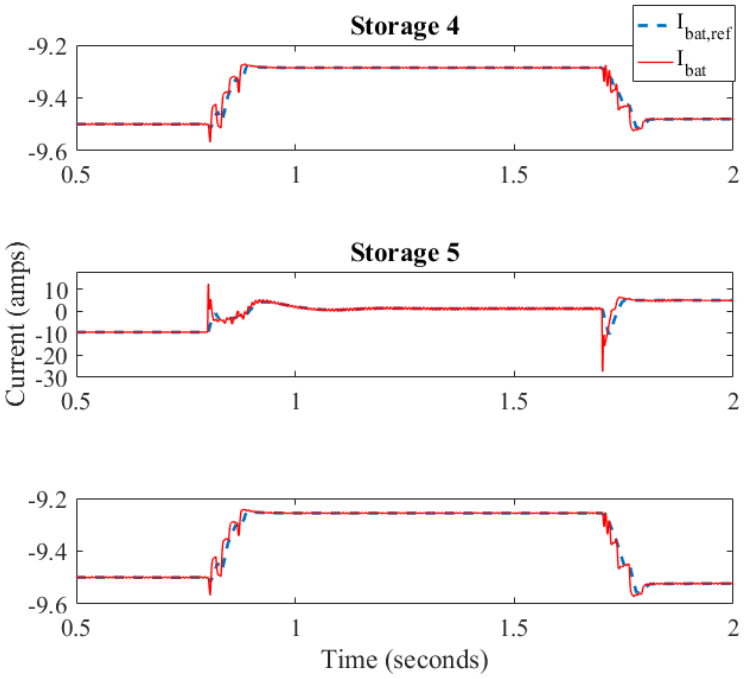

Figure 5.16: Storage response of SST 4 to 6.

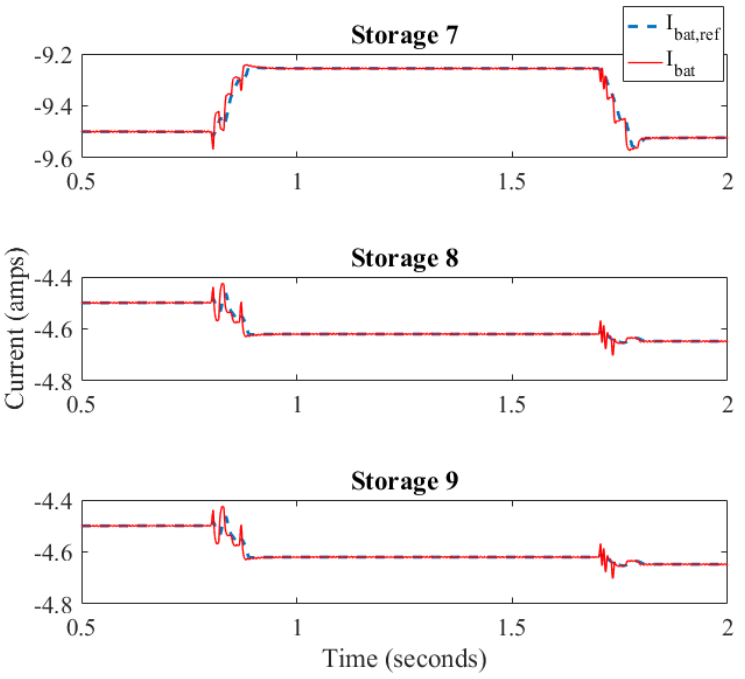

Figure 5.17: Storage response of SST 7 to 9.

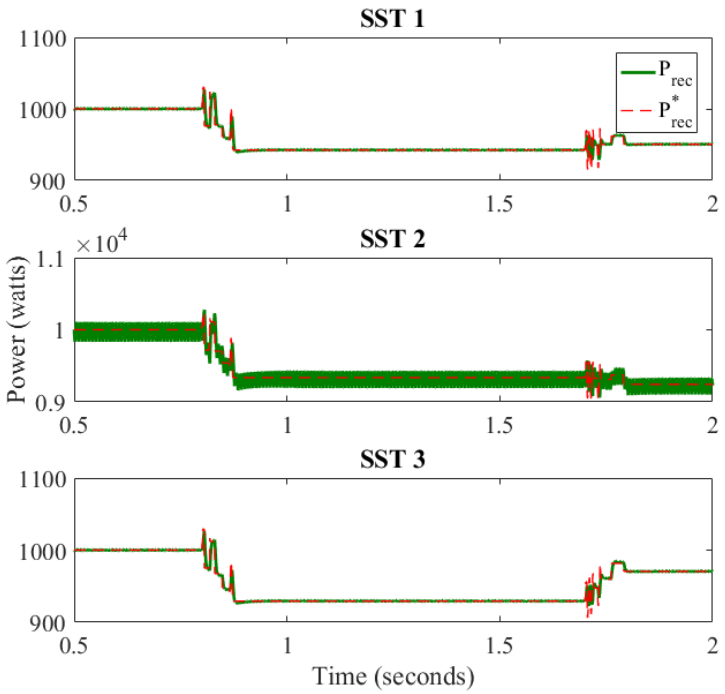

Figure 5.18: Power profile of SST 1 to 3.

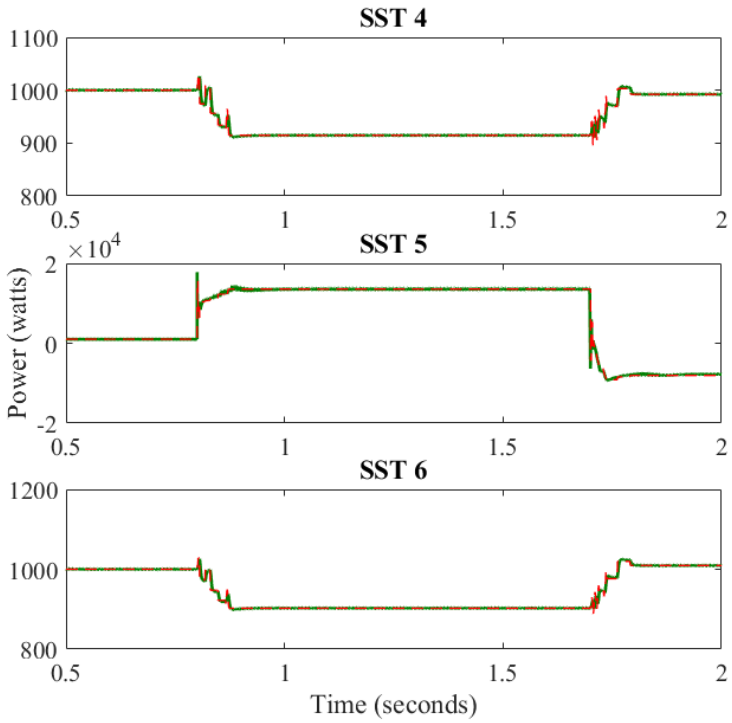

Figure 5.19: Power profile of SST 4 to 6.

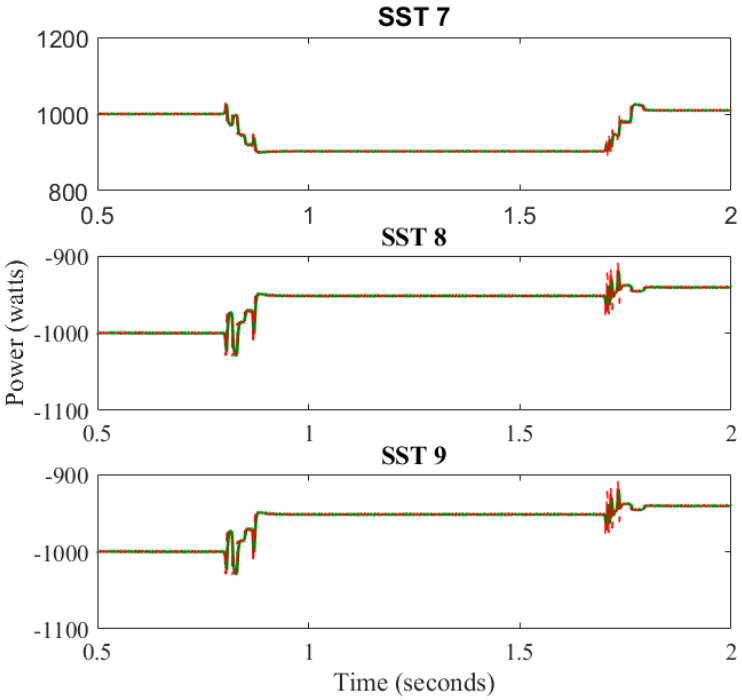

Figure 5.20: Power profile of SST 7 to 9.

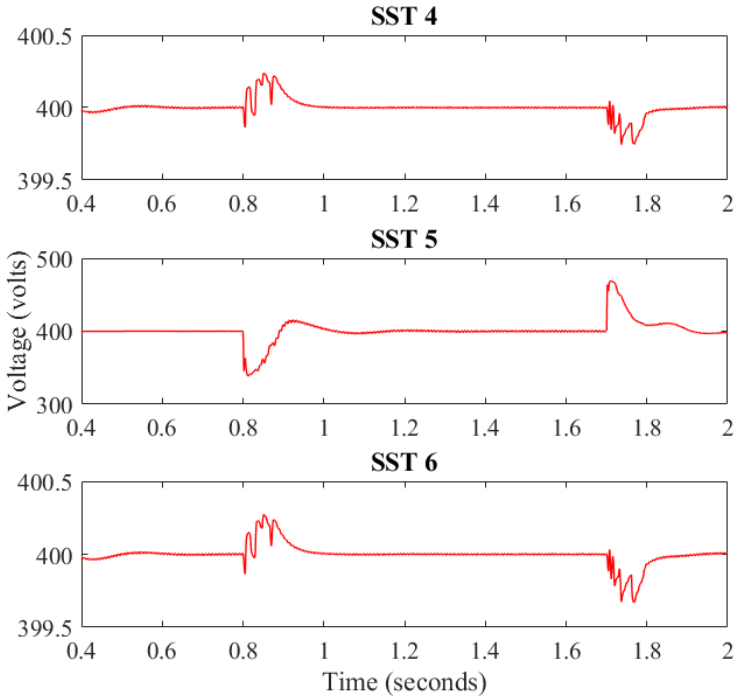

Figure 5.21: DAB output voltage of SST 4 to 6.

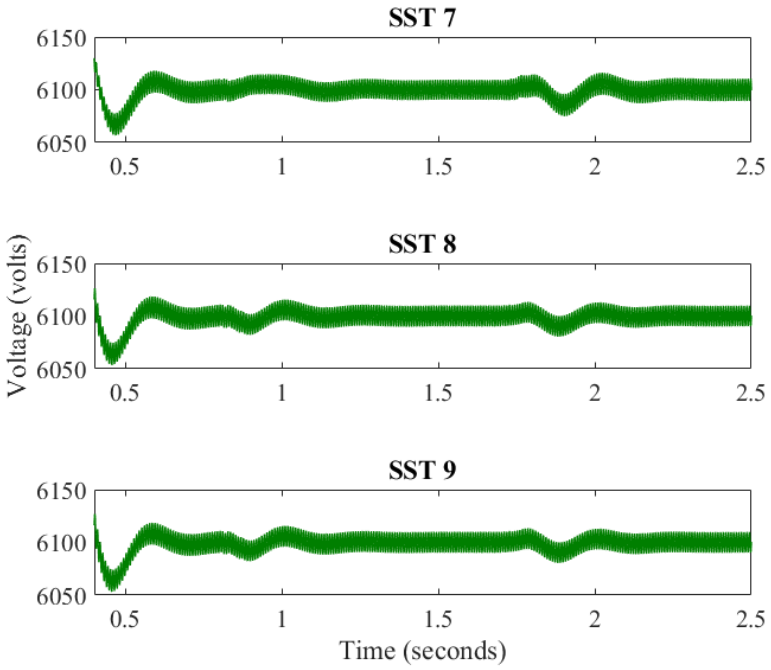

Figure 5.22: Rectifier output voltage of SST 7 to 9.

5.4.2. Storage Controller with Method 2

In this subsection, developed energy storage controller is used to validate the power sharing method two where node voltage remains same for all the neighboring SSTs except i^{th} SST. To validate the controller actuation, a sudden change in the net power happens at t = 0.6 sec in SST 5 as the storage capacity is full to absorb more power. Storage currents are plotted in Figures 5.23 to 5.25 for all 9 SSTs due to the change in power of SST 5. For this case study, the wind and PV currents are kept constant for all the SSTs and I_{bat}^{r} of every SST are flat lines as there was no variation in the load demand or renewable generation before t = 0.6 second, and then due to change in power in SST 5, I_{bat}^{r} gets updated for only the neighboring SSTs unlike method one and actual I_{bat} follows.

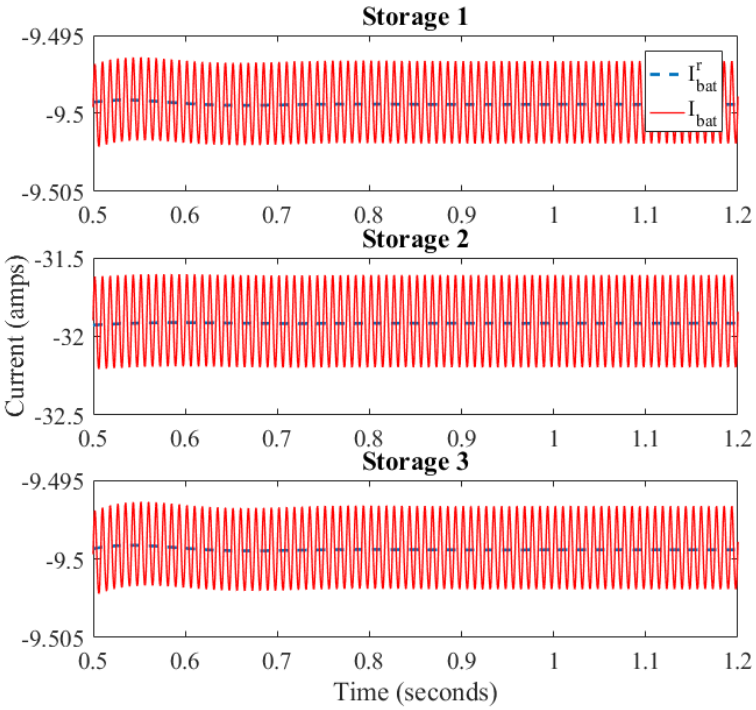

Figure 5.23: Storage response of SST 1 to 3.

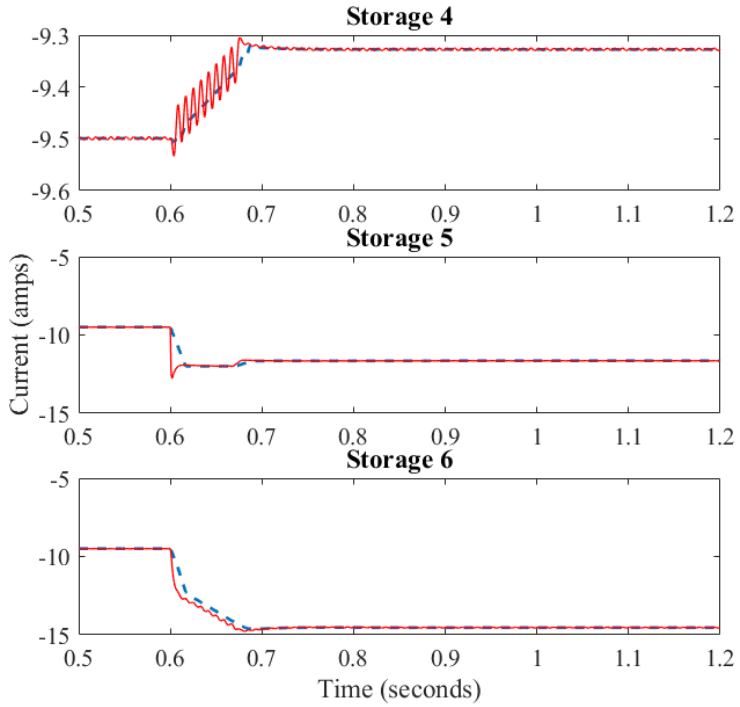

Figure 5.24: Storage response of SST 4 to 6.

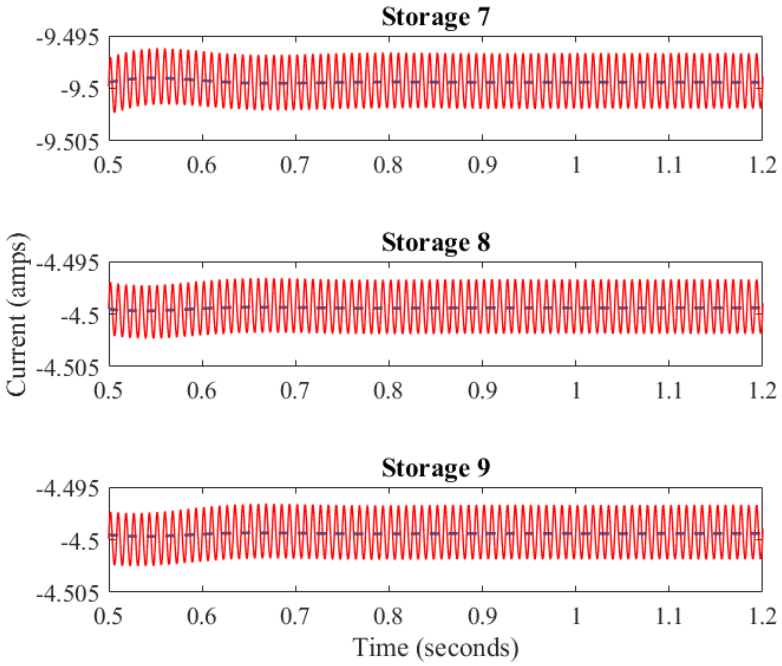

Figure 5.25: Storage response of SST 7 to 9.

As explained in chapter three, method two only involves the immediate neighbor for power sharing and all others in the network have uninterrupted operation. As shown in Figures 5.23 and 5.25, I_{bat}^{r} remains the flat for the SST 1 to 3 and 7 to 9 as only the immediate neighbors of the SST 5 are SST 4 and SST 6. The change in the storage current reference for SST 4 and 6 are shown in Fig. 5.24. For this method, the computation delay is unavoidable due to calculation of the impedance ratio in complex plane. However, the accurate setpoint can be calculated in less than 0.1 second and the oscillations due to the wrong operational point is shown in Fig. 5.24. The ripples (~0.01%) present in the response of I_{bat} is due to the second harmonics of the DC bus voltage similar to method one. Updated P_{rec} for all the SSTs are also shown in Figures 5.26 to 5.28 where the red dotted line represents the reference and green one indicate the real $P_{rec}(t)$. The ripples in $P_{rec}(t)$ are due to the second order harmonics of fundamental frequency component of the grid side as shown in equations (2.3)

and as expected, no change in power is observed in Figures 5.26 and 5.28. Based on the change in net power of the immediate neighbors (SST 4 and 6), corresponding storage current reference are being updated as shown in Fig. 5.24. $P_{rec}(t)$ of the SST 5 shows transient response when the big load change happens as the SST is not capable of compensating the change and settles to the required power set point as soon as power sharing method provides the accurate setpoints for the neighbors.

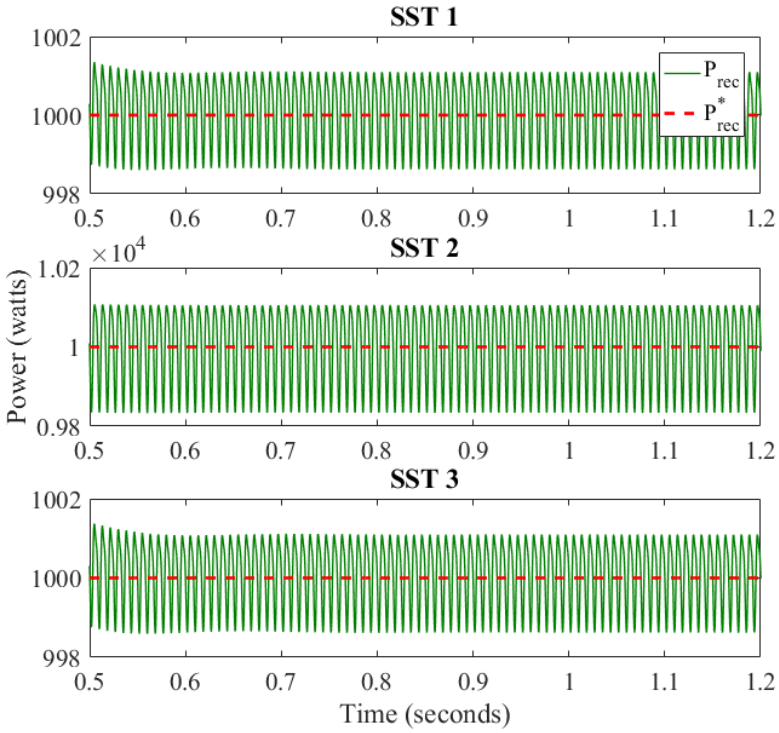

Figure 5.26: Power profile of SST 1 to 3.

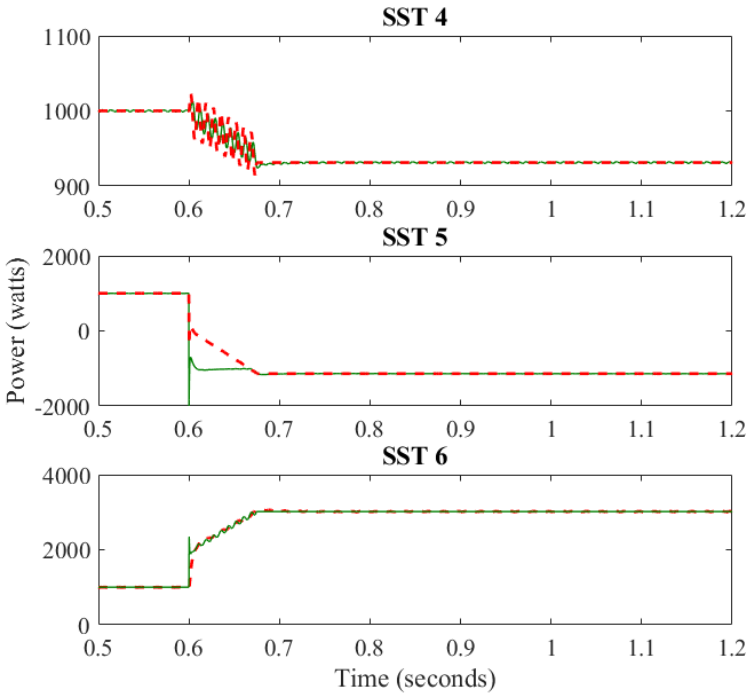

Figure 5.27: Power profile of SST 4 to 6.

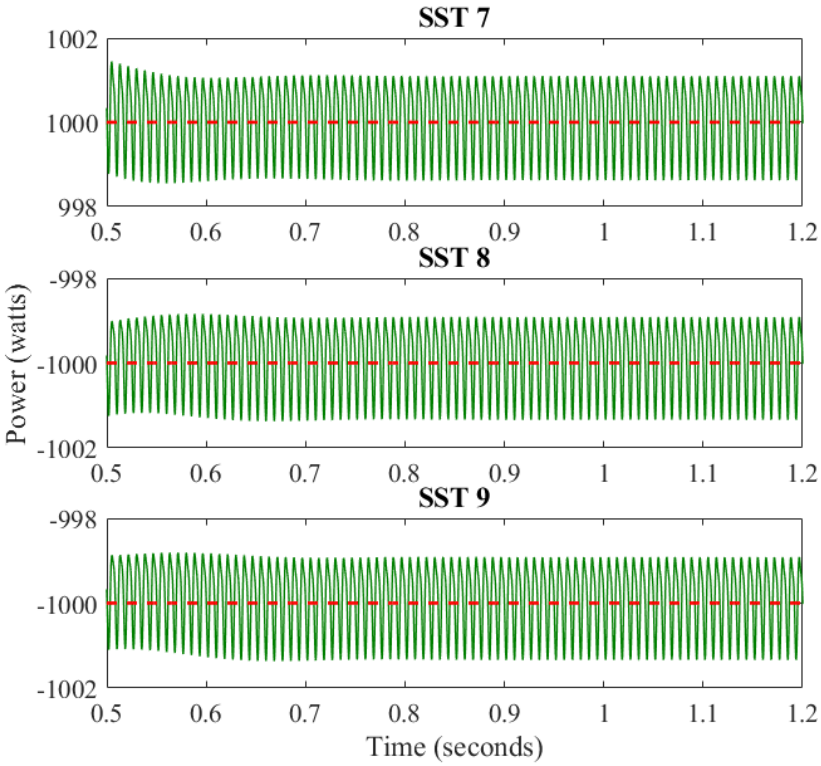

Figure 5.28: Power profile of SST 7 to 9.

An interesting observation is also made in between method one and two in terms of the impact for the grid side. As in method one, all the neighbors share the change and the rest is being taken care by the grid and so the *d*-axis current of the grid gets changed in method one as shown in Fig. 5.29. However, for the similar change in power in SST 5 with method two, there is no impact on the grid side as the immediate neighbors compensate fully for any changes in the system. This advantage makes method two more applicable to maintain the grid stability and uninterrupted operation, however, it comes with disadvantage of burdening the neighbors heavily in the process and also has a computational delay of around 0.08 second.

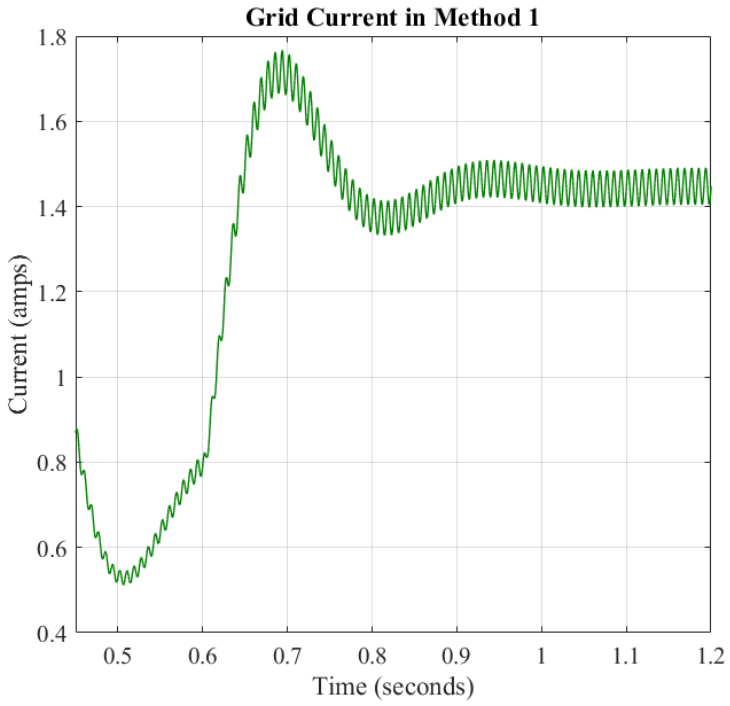

Figure 5.29: Grid current in method one.

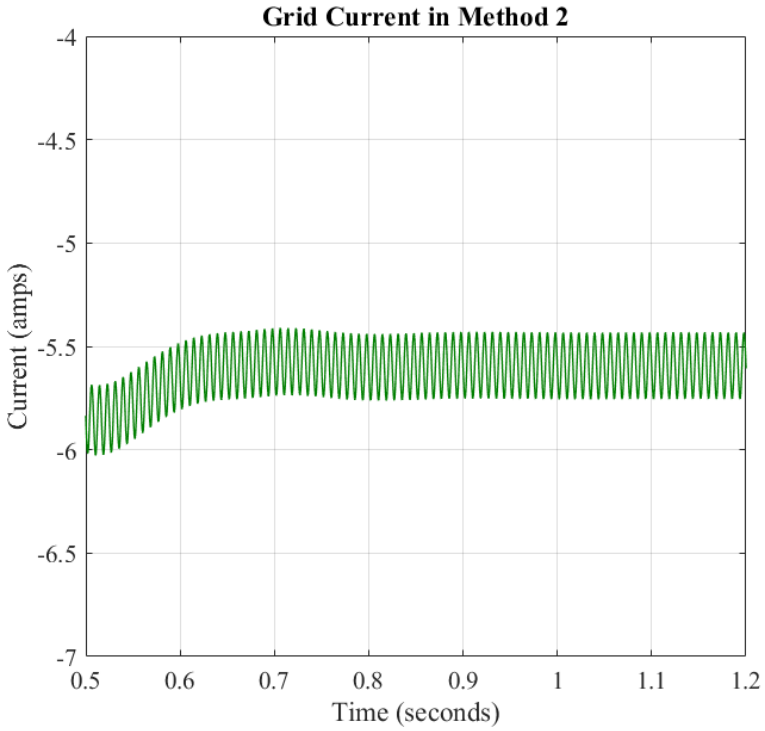

Figure 5.30: Grid current in method two.

Results are also provided in Figures 5.31 to 5.33 to show the state response of the SSTs during the power setpoint update in power sharing method two. DAB output voltage for the SST 1 to 3 and 7 to 9 don't see any change as those are not immediate neighbors of SST 5 as shown in the Fig. 5.31 and 5.33. However, due to computational delay, SST 4 to 6 show a transient value of 1% to 2.5% in between the calculation of accurate operational point. Similar responses have been observed for rectifier output voltage in Figures 5.34 to 5.36 with very similar response of DAB output voltage. Again, the oscillations in the response are due to the second order harmonics of the fundamental grid frequency which captures the grid frequency.

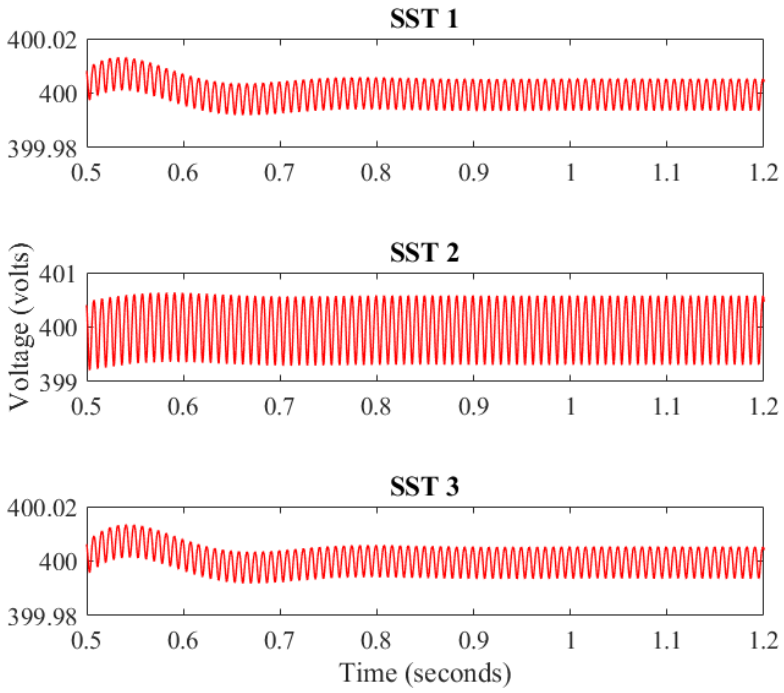

Figure 5.31: DAB output voltage of SST 1 to 3.

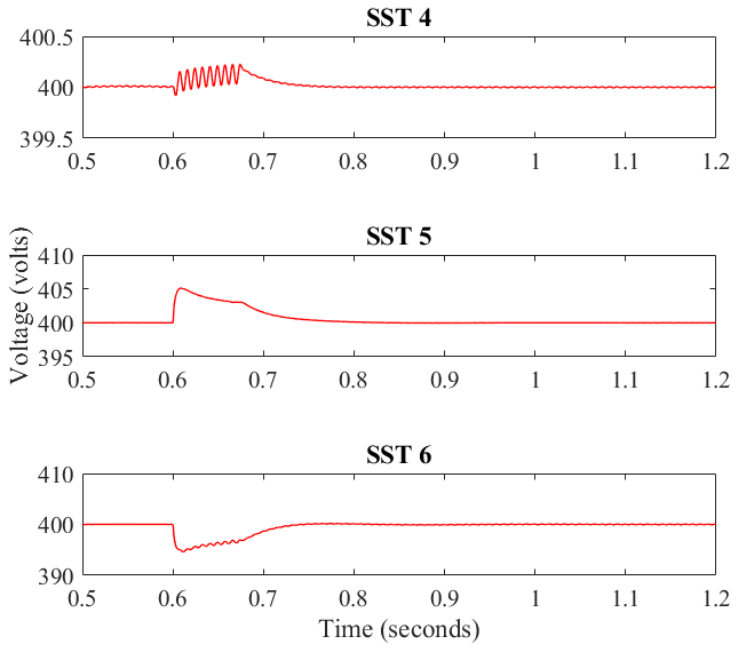

Figure 5.32: DAB output voltage of SST 4 to 6.

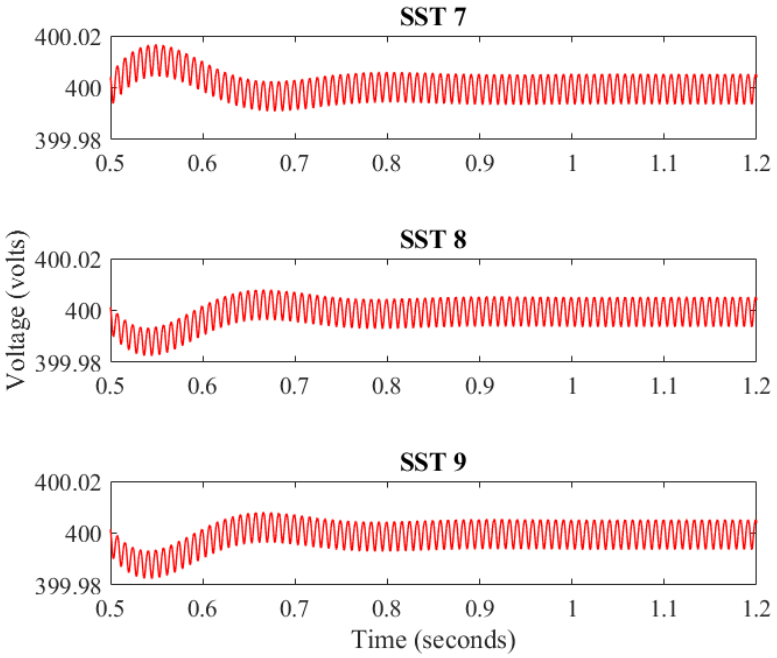

Figure 5.33: DAB output voltage of SST 7 to 9.

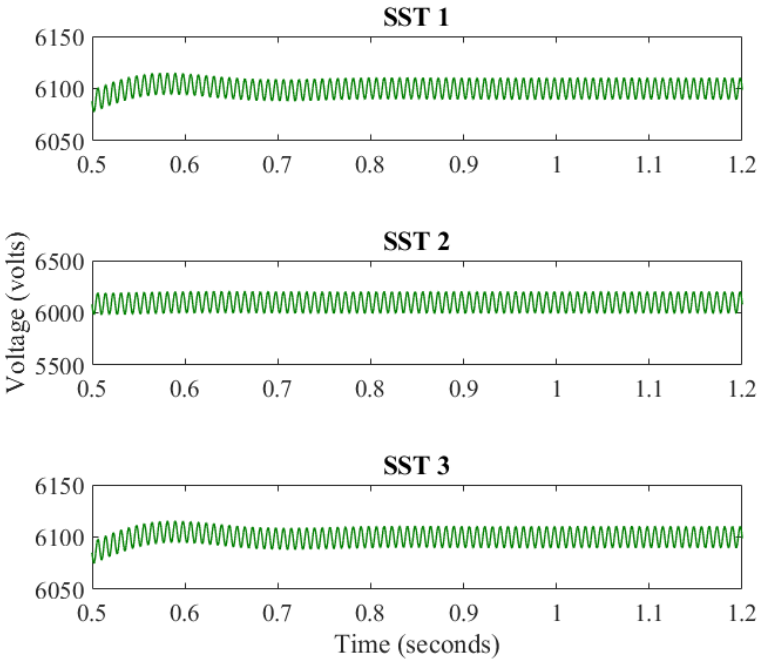

Figure 5.34: Rectifier output voltage of SST 1 to 3.

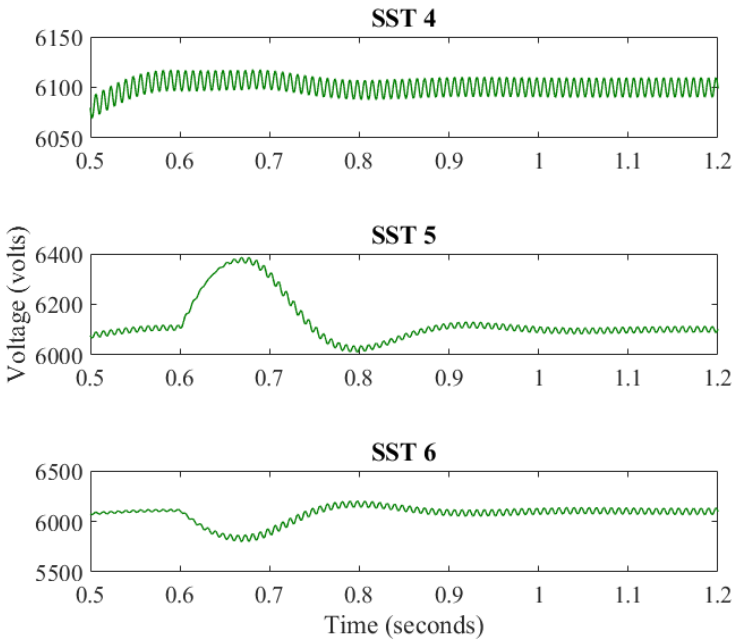

Figure 5.35: Rectifier output voltage of SST 4 to 6.

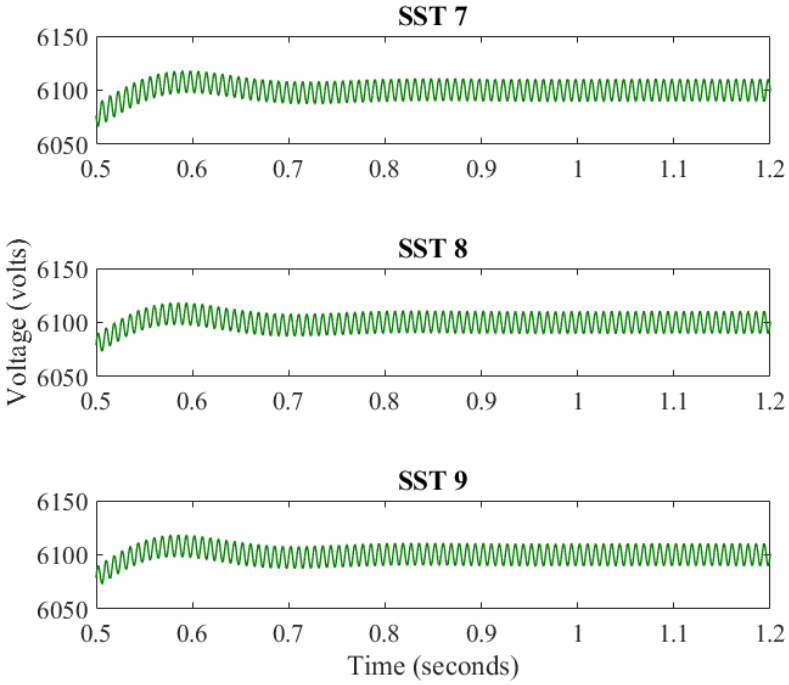

Figure 5.36: Rectifier output voltage of SST 7 to 9.

5.5. Contribution

1. Full SST system is built in the PSCAD to validate the developed model in the distribution network of IEEE 34 bus. The model follows the feasibility bounds those were derived from the simplified model and also provides the reasoning behind system failure in a large distribution network.

2. Power sharing methods are validated with developed storage controller in the modified IEEE 34 bus with 9 SSTs. Results show that the computational time can play significant role in execution of these methods as the regulation of the SST states rely on accurate operation setpoint.

3. Location can also play a significant role in method two where the power sharing depends on immediate neighbors and the power ratio is a function of the tie line impedance.

5.6. Conclusions

Fundamental physical model, feasibility criteria, power sharing methods and energy storage controller developed in earlier chapters are verified in a large system simulation in this chapter. It is critical to provide the proof of concept for the dynamic physical models in a practical system like IEEE 34 bus which will eventually lead towards real-time hardware implementation. More importantly, the feasibility criteria were developed for a simplified rectifier model which is verified for a full microgrid system in this chapter. Maintaining the feasibility criteria is difficult once the hardware is built and so the developed power sharing methods will be important for a feasible operation when anyone in the network violates the conditions or require sudden high amount of power. Implementation of such power sharing requires the support of the energy storage and this chapter validates power sharing methods

with energy storage controller. This work can eventually be considered for developing a virtual power network in a community microgrid system.

CHAPTER 6

‘PLUG-AND-PLAY’ PV INSTALLATION FOR DC-AC ENERGY CELLS WITH EXPEDITED PERMITTING DEVICE

6.1. Introduction

6.2. Current PV system permitting requirements

6.3. ‘Plug-and-Play’ PV Electrical System

6.4. Multi-port Building Block (MPBB)

6.5. Photovoltaic Utility Interface (PUI)

6.6. PUI Start up and System Authentication

6.7. Prototype and Experimental Results

6.8. Cost analysis of the System

6.9. Contribution

6.10. Conclusions

6.1. Introduction

PV system is an essential component of the FREEDM system based MG and this work is based on the automation of the PV system installation for residential houses to facilitate the SST operation. As the previous chapter works with the storage control for FREEDM system, it is also critical to have system level development for expedited PV installation to get the full advantages of SST based network. PV integration and its role in SST based MG is shown in Fig. 6.1 [79].

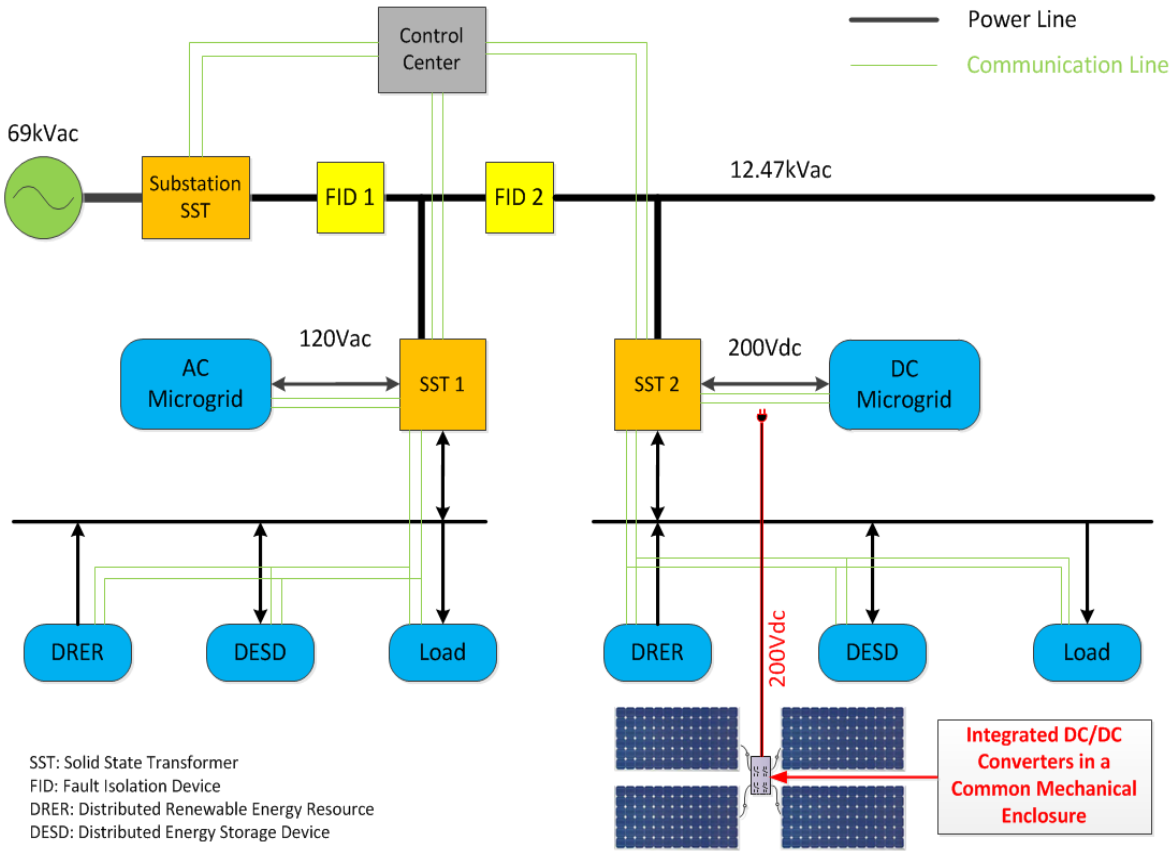

Figure 6.1. PV system in SST based network [79].

With sharp increase in the adoption of residential PV systems, new technologies and streamlined procedures are being created to make the installation process faster, cheaper, and

easier for the system owner. Recent solar industry data shows that utility PV systems have been reduced in cost by nearly 50% since 2011 whereas residential PV systems have reduced by 30% in the same time period that helped PV installations to increase by more than 50% [80]. Overall system cost for the PV system can be categorized into hardware cost and soft cost. The hardware cost comprises of modules, inverters, racking, and all other hardware required for the installation of a PV system. Installation labor, customer acquisition, permitting, inspection, interconnection, overhead and profit margin are categorized as the soft cost for PV system price. Soft cost itself is accountable for 44% of the system price in residential PV system, according to the recent National Renewable Energy Laboratory (NREL) benchmark cost breakdown for residential systems [81]. Eventually, soft costs and labor intensive PV installations are still preventing residential PV system from being widely adopted. The Solar Electric Power Association (SEPA) and the Electric Power Research Institute (EPRI) recently reported on the advantages of utility-owned inverters [82]. Advantages of utility-owned inverters are many and include utility controlled on-grid conditions, reduction of PV system price through utility ownership, easier maintenance and upgrading, and real-time data transfer that enables proactive grid support. Local governments across the US have already introduced streamlined and less invasive installation and permitting processes [83, 84]. These solutions involve the physical installation of the PV system, and quick permitting and interconnection agreement with the utilities by the Authorities Having Jurisdictions (AHJs). Generally, AHJs have the authority to inspect the system to ensure it meet the technical requirements, i.e., the National Electric Code (NEC). They also have the freedom to interpret the code and waive requirements for alternative methods (equipment and practice); some of the state authorities have started to introduce

those alternate ways to expedite the permitting process. San Diego Gas and Electric has been able to efficiently streamline its interconnection application process by launching its Distributed Interconnection Interface System (DIIS) [85]. The DIIS has been able to increase the average authorized application per employee from 30 applications a day in late 2012 to as high as 196 applications a day currently. This system is unique, because it allows for a much smoother interface and communication between local AHJ inspectors, the utility, and the end-user. In lieu of physical paperwork, the entire installation process is streamlined using digital communications. However, none of these practices really provided the solution that will significantly reduce the installation cost, which is the other major contributor of the PV system soft costs. The PnP concept recently proposed by North Carolina State University (NCSU) researchers not only incorporates the streamlined communications concept with the help of a smart interface, but also pushes the idea further to produce a truly PnP installation and interconnection process that can handle both installation and inspection related soft costs [43, 44]. Through the use of a cloud interface and system level software features, the smart interface enables the automation of PV system installation and approval. This particular research is part of the Department of Energy's (DoE) Sunshot initiative that targets an installation cost of $1.50/watt (currently, $3.09/watt [81]) for residential PV systems by 2020 which will translate to 6-8¢/kWh Levelized Cost of Energy (LCOE) assuming 20 years of PV panel lifetime with 10% discount rate [86]. LCOE range considers the variable solar generation in different geographical locations in USA. Sunshot initiative deals with the redesign of the residential PV system that will reduce the overall system price and installation time. Flexible racking system, innovative inverter solution and PUI are developed under the initiative, and this paper discusses the PUI concept that is expected to reduce the

installation and inspection cost significantly. The PUI functional prototype has been developed and tested with a focus on self-inspection, start-up algorithm, and internal communications.

6.2. Current PV system permitting requirements

The residential PV installation permitting steps can be categorized into three major aspects of electrical, structural and utility interconnection. Fig. 6.2 shows the steps currently followed to satisfy the residential PV installation requirements. Generally, the consumer contacts the vendor and the vendor completes the initial system sizing before selling their product. Later, the consumer has to schedule an appointment with a certified installer for the PV system installation. The installer follows article 690 of NEC that specifies the codes related to obtaining the electrical permit for the PV system [87]. PV rating, protection circuit, AC and DC disconnects, ground fault protection, system grounding, wiring methods, and equipment markings are the major items checked based on the article NEC 690. Besides NEC 690, the electrical components of the PV system must have UL certification according to the UL 1741 standard [88]. Building codes from International Code Council (ICC) are followed to satisfy the structural permit of PV systems. Roof information, mounting system structure, weight of the PV system, dead load and wind load of the roof are the key factors evaluated through structural permit. Utility currently follows the interconnection standard from IEEE 1547 which is the standard for interconnecting distributed resources with electric power systems [89]. NEC 705 also provides directions regarding the basic utility integration [87]. Power factor (pf), harmonic injection, grid synchronization, over current and under voltage disconnects, and anti-islanding are the technical aspects related to the utility permit. Once the PV installer completes the system installation per the codes and requirements, a permit

application is submitted for the site visit by the field inspectors and AHJs. As AHJs approve the system installation, another application is to be submitted for utility integration. The final approval for system operation comes from the utility. The overall process is time consuming and add unnecessary cost to the system, particularly for the residential PV system. The cost breakdown for the 2015 PV system installation in Fig. 6.3 shows that soft costs constitute the highest portion of system price in residential-scale systems compared to commercial and utility-scale system prices [81]. The proposed PnP concept with PUI system is designed for the residential system considering all these soft cost issues; the solution is discussed in the following sections.

6.3. 'Plug-and-Play' PV Electrical System

While the PnP system with PUI does not go as far as promoting the idea of utilities owning inverters, it is critical for the utility to own the PUI. Utility can monitor real-time data that enables proactive grid support through utility owned inverter, whereas utility-owned PUI can provide additional benefits as utilities agree that the ability to know PV production and performance of the grid is essential for grid management [82]. Additionally, a PnP solution with PUI would potentially provide further visibility that enables proactive grid support in real-time. Unanimous interest has been found with the utilities in receiving PV system information in real-time (pinged on a one-hour increment) in terms of kW output, voltage, and frequency. Furthermore, "edge device" features and functions such as ride-through capabilities, access to VAR control, and programmable setpoints for voltage and frequency are also desirable in a high penetration scenario, and PUI can be further modified to include those features.

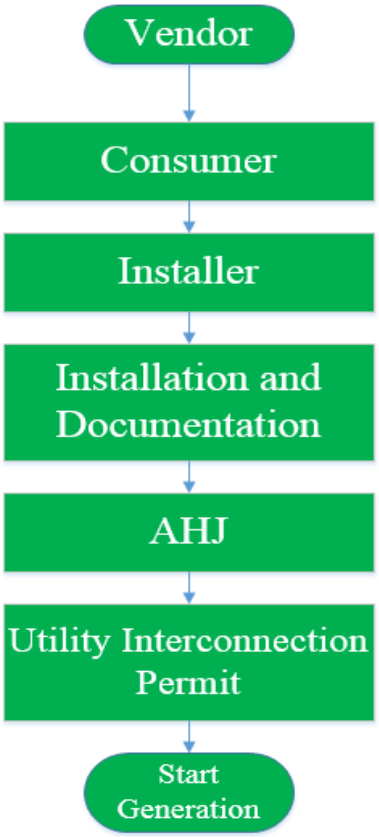

Figure 6.2. Current permitting process of PV system.

Utility ownership also shifts the long-term operation to utilities, which are equipped to maintain and upgrade infrastructure that will save overall system cost in the long run. In general, the proposed model opens the opportunity for enhanced customer services and programs that would automate the grid interconnection, and provide functionality to the utility to increase grid safety and stability.

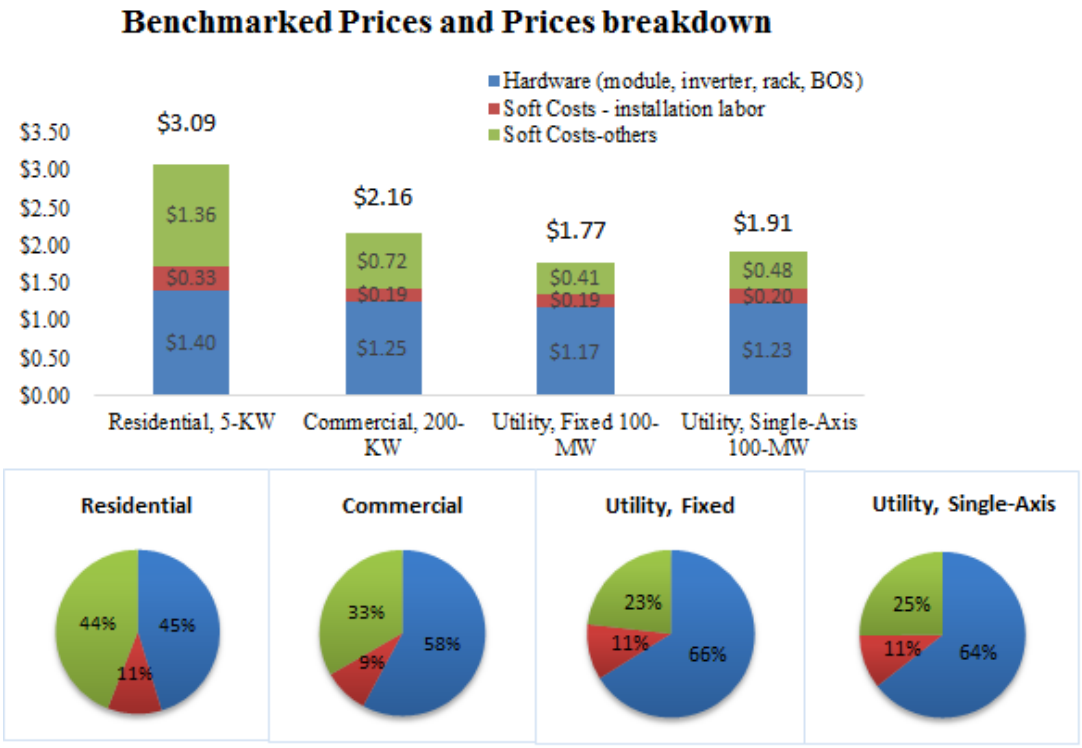

Figure 6.3. Benchmark price summary [81].

The PnP solution for the residential PV system must satisfy the National Electric Code (NEC), meet all interconnection and installation requirements, and be successfully inspected and permitted by the local AHJ for it to be accepted by AHJs and utilities as a safe and reliable method of producing solar power. A truly PnP system would be able to automate the inspection and permitting process as well as the interconnection agreement with the local utility company. Through the study of current codes and standards governing residential PV systems as well as interviews with AHJs and utility representatives, the designed PnP electrical system is built to provide an AHJ and utility vetted installation and interconnection procedure. The system uses UL-listed plugs, pre-sized components, and system-wide electrical safety checks to satisfy all the various safety codes and standards.

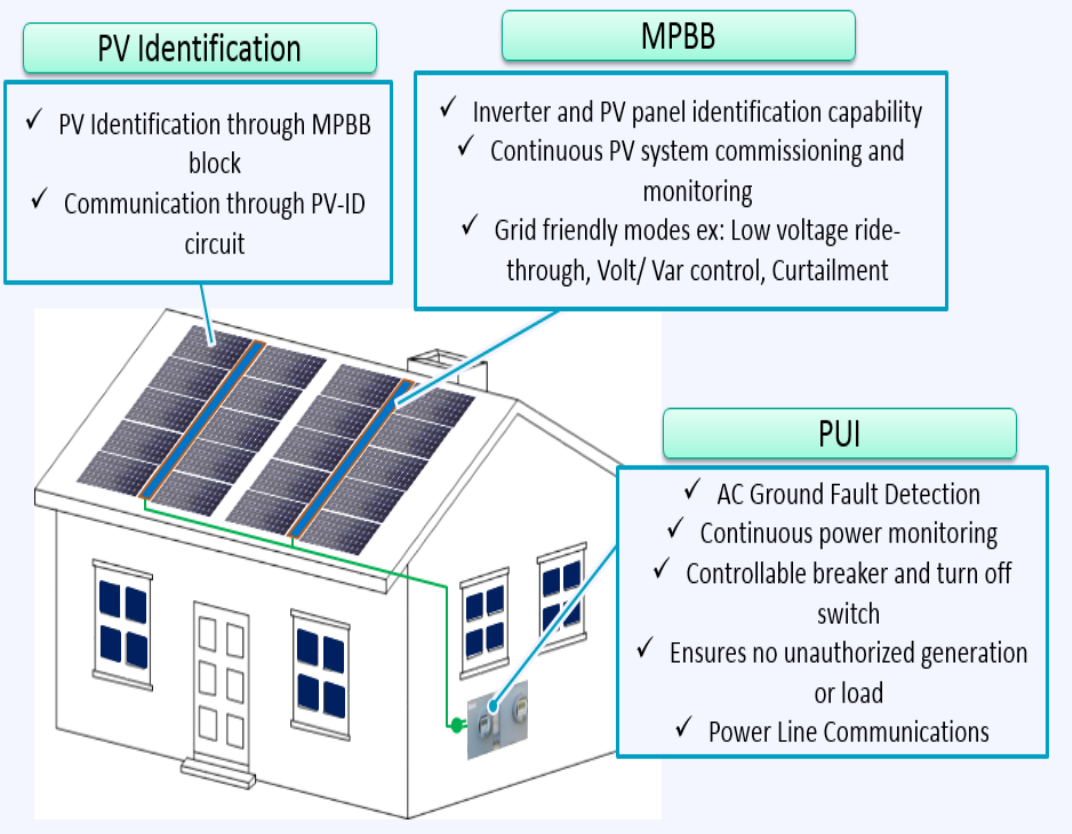

Figure 6.4: System-level ‘plug-and-play’ functions.

The system also features an innovative inverter design called the Multi-Port Building Block (MPBB) which has all the advantages of a large string inverter besides operating each panel independently like a microinverter [90]. The MPBBs are designed to have identification data pre-installed into its controller so that it may be read by the PUI upon start-up. The design and implementation of the MPBB has been carried out in a parallel project under the same DoE Sunshot program and is reported in [91]; only a brief description of MPBB is provided in the next section. A novel PV panel identification circuit has been added to the output wires of each panel that use current pulses, like serial communication, to transfer PV identification data to the MPBB controller. Fig. 6.4 shows the system level PnP functionalities.

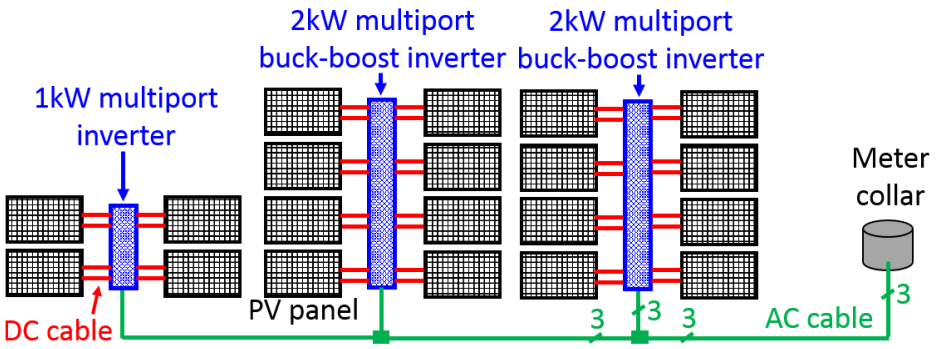

(a) Developed Multi-Port Building Block (MPBB) based PnP system.

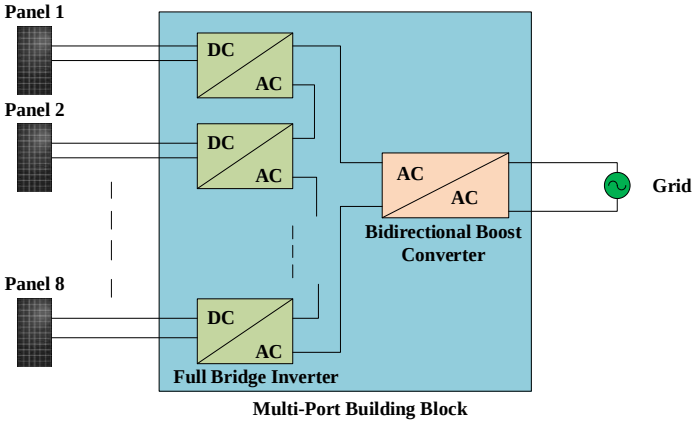

(b) Block Diagram of MPBB.

Figure 6.5: MPBB based 5 kW system.

6.4. Multi-port Building Block (MPBB)

Multi-Port Building Block (MPBB) encompasses the concept of stacking microinverters in the residential PV system in one integrated mechanical enclosure to enable a true PnP installation [91]. MPBB uses a non-isolated Buck-Boost type inverter that provides boost capability with very high efficiency. The solution combines the advantages of both string PV inverter and conventional microinverter based PV system. MPBB based PnP system along with the functional block diagram is provided in Fig. 6.5.

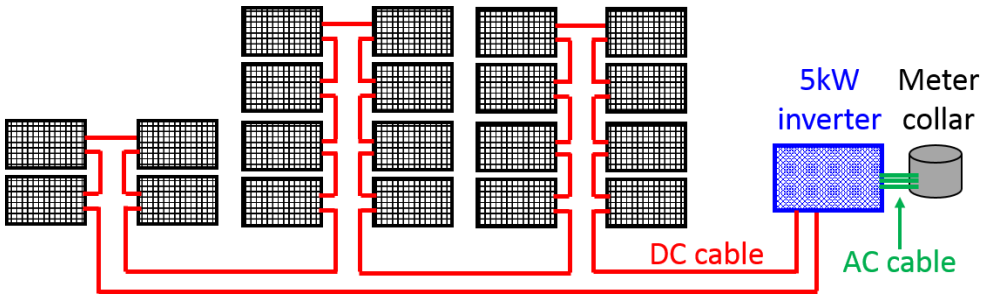

(a) String PV inverter system.

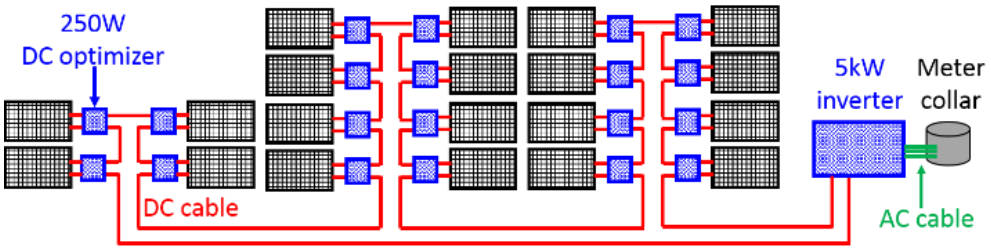

(b) DC optimizer plus string PV inverter system.

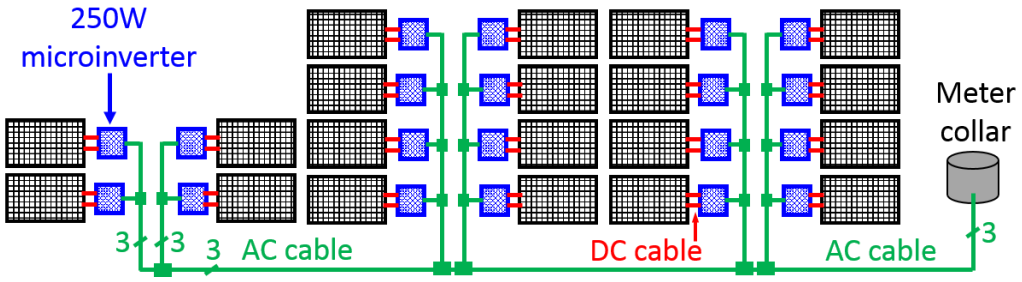

(c) PV microinverter system.

Figure 6.6: Three different types of residential 5 kW system.

In the proposed PV system, a maximum of 8 PV panels are allowed whose voltage sum is 240V; this is less than the maximum grid voltage 340V (240V RMS). The AC boost stage is Scalable power levels are realized by connecting the flexible number of MPBBs in parallel. In the MPBB based system, there is no risk of DC arc and the cost is significantly reduced compared to micro-inverter PV system. Moreover, the onsite installation time is effectively improved since the connectors, interconnection and wiring harnesses are simplified at the multiple PV panel level, and not at individual panels. MPBB based inverter has its own

disadvantages in terms of conduction and switching losses due to the two-stage power conversion, however the solution is better suited as a system level solution as it facilitates the installation and integration of PV system into the grid. Different configuration of PV system utilizing the string PV inverter, DC optimizer with string inverter, and microinverter for a 5kW system is also shown in Fig. 6.6.

6.5. Photovoltaic Utility Interface (PUI)

A functional prototype of the PUI has been designed and built. All PUI hardware and software are integrated into the utility meter itself and powered from the 240V supplied by the utility grid. This includes a master controller, current sensors, data display, wireless module, power line communications module, and a shunt-trip circuit that controls the AC breaker at the PV-meter connection point (Fig. 6.7). The control logic of the PUI ensures that no generation will take place unless all auto-inspection checks are passed and all generation sources are authenticated. Hardware housed in the meter interface includes ground fault detection circuit, over-current protection device (OCPD), safety relays, controllable shunt resistor to allow system checks prior to grid connection, and a control module to send and receive control signals from the rest of the system. Different ground fault detection methods have been studied to design the hardware, such that it can be housed inside the PV meter interface [92, 93]. Fig. 6.8 shows the PUI block connection and wiring diagram.

The PUI offers the flexibility of auto-permitted and self-authenticated PnP PV systems. The task of the PUI can be divided into two major parts; hardware checks and software checks. A two-layered PUI resides inside the utility meter which will provide the exciting opportunity to integrate this into any meter presently available in the market. The PUI hardware circuit

checks for the ground fault and processes data before running the start-up logic for the authentication of the system through software checks. All these analyses can be monitored in real-time through the display available in the circuit board. The PnP system will have to be UL certified for insertion into a utility meter socket, and the design requirements have been set accordingly. The ultimate goal of the auto-inspection process is not only to prove that it is equally safe as an AHJ in-person inspection, but also it can, in fact, be safer. Where some in-person inspection steps rely on visual observations, the PnP system with PUI can do these steps with real-time electrical safety measurements; where an installer commissions the system only once after installation, this system can re-commission itself periodically for proper operation and alert the owner of any possible problem. Start-up sequence, operation controls, and Graphical User Interface (GUI) demonstration setup have been created for system testing and to verify that the required data is being transferred and available for viewing by the customer, utilities, or authorities. The PUI features are summarized in Table 6.1. For its common use in applications where one master controller is communicating with several slave controllers, Modbus protocol is chosen as the communication protocol between the PUI and the MPBBs. The system uses power line communications across the power wires, and therefore, when a signal is sent from the PUI, it is received by every MPBB present in the system. Modbus protocol allows the PUI to communicate with a specific MPBB and guarantees each MPBB to only respond to a PUI request if that command addresses it specifically. This is especially useful when the PUI is involved in the identification of individual components or reading electrical measurement from specific points in the system.

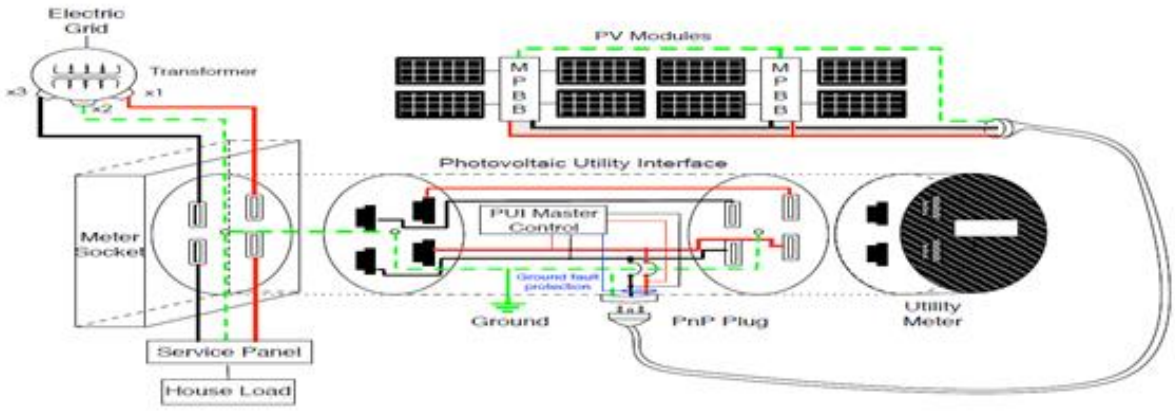

Figure 6.7: PnP system with PUI circuit.

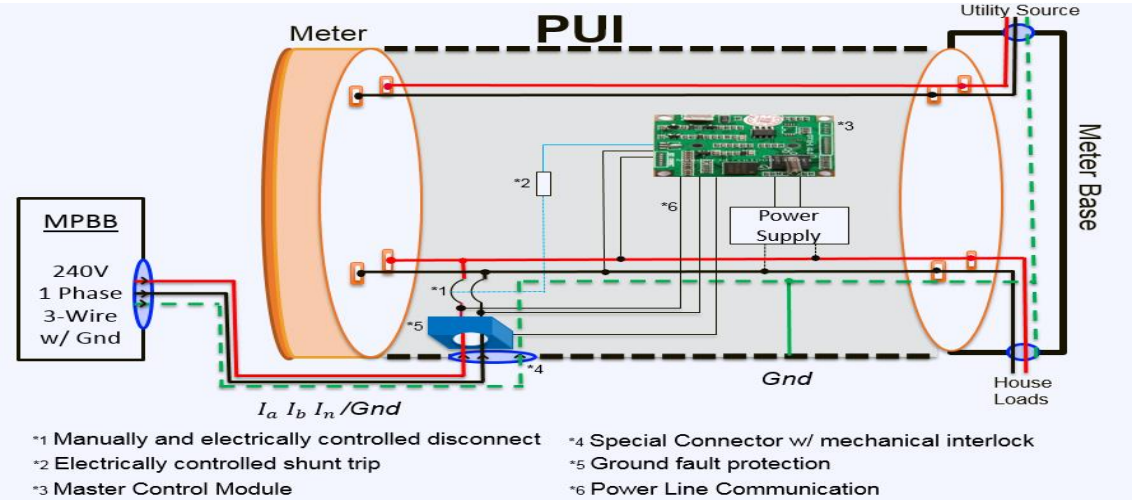

Figure 6.8: PUI wiring and power supply connection.

6.6. PUI Start up and System Authentication

The start-up and inspection sequence are key to the reliability and safety of the system. Before the PV system is plugged into the PUI, the breaker is kept open to ensure the safe operation. When the system is plugged in, the start-up procedure only begins then. If the device plugged into the PUI is found not to be a PnP System, the breaker will trip and no voltage will be allowed through the PUI. Fig. 6.9 shows a condensed flow chart of the PUI start-up sequence.

If any component of the system is not identified or found to be potentially unsafe for generation, then that component can be turned off and the rest of the system can function in their capacities. In addition to retrieving identification data for each MPBB, the PUI also requires to retrieve identification data from each PV panel. There are two possible solutions for obtaining the information by the PUI with each having its own pros and cons. The first solution is a microcontroller based circuit that is placed at the output of the module. When activated, this circuit uses current pulses from the PV module to transmit its identification data to the MPBB. This data can then be relayed to the PUI by the MPBB. The second solution involves placing an RFID transceiver inside each MPBB to trigger and receive data transmissions from RFID tags placed on the frame of each PV module. The microcontroller based circuit has been constructed and successfully tested. This solution has the advantage of being very low-cost, but brings up issues of PV module manufacturers' acceptance of the concept of adding the circuit to the output of their panels. The RFID approach has the disadvantage of being more expensive, but would only require PV module manufacturers to place an RFID tag somewhere on the module offering a much simpler addition to the module. Tags could also be put on other parts of the system to prove authenticity.

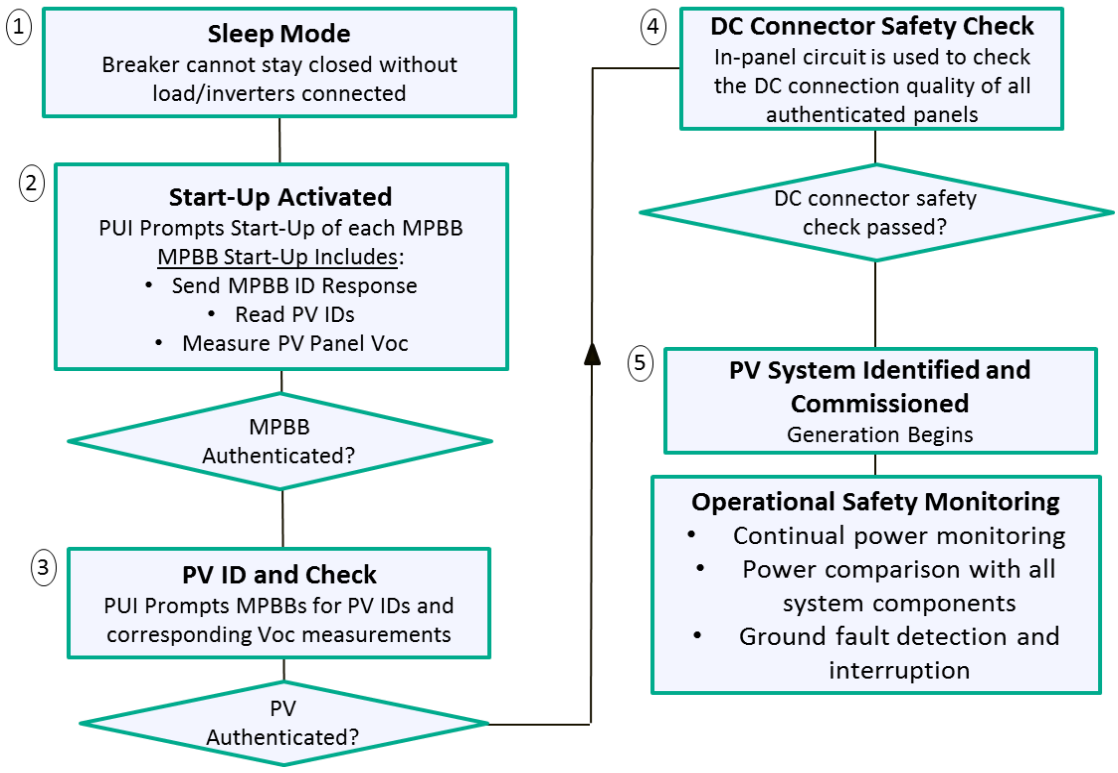

Figure 6.9: PUI daily start-up sequence.

Authentication for the system includes the checks to verify that the MPBB and the PV panel are genuine, that the number of PV modules connected match or are below the power level applied for from the utility, and that the PV power production does not exceed the PUI rating or permitted capacity. A commonly used master-slave protocol like Modbus is a suitable choice for this system since the PUI will be the master controller for this system [94]. To avoid errors and signal overlapping between multiple MPBBs, a five-byte standard accompanies each data transfer in the system. This standard includes the destination of the signal, the function requested, the memory register effected by the function, and a 16-bit error check. Each MPBB in the system is given an ID number.

Table 6.1: PUI ‘plug-and-play’ software functions.

Authentication	PV Panel and MPBB Identification and Authentication PV System Rating Check Number of Modules Connected
System Monitoring	Real-Time System Voltage, Current, and Power Checks Daily PV Panel and DC connection commissioning
Protection	AC and DC Ground Fault Protection, OCPD, Conductor, and Equipment Ratings Check
Communication Protocol	Power Line Communications Wireless Zigbee communications to a computer and display

When a signal is received, each MPBB will check the destination byte of the signal and will only respond if this destination byte matches its own ID number. Table 6.2 provides data byte example for PnP communications. It is by the Modbus standard that the system keeps track of what data is being requested and from which MPBB. Most functions, but certainly not all, requested by the PUI will be for information from the MPBBs. Therefore, the register number byte will usually refer to the memory register of the MPBB controller that holds the data being requested. In addition to data requests, the function ID byte can also trigger start-up or shutdown of parts of the system or can trigger measurements to be taken. Instead of doing this in a very general way, this protocol can be used in a very specific way. The destination IDs, functions, and registers requested can be customized to be used specifically between a PnP PUI and the MPBBs that it is connected to. This helps to make the protocol simpler with fewer possible requests that are applicable to the system. Table 6.3 gives an example of the data protocol in hex format.

Table 6.2: Byte data examples for PnP communications.

Destination IDs	
PUI ID	0x01
MPBB 1 ID	0x02
MPBB 1 ID	0x03
MPBB 1 ID	0x04

Register IDs	
MPBB ID and Start-up Request	0x00
PV Panel ID Request	0x09…0x10
PV Voltage and DC Connection Check	0x09… 0x10
System Approved for Generation	0x11

The protocol displayed is used when the PUI sends a read function request (0x03) to MPBB 1 asking for PV Panel 6 identification. The MPBB then responds to the read request by sending the PV Panel 6 ID back to the PUI. Through the testing procedure, it is resolved that the PV identification circuit can also be used to test the DC-connector from PV panel to MPBB. Since the PV-ID circuit allows the system to receive accurate measurements from both sides of the DC-connector, it helps the system to test the connector for safety and fire prevention. Fig. 6.10 shows the full start-up and sequential logic for the PUI circuit.

Table 6.3: Communications protocol example.

Request	[Destination ID] [Function ID] [Register Number] [16-bit Error Check]
	[0x02] [0x03] [0x06] [0x****]
Response	[Destination ID] [Function ID] [Register Number] [Response Data] [16-bit Error Check]
	[0x01] [0x03] [0x06] [“PLUGnPLAY250W”] [0x****]

6.7. Prototype and Experimental Results

A functional PUI electrical prototype has been built and tested. It demonstrates PV system authentication, electrical safety checks, and internal communications with MPBBs through the use of power line communications. Auto-inspection logic and controls for the start-up sequence have been checked and a GUI setup is being developed for error checking. GUI is essential to confirm that the expected data has been transmitted and is available for viewing. This circuitry includes all power, control, sensor interface, and communication circuits. Fig. 6.11 and 6.12 show the built circuit for version 1.0. Meter adapter is shown in Fig. 6.13. All the components within the circuit that take up volume (such as power converters and transformers) are reduced in size by 50% or more in version 2.0 and the placements of these components are carefully chosen to allow for the maximum amount of hardware to be housed in the limited space available in the utility meter which is shown in Fig. 6.14 and Fig. 6.15.

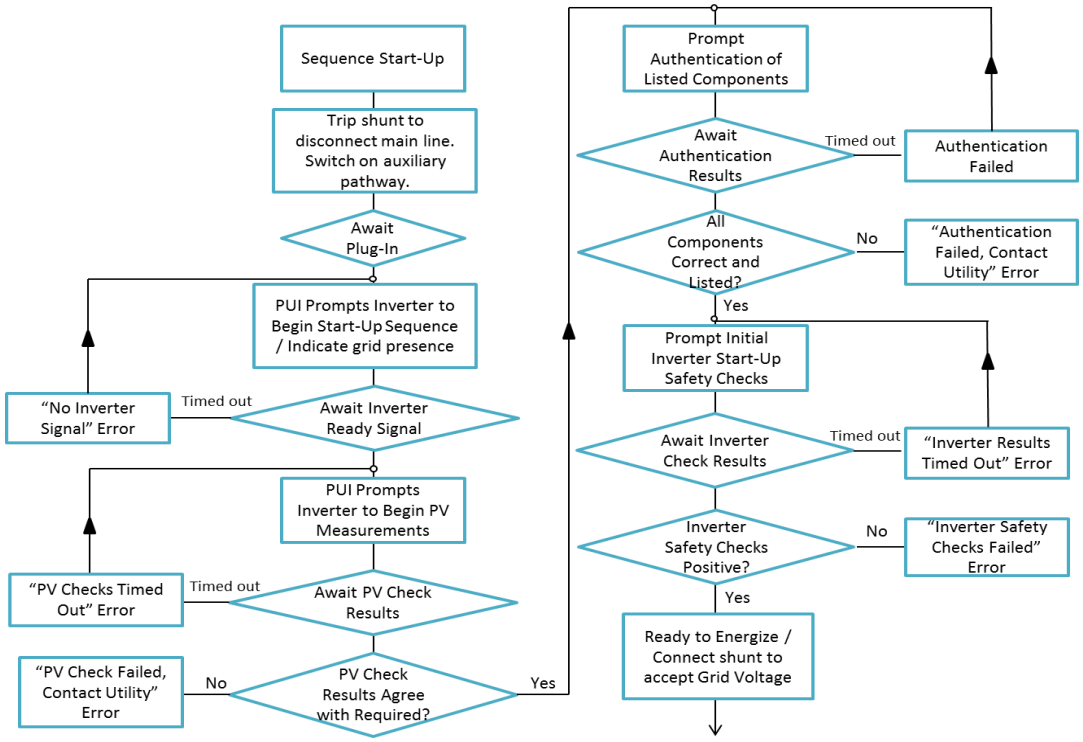

Figure 6.10: Start-up and sequential logic for PUI.

The shunt-trip controlled AC breaker in version 2.0 demonstrates an improvement in PV system safety. The tests show that the control circuit can stop the flow of electricity through the power wires within 1.5 cycles (approximately 20ms) after an electrical fault has occurred as shown in Fig. 6.16. Compared to a standard GFI outlet's trip-off time of 5-6 cycles, this is an encouraging result. Preliminary data displays have been tested to allow PUI demonstrations and system testing to verify that the required data is being transferred and is available for viewing by all interested parties. Though currently only being used for demonstration purposes, the PUI contains wireless data capability that could transmit data to a nearby wireless internet connection or a local computer. In a real-world scenario, the PUI would be used to communicate system data to the user, and in addition, to communicate with the local AHJs and utility company to aid in the auto-permitting and interconnection process. Documentation flow and approval process can be streamlined by integrating the PUI circuit with a web portal which will simplify the permitting process. The steps in the proposed process to complete the installation without any site visit by the authorities are shown in Fig. 6.17.

Step 1: Vendors upload all related product information along with certification information beforehand into the web portal. AHJs and utility verify whether equipment satisfying code requirements are being listed to use by the customer. This step does not involve the customers.

Step 2: Consumer searches for authorized vendor from the web portal and orders the product.

Step 3: Consumer contacts the certified installer to install the PV system.

Step 4: Installer completes installation according to the guidelines, ensures code compliance, and initiates the PUI automation for the system checks and then PUI transfers the results to the web portal.

Step 5: Local AHJs are notified from the web portal with the PUI results.

Step 6: AHJ reviews and approves the installation through the web portal.

Step 7: Utility is contacted through the web portal upon approval from the AHJ.

Step 8: Utility reviews and provides the approval code to the portal which is then assigned with the installed PV system. This enables the PUI to complete the system self-diagnostics.

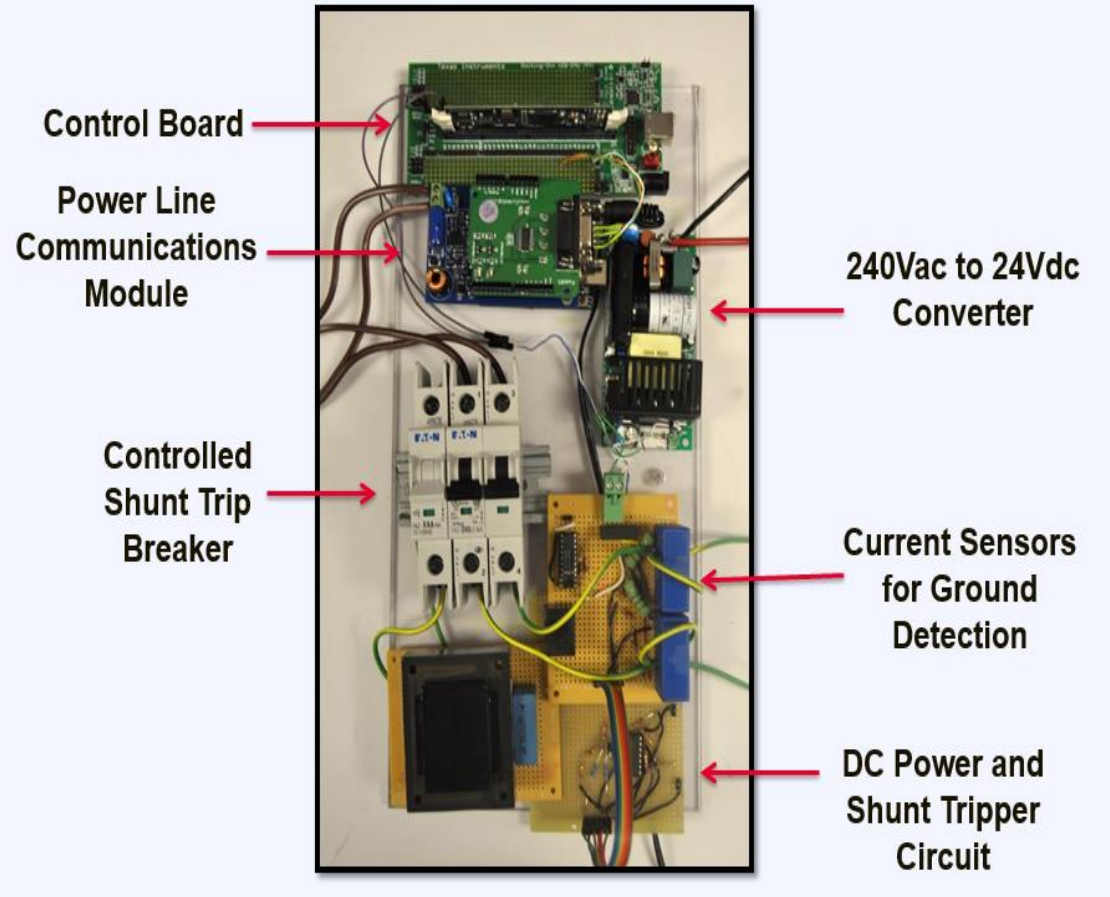

Figure 6.11: PUI version 1.0 (Test circuit).

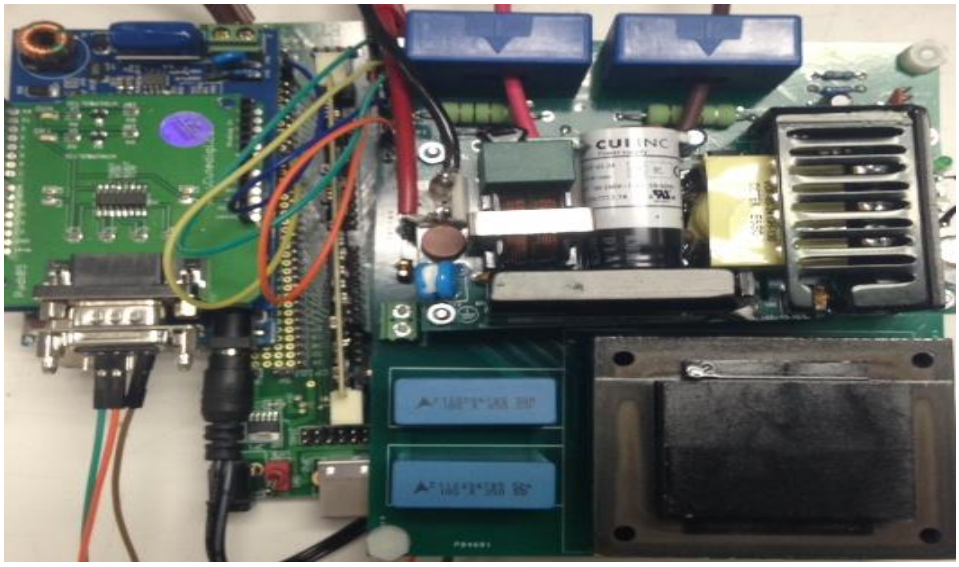

Figure 6.12: PUI version 1.0 prototype.

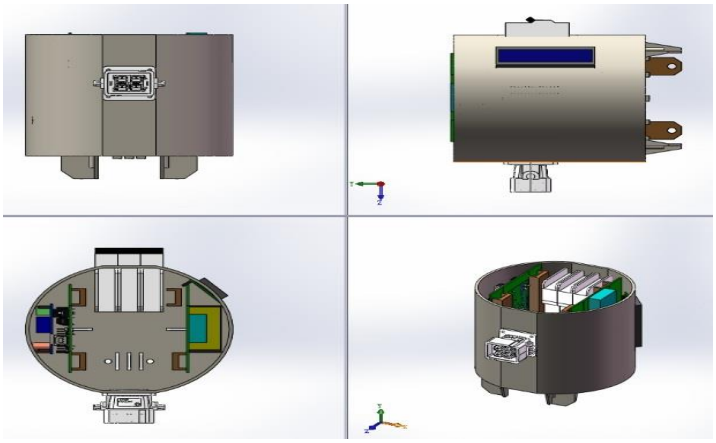

Figure 6.13: PUI meter adapter.

Figure 6.14: PUI version 2.0 prototype.

Figure 6.15: PUI adapter installed between meter and meter base.

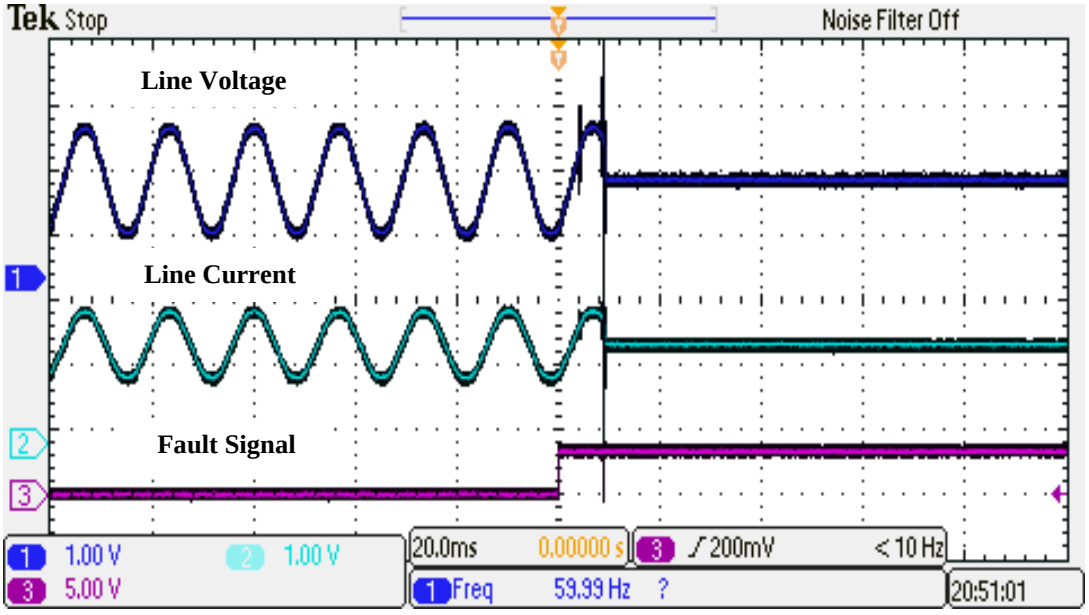

Figure 6.16: Shunt trip test ground fault results with PUI version 1.0.

In the proposed process, there is no additional task for the consumer other than buying the system from the vendor and contacting the installer; the process is automated through the web portal with the help of the developed PUI. The whole process can be completed within hours to several days depending on the system size and installer installation time whereas it takes two weeks to months for getting the installation approval by the present process. In the proposed process, there is no additional task for the consumer other than buying the system

from the vendor and contacting the installer; the process is automated through the web portal with the help of the developed PUI. The whole process can be completed within hours to several days depending on the system size and installer installation time whereas it takes two weeks to months for getting the installation approval by the present process.

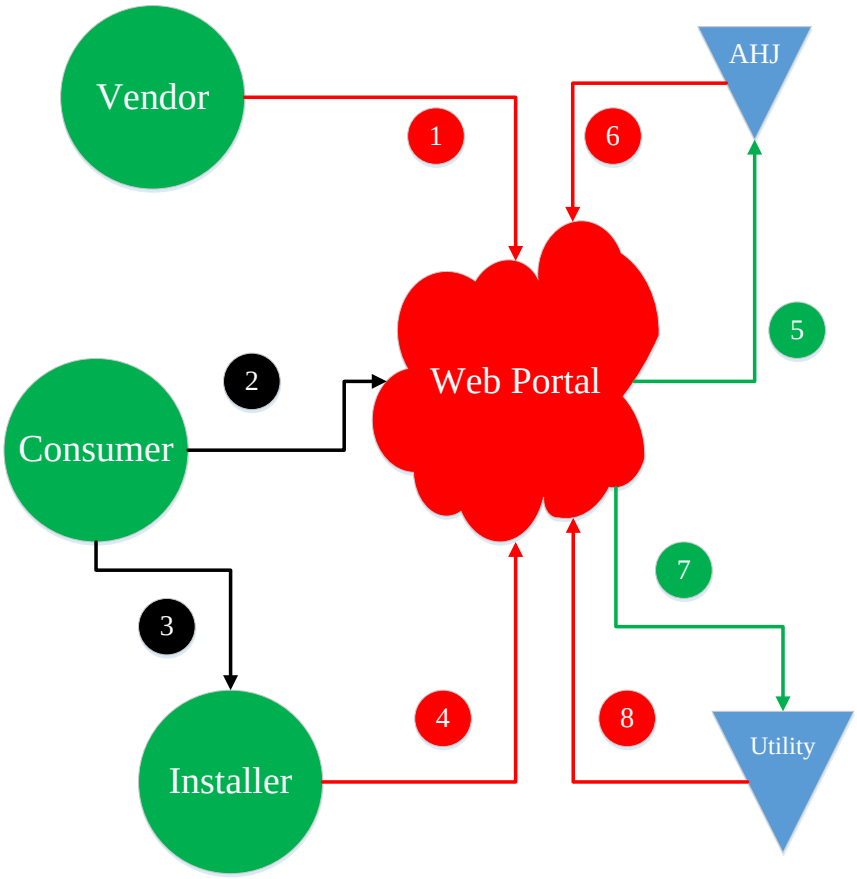

Figure 6.17. Web portal for PV permitting process.

A GUI is also developed and tested for the system authentication and function verification of the PUI which is shown in Fig. 6.18. The interface consists of 4 screens that focus on installation, authentication, safety and reliability, and power generation. The interface takes the end-user measurement through the complete PnP start-up procedure, then displays real-time data during generation. All authentication checks and safety measurements are clearly displayed in real-time and the number of PV modules and MPBBs connected to the system

are shown throughout the daily operation. During generation, the interface displays the power processed by each MPBB, total power measured at the PUI, measured ground fault current, breaker status (open or closed), and the total energy produced during that day.

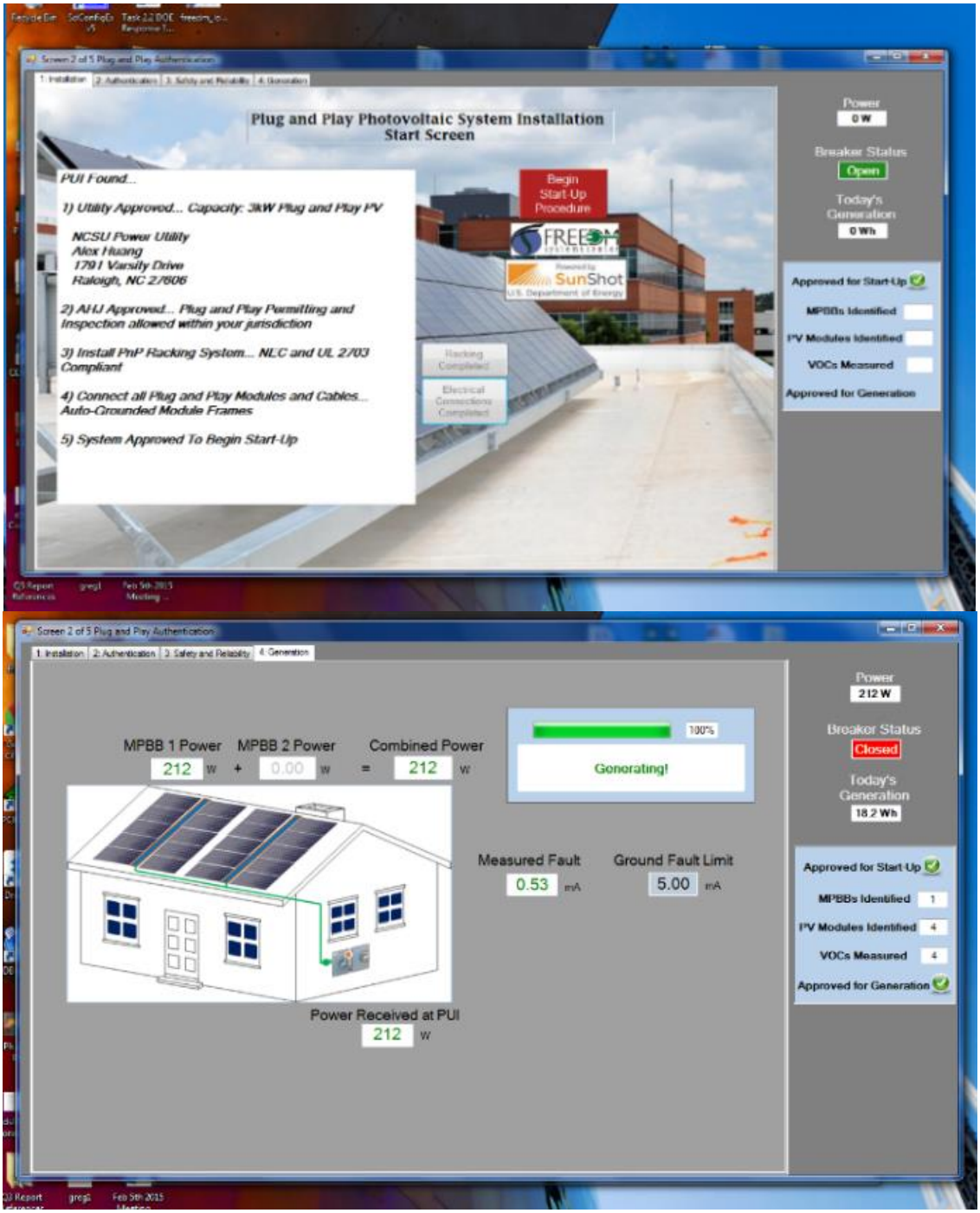

Figure 6.18: Graphical user interface used for PnP system data display.

6.8. Cost analysis of the System

Residential system price has experienced 56% decrease since 2009 as equipment cost has declined significantly; however, the price drop has slowed down in the last few years as the hardware cost reached saturation levels [81]. The reduction in soft cost is not promising as those costs are mainly added due to the installation and interconnection approval, which remained very much the same over the years. The developed PnP method utilizes the detailed cost breakdown for residential system using NREL's benchmark [81]. The installation time recorded in the project demonstration is 1 hour and 21 minutes with the PUI requiring only 10 minutes to connect and another 5 minutes to automate the permitting procedure. This is a significant reduction in time compared to the present installation time of 1-2 days which is equivalent to 50 person-hours for a 5 kW system [81]. There is the added cost for the PUI, but this is minimal compared to the present soft cost of the PV system. Table 6.4 provides the cost breakdown of PUI based on a 3 kW system that has been demonstrated. The system also includes an innovative racking design for the installation of the PV panels which is not related to PUI and is reported in [95]. The PUI based system reduces the installation time by 95% which will result in a saving of $0.30/W compared to 2015 benchmark price. There is $0.11/W cost associated with residential system for the permitting and inspection which will eventually be eliminated through this automated process. In summary, there will be a saving of $0.30/W utilizing the PUI, and the cost estimate including the racking and MPBB is $.405/W compared to today's $1/W.

6.9. Contribution

1. Novel automated PUI design for ‘plug-and-play’ PV installation with reduced cost and time.

2. System demonstration of the developed hardware for a typical residential PV system that shows a reduction of installation time by 95% to the present practice.

3. Developed PUI hardware will reduce the PV system cost by $0.3/watts which will ultimately lower the soft cost related with PV residential system.

4. Development of novel web interface architecture and system level checks to eliminate all the physical checks required for PV system installation.

Table 6.4: PUI cost breakdown.

Cost Breakdown	PUI (3 KW System)
Unit Cost($)	$280
$/W (based on quantity of 1)	$.093
Estimated cost @ high quantity	$112
Estimated $/W @ high quantity	$.037

6.10. Conclusions

Through innovative circuits and system-level functionalities a PnP PV system can, in many ways, be safer and more reliable than a traditionally installed PV system. An integrated PV system has been designed that can conduct all the verifications and procedures required to automate the inspection, permitting, and interconnection process with proper AHJ and utility acceptance. Control logic and communications protocol have been incorporated to this

application to facilitate the information exchange between the PUI and MPBBs, as well as to automate inspection and system monitoring. The desired result of using a PnP PUI is to significantly reduce the upfront expenses by automating the processes while replacing the arduous electrical installation process with a simple, plug-based meter connection that adds negligible cost to the system. The next step is one that has less to do with the technology and design, but more to create a market entry plan to convince the utilities. For this utility owned device for use by a solar customer, they would expect to be compensated through charging the user either through a monthly fee or a one-time installation fee.

CHAPTER 7

SUMMARY AND FUTURE WORK

7.1. Summary

7.2. Future Work

7.1. Summary

This section summarizes the dissertation to highlight the findings and contributions.

1. In chapter two, detailed FREEDM power distribution model along with renewable generation and storage systems and their corresponding interface circuits to DC and AC buses is developed.
2. Solid-state transformer based power distribution system (the FREEDM system) is analyzed for feasibility bounds in steady-state following the development of a 70^{th}-order state-space system representation. The analysis defines the feasible operational bounds for FREEDM system to study system level failures in distribution network.
3. IEEE 34 bus simulation verifies the proposed feasibility constraint and the analysis lays out the background to study power sharing capability of networked microgrid in the multiple-SST connected FREEDM system. Validation of feasibility constraints are verified in chapter five with IEEE 34 bus.
4. In chapter three, power sharing methods are proposed to maintain the feasibility of the system when there is a change in the load of any of the SSTs for a multiple-SST power distribution network in tree configuration. Two methods are proposed to maintain the system feasibility without running the power flow and then, validation model is built for verification of the proposed approach.
5. Control layers for energy and power balance are introduced based on the feasibility study. Controller interaction and then, their subsequent architecture is proposed for the distributed or decentralized controller design of a multiple-SST network along with their corresponding time-scale separation.

6. Energy storage controller to support the dynamic variation in SST based microgrid is developed in chapter four. The controller takes feasibility into the consideration to maintain the steady-state regulation of the internal SST states with the presence of generation or load variation in microgrid.
7. Storage controller is then formulated to enable the power sharing methods developed in chapter three. Stability of the overall system with the storage controller is also verified for an n-SST system.
8. In chapter five, system level simulation to identify the failure in distribution network is presented and then the power sharing methods are demonstrated in the modified IEEE 34 bus with the energy storage controller.
9. In chapter six, the existing requirements for the permitting process of solar PV systems are discussed to implement the PnP system for residential units and then, the PnP electrical system, with emphasis on the controls, software, and system level communications within the system is designed for a residential system.
10. A smart interface with web portal based permitting process is proposed that is expected to increase the numbers of residential PV installation. A PV Utility Interface (PUI) circuit has been developed for automated electrical safety checks and authentication for the PnP PV system. A data protocol is introduced to deal with the master-slave controller setup in the system. This research has the potential to reduce residential PV system price by $0.3/watt.

7.2. Future Work

This section provides an insight of the achievable future works out of this research work.

1. All of the analysis in this dissertation deals with the steady-state feasibility study to develop the power sharing capability of a special type of power distribution system named FREEDM. The next step should be studying the stability performance of such a system through designing robust controllers for IEM and IPM which would guarantee comprehensive performance of the system with the instantaneous changes in the load of the system.
2. Weak grid/islanded mode of operation of SST based system needs to be studied where defining the weak grid will dominate the state-space modeling and subsequent system design. It is important to develop the similar study that has been carried out in this dissertation considering the grid as islanded or weak to support the required load demand. This kind of study will assist universal controller design for any mode of operation alongside the regular grid operation to maintain the stability.
3. Development of optimum power flow analysis for IEM would be something interesting which is essential for the start-up/initial operation of FREEDM in reality. IEM can be designed considering the physical constraints developed from the feasibility study along with the load demand, RES generation forecast, and economic constraints.
4. Parameters and set points play an important role in the definition of the feasibility of FREEDM system. Power electronics parameters like filter resistance for the SST can be designed based on the location in the distribution feeder which will enable further extended feasible operation. This kind of analysis will provide the pathways for optimized selection of the power electronics components for hardware development. Also, the impact of tie line impedances can be added as a part of the study.

5. Storage sizing along with the developed controller can be studied for an optimal operation of the microgrid network. Also, the storage placement can be analyzed considering the power sharing methods.
6. Communication protocol and medium are very critical for the efficient implementation of power sharing. As shown in this dissertation, communication delay plays significant role in the steady-state regulation of the internal SST while power sharing, defining the communication network based on feasibility criteria for power sharing methods will be an interesting topic to continue.
7. Designed PnP PUI significantly reduces the upfront expenses by automating the processes while replacing the arduous electrical installation process. However, due to the fact that NEC still technically does not permit for user-plugged PV systems, further research will be necessary to get the system UL-listed as a PnP system, and to make changes to the NEC standards to allow for the PnP based PV systems.
8. The concerns for the utilities, as identified through a survey as a part of this research while developing the PUI, is the business and market orientation of PUI relating the cost of liability, timing, cross subsidization, compensation, and assignment of costs. The next step of research with PUI is one that has less to do with the technology and design, but more to create a viable business case for the utilities.

REFERENCES

[1] McCrone, Angus; Moslener, Ulf; d'Estais, Francoise; Usher, Eric; Gruning, Chistine, *Global Trends in Renewable Energy Investment*, Frankfurt School-UNEP Centre, Frankfurt, Germany, 2016.

[2] Sawin, Janet L.; Seyboth, Kristin; Sverrisson, Freyr, *Renewables 2016 Global Status Report*, Renewable Energy Policy Network for the 21st Century Secretariat, Paris, France, 2016.

[3] Canete, Miguel, *The European Union Leading in Renewables*, European Commission, Brussels, Belgium, 2015.

[4] Gielen, Dolf; Saygin, Deger; Wagner, Nicholas, *Renewable Energy Prospects: United States of America, Remap 2030*, International Renewable Energy Agency, Abu Dhabi, Jan '2015.

[5] K. Schneider; F. Tuffner; M. Elizondo; C. C. Liu; Y. Xu; D. Ton, "Evaluating the Feasibility to Use Microgrids as a Resiliency Resource," in *IEEE Transactions on Smart Grid* , vol.PP, no.99, pp.1-1

[6] J. He, Y. W. Li and F. Blaabjerg, "Flexible Microgrid Power Quality Enhancement Using Adaptive Hybrid Voltage and Current Controller," in *IEEE Transactions on Industrial Electronics*, vol. 61, no. 6, pp. 2784-2794, June 2014.

[7] R. Yan and T. K. Saha, "Voltage Variation Sensitivity Analysis for Unbalanced Distribution Networks Due to Photovoltaic Power Fluctuations," in *IEEE Transactions on Power Systems*, vol. 27, no. 2, pp. 1078-1089, May 2012.

[8] Reinaldo Tonkoski, Luiz A. C. Lopes, and Tarek H. M. El-Fouly, "Coordinated Active Power Curtailment of Grid Connected PV Inverters for Overvoltage Prevention," IEEE Transactions on Sustainable Energy, Vol. 2, No. 2, pp. 139-147, April 2011.

[9] Saeed Alyami, Yang Wang, Caisheng Wang,, Junhui Zhao, and Bo Zhao, "Adaptive Real Power Capping Method for Fair Overvoltage Regulation of Distribution Networks With High Penetration of PV Systems," IEEE Trans. on Smart Grid, Vol. 5, No. 6, November 2014.

[10] A. Safayet, P. Fajri and I. Husain, "Reactive power management for overvoltage prevention at high PV penetration in low voltage distribution system," *2015 IEEE Energy Conversion Congress and Exposition (ECCE)*, Montreal, QC, 2015, pp. 1988-1994.

[11] Erhan Demirok, Pablo Casado Gonz´alez, H. B. Frederiksen, Dezso Sera, Pedro Rodriguez, and Remus Teodorescu, "Local Reactive Power Control Methods for

Overvoltage Prevention of Distributed Solar Inverters in Low-Voltage Grids," IEEE Journal Of Photovoltaics, Vol. 1, No. 2, December 2011.

[12] P. Fortenbacher, M. Zellner and G. Andersson, "Optimal sizing and placement of distributed storage in low voltage networks," *2016 Power Systems Computation Conference (PSCC)*, Genoa, 2016, pp. 1-7.

[13] M. J. E. Alam, K. M. Muttaqi and D. Sutanto, "Distributed energy storage for mitigation of voltage-rise impact caused by rooftop solar PV," *2012 IEEE Power and Energy Society General Meeting*, San Diego, CA, 2012, pp. 1-8.

[14] S. Kotra and M. K. Mishra, "Energy management of hybrid microgrid with hybrid energy storage system," *2015 International Conference on Renewable Energy Research and Applications (ICRERA)*, Palermo, 2015, pp. 856-860.

[15] P. C. Sekhar and S. Mishra, "Storage Free Smart Energy Management for Frequency Control in a Diesel-PV-Fuel Cell-Based Hybrid AC Microgrid," in *IEEE Transactions on Neural Networks and Learning Systems*, vol. 27, no. 8, pp. 1657-1671, Aug. 2016.

[16] F. Marra, Y. T. Fawzy, T. Bülo and B. Blažic, "Energy storage options for voltage support in low-voltage grids with high penetration of photovoltaic," *2012 3rd IEEE PES Innovative Smart Grid Technologies Europe (ISGT Europe)*, Berlin, 2012, pp. 1-7.

[17] G. Wang *et al*., "A Review of Power Electronics for Grid Connection of Utility-Scale Battery Energy Storage Systems," in *IEEE Transactions on Sustainable Energy*, vol. 7, no. 4, pp. 1778-1790, Oct. 2016.

[18] Y. Yang and H. Li, "Performance analysis of LiFePO4 battery energy storage for utility-scale PV system," *2014 IEEE Energy Conversion Congress and Exposition (ECCE)*, Pittsburgh, PA, 2014, pp. 414-419.

[19] D. Apostolopoulou, A. D. Domínguez-García and P. W. Sauer, "An Assessment of the Impact of Uncertainty on Automatic Generation Control Systems," in *IEEE Transactions on Power Systems*, vol. 31, no. 4, pp. 2657-2665, July 2016.

[20] Z. Li, C. Zang, P. Zeng, H. Yu and S. Li, "Agent-based distributed and economic automatic generation control for droop-controlled AC microgrids," in *IET Generation, Transmission & Distribution*, vol. 10, no. 14, pp. 3622-3630, 11 4 2016.

[21] A. Q. Huang, M. L. Crow, G. T. Heydt, J. P. Zheng, and S. J. Dale, ``The Future Renewable Electric Energy Delivery and Management (FREEDM) System: The Energy Internet," in *Proceedings of the IEEE*, vol. 99, no. 1, pp. 133-148, Jan. 2011.

[22] X. She, X. Yu, F. Wang, and A. Q. Huang, ``Design and Demonstration of a 3.6-kV 120-V/10-kVA Solid-State Transformer for Smart Grid Application," in *IEEE Transactions on Power Electronics*, vol. 29, no. 8, pp. 3982-3996, Aug. 2014.

[23] T. Zhao, J. Zeng, S. Bhattacharya, M. E. Baran, and A. Q. Huang, ``An Average Model of Solid State Transformer for Dynamic System Simulation," in *IEEE Power & Energy Society General Meeting*, Calgary, Canada, 2009.

[24] X. Yu, X. She, X. Ni and A. Q. Huang, "System Integration and Hierarchical Power Management Strategy for a Solid-State Transformer Interfaced Microgrid System," in *IEEE Transactions on Power Electronics*, vol. 29, no. 8, pp. 4414-4425, Aug. 2014.

[25] Y. Jiang, L. Breazeale, R. Ayyanar and X. Mao, "Simplified Solid State Transformer modeling for Real Time Digital Simulator (RTDS)," *2012 IEEE Energy Conversion Congress and Exposition (ECCE)*, Raleigh, NC, 2012, pp. 1447-1452.

[26] V. Ramachandran, A. Kuvar, U. Singh, S. Bhattacharya and M. Baran, "A system level study employing improved solid state transformer average models with renewable energy integration," *2014 IEEE PES General Meeting | Conference & Exposition*, National Harbor, MD, 2014, pp. 1-5.

[27] Z. Yu, R. Ayyanar, I. Husain, "A detailed analytical model of a solid-state transformer," *in Energy Conversion Congress and Exposition (ECCE)*, 2015 IEEE, pp.723-729, 20-24 Sept. 2015.

[28] D. G. Shah and M. L. Crow, ``Stability Design Criteria for Distribution Systems With Solid-State Transformers," in *IEEE Transactions on Power Delivery*, vol. 29, no. 6, pp. 2588-2595, Dec. 2014.

[29] F. Wang, X. Lu, W. Y. Wang, and A. Q. Huang, “Development of distributed grid intelligence platform for solid state transformer,” in Proc. IEEE Smart Grid Commun., 2012, pp. 481–485.

[30] X. She, A. Q. Huang, and X. J. Ni, “Current sensorless power balance strategy for a cascaded multilevel converter based solid state transformer,” IEEE Trans. Power Electron., vol. 29, no. 1, pp. 17–22, Jan. 2014.

[31] Hao Li, Ying Sun, Kejun Li, Wenwen Xiao, Mi Xu and Liyuan Gao, "Research on grid-connected photovoltaic power generation technology based on FREEDM system," *TENCON 2015 - 2015 IEEE Region 10 Conference*, Macao, 2015, pp. 1-6.

[32] A. M. S. S. Andrade; L. Schuch; M. L. da S. Martins, "High Step-Up PV Module Integrated Converter for PV Energy Harvest in FREEDM Systems," in *IEEE Transactions on Industry Applications* , vol.PP, no.99, pp.1-1.

[33] F. Wang, G. Wang, A. Huang, W. Yu and X. Ni, "Rectifier stage operation and controller design for a medium voltage solid state transformer with LCL filter," *2014 IEEE Energy Conversion Congress and Exposition (ECCE)*, Pittsburgh, PA, 2014, pp. 3642-3649.

[34] J. Shi, W. Gou, H. Yuan, T. Zhao and A. Q. Huang, "Research on voltage and power balance control for cascaded modular solid-state transformer," in *IEEE Transactions on Power Electronics*, vol. 26, no. 4, pp. 1154-1166, April 2011.

[35] H. Hu, X. She and A. Q. Huang, "A high performance controller for a single phase cascaded multilevel photovoltaic system," *2014 IEEE Energy Conversion Congress and Exposition (ECCE)*, Pittsburgh, PA, 2014, pp. 2538-2543.

[36] H. Khorramdel, J. Aghaei, B. Khorramdel and P. Siano, "Optimal Battery Sizing in Microgrids Using Probabilistic Unit Commitment," in *IEEE Transactions on Industrial Informatics*, vol. 12, no. 2, pp. 834-843, April 2016.

[37] A. Saez-de-Ibarra, A. Milo, H. Gaztañaga, V. Debusschere and S. Bacha, "Co-Optimization of Storage System Sizing and Control Strategy for Intelligent Photovoltaic Power Plants Market Integration," in *IEEE Transactions on Sustainable Energy*, vol. 7, no. 4, pp. 1749-1761, Oct. 2016.

[38] H. Dagdougui, N. Mary, A. Beraud-Sudreau and L. Dessaint, "Power management strategy for sizing battery system for peak load limiting in a university campus," *2016 IEEE Smart Energy Grid Engineering (SEGE)*, Oshawa, ON, 2016, pp. 308-312.

[39] M. T. A. Khan, A. A. Milani, A. Chakrabortty and I. Husain, "Comprehensive dynamic modeling of a solid-state transformer based power distribution system," *2016 IEEE Energy Conversion Congress and Exposition (ECCE)*, Milwaukee, WI, 2016, pp. 1-8.

[40] M. T. A. Khan, A. Afiat Milani, A. Chakrabortty and I. Husain, "Dynamic Modeling and Feasibility Analysis of a Solid-state Transformer Based Power Distribution System," in *IEEE Transactions on Industry Applications*, vol. PP, no. 99, pp. 1-1.

[41] A. Afiat Milani, M. T. A. Khan, A. Chakrabortty and I. Husain, "Equilibrium Point Analysis and Power Sharing Methods for Distribution Systems Driven by Solid-State Transformers," in *IEEE Transactions on Power Systems*, vol. PP, no. 99, pp. 1-1.

[42] M. T. A. Khan, I. Husain and D. Lubkeman, "Power electronic components and system installation for plug-and-play residential solar PV," *2014 IEEE Energy Conversion Congress and Exposition (ECCE)*, Pittsburgh, PA, 2014, pp. 3272-3278.

[43] M. T. A. Khan, G. Norris, R. Chattopadhyay, I. Husain and S. Bhattacharya, "Auto-inspection and permitting with a PV Utility Interface (PUI) for residential plug-and-play solar photovoltaic unit," *2015 IEEE Energy Conversion Congress and Exposition (ECCE)*, Montreal, QC, 2015, pp. 5763-5770.

[44] M. T. A. Khan, G. Norris, R. Chattopadhyay, I. Husain and S. Bhattacharya, "Auto-inspection and Permitting with a PV Utility Interface (PUI) for Residential Plug-and-Play Solar Photovoltaic Unit," in *IEEE Transactions on Industry Applications*, vol. 53, no. 2, pp. 1337-1346, March-April 2017.

[45] X. W. Yu, X. She, X. H. Zhou, and A. Q. Huang, "Power management for DC microgrid eneabled by solid-state transformer," in *IEEE Trans. Smart Grid*, vol. 5, no. 2, pp. 954–965, Mar 2014

[46] J. W. Kimball and P. T. Krein, “Singular perturbation theory for dc– dc converters and application to PFC converters,” *in Proc. IEEE Power Electron. Spec. Conf.,* Orlando, FL, 2007, pp. 882–887.

[47] H. Bai, C. Mi, C. Wang, and S. Gargies, “The dynamic model and hybrid phase-shift control of a dual-active-bridge converter,” *in Proc. 34th Annu. IEEE IECON*, Nov. 2008, pp. 2840–2845.

[48] A. Emadi, "Modeling and analysis of multi-converter DC power electronic systems using the generalized state-space averaging method," in *Industrial Electronics, IEEE Transactions on* , vol.51, no.3, pp.661-668, June 2004.

[49] M. G. Villlalva, J. R. Gazoli, and E. Ruppert, “Comprehensive approach to modeling and simulation of photovoltaic arrays,” *IEEE Trans. Power Electron.*, vol. 24, no. 5, pp. 1198–1208, May 2009.

[50] Shengyi Liu and R. A. Dougal, "Dynamic multiphysics model for solar array," in *IEEE Transactions on Energy Conversion*, vol. 17, no. 2, pp. 285-294, Jun 2002.

[51] Z. M. Salameh, M. A. Casacca, and W. A. Lynch, “A mathematical model for lead-acid batteries,” *IEEE Trans. Energy Convers.*, vol. 7, no. 1, pp. 93–98, Mar. 1992.

[52] Min Chen and G. A. Rincon-Mora, "Accurate electrical battery model capable of predicting runtime and I-V performance," in *IEEE Transactions on Energy Conversion*, vol. 21, no. 2, pp. 504-511, June 2006.

[53] Peng Wang; Fang-ming Niu, "Research on the AGC coordination control method including energy storage system based on area control error in the interconnected power grid," in *Future Energy Electronics Conference (IFEEC), 2015 IEEE 2nd International*, pp.1-5, 1-4 Nov. 2015.

[54] Vandoorn, T.L.; De Kooning, J.D.M.; Meersman, B.; Guerrero, J.M.; Vandevelde, L., "Voltage-Based Control of a Smart Transformer in a Microgrid," in *Industrial Electronics, IEEE Transactions on* , vol.60, no.4, pp.1291-1305, April 2013.

[55] Chidurala, A.; Saha, T.; Mithulananthan, N., "Field investigation of voltage quality issues in distribution network with PV penetration," in *Power and Energy Engineering Conference (APPEEC), 2015 IEEE PES Asia-Pacific* , pp.1-5, 15-18 Nov. 2015.

[56] A.A. Milani, M.T.A. Khan, A.Chakrabortty, and I. Husain, “Equilibrium Analysis of Power Distribution Systems Driven by Solid-State Transformer: A Nonlinear Dynamical Approach” submitted for review in *Power Systems, IEEE Transactions.*

[57] F. Wang, G. Wang, A. Huang, W. Yu and X. Ni, "Design and operation of A 3.6kV high performance solid state transformer based on 13kV SiC MOSFET and JBS diode," *2014 IEEE Energy Conversion Congress and Exposition (ECCE)*, Pittsburgh, PA, 2014, pp. 4553-4560.

[58] H. Khorramdel, B. Khorramdel, and M. Poshtyafteh, "Programming of energy storage system in an Island microgrid with photovoltaic and fuel cell," *Walailak J. Eng. Phys. Sci.*, vol. 12, no. 4, pp. 361–371, 2015.

[59] H. Pandžić, Y. Wang, T. Qiu, Y. Dvorkin and D. S. Kirschen, "Near-Optimal Method for Siting and Sizing of Distributed Storage in a Transmission Network," in *IEEE Transactions on Power Systems*, vol. 30, no. 5, pp. 2288-2300, Sept. 2015.

[60] P. Harsha and M. Dahleh, "Optimal Management and Sizing of Energy Storage Under Dynamic Pricing for the Efficient Integration of Renewable Energy," in *IEEE Transactions on Power Systems*, vol. 30, no. 3, pp. 1164-1181, May 2015.

[61] O. C. Rascon, B. Schachler, J. Bühler, M. Resch and A. Sumper, "Increasing the hosting capacity of distribution grids by implementing residential PV storage systems and reactive power control," *2016 13th International Conference on the European Energy Market (EEM)*, Porto, 2016, pp. 1-5.

[62] Jayalakshmi N. S., D. N. Gaonkar, Vikash Kumar J. and Karthik R. P., "Battery-ultracapacitor storage devices to mitigate power fluctuations for grid connected PV system," *2015 Annual IEEE India Conference (INDICON)*, New Delhi, 2015, pp. 1-6.

[63] P. Li; R. Dargaville; Y. Cao; D. Y. Li, "Storage Aided System Property Enhancing and Hybrid Robust Smoothing for Large-scale PV Systems," in *IEEE Transactions on Smart Grid* , vol.PP, no.99, pp.1-1.

[64] H. Bitaraf, S. Rahman and M. Pipattanasomporn, "Sizing Energy Storage to Mitigate Wind Power Forecast Error Impacts by Signal Processing Techniques," in *IEEE Transactions on Sustainable Energy*, vol. 6, no. 4, pp. 1457-1465, Oct. 2015.

[65] M. Vasiladiotis, N. Cherix and A. Rufer, "Impact of Grid Asymmetries on the Operation and Capacitive Energy Storage Design of Modular Multilevel Converters," in *IEEE Transactions on Industrial Electronics*, vol. 62, no. 11, pp. 6697-6707, Nov. 2015.

[66] G. Lei, C. Liu, M. Jafari, J. Zhu and Y. Guo, "Multilevel Robust Design Optimization of a Superconducting Magnetic Energy Storage Based on a Benchmark Study," in *IEEE Transactions on Applied Superconductivity*, vol. 26, no. 7, pp. 1-5, Oct. 2016.

[67] Y. Xu and C. Singh, "Multi-objective design of energy storage in distribution systems based on modified particle swarm optimization," *2012 IEEE Power and Energy Society General Meeting*, San Diego, CA, 2012, pp. 1-8.

[68] X. Li, J. Zhang, Y. He and D. Zhao, "Coordinated control strategy of wind/battery energy storage system hybrid power output based on adaptive dynamic programming," *2016 12th World Congress on Intelligent Control and Automation (WCICA)*, Guilin, 2016, pp. 2052-2057.

[69] J. Qin and R. Rajagopal, "Dynamic programming solution to distributed storage operation and design," *2013 IEEE Power & Energy Society General Meeting*, Vancouver, BC, 2013, pp. 1-5.

[70] Y. Xu, D. Liu, Q. Wei and B. Luo, "Adaptive dynamic programming for residential energy scheduling with solar energy," *2016 12th World Congress on Intelligent Control and Automation (WCICA)*, Guilin, 2016, pp. 845-850.

[71] Y. Tang, H. He, Z. Ni and J. Wen, "Optimal operation for energy storage with wind power generation using adaptive dynamic programming," *2015 IEEE Power & Energy Society General Meeting*, Denver, CO, 2015, pp. 1-6.

[72] M. Khalid, A. V. Savkin and V. G. Agelidis, "Maximizing the income for wind power plant integrated with a battery energy storage system using dynamic programming," *Control Conference (ASCC), 2015 10th Asian*, Kota Kinabalu, 2015, pp. 1-5.

[73] J. Mongkoltanatas, D. Riu and X. LePivert, "Energy storage design for primary frequency control for islanding micro grid," *IECON 2012 - 38th Annual Conference on IEEE Industrial Electronics Society*, Montreal, QC, 2012, pp. 5643-5649.

[74] J. P. Barton and D. G. Infield, "Energy storage and its use with intermittent renewable energy," in *IEEE Transactions on Energy Conversion*, vol. 19, no. 2, pp. 441-448, June 2004.

[75] P. Mercier, R. Cherkaoui and A. Oudalov, "Optimizing a Battery Energy Storage System for Frequency Control Application in an Isolated Power System," in *IEEE Transactions on Power Systems*, vol. 24, no. 3, pp. 1469-1477, Aug. 2009.

[76] G. Delille, B. François and G. Malarange, "Dynamic frequency control support: A virtual inertia provided by distributed energy storage to isolated power systems," *2010 IEEE PES Innovative Smart Grid Technologies Conference Europe (ISGT Europe)*, Gothenburg, 2010, pp. 1-8.

[77] A. Isidori. *Nonlinear Control Systems*, Springer, 1995.

[78] H. Khalil, *Nonlinear Control*, Pearson, 2015.

[79] E. M. Najm, Y. Xu and A. Q. Huang, "Low cost plug-and-play PV system for DC microgrid," *2015 IEEE Energy Conversion Congress and Exposition (ECCE)*, Montreal, QC, 2015, pp. 4236-4242.

[80] *Solar Energy Industries Association Q3 2014 SMI Fact Sheet*, SEIA Secretariat, Washington, DC 2014.

[81] Chung, Donald; Davidson, Carolyn; Fu, Ran; Margolis, Robert., *U.S. Photovoltaic Prices and Cost Breakdowns: Q1 2015 Benchmarks for Residential, Commercial, and Utility-Scale Systems*. National Renewable Energy Laboratory, Golden, CO, 2015. NREL/TP-6A20-64746.

[82] Taylor, M.; Enbar, N.; Kling, Alison., "How Utilities Can Influence Where Distributed Solar Is Located," SEPA Webinar, Washington, DC, Nov, 2014.

[83] SF Environment (2013, Jan 10). *San Francisco Solar Photovoltaic Permitting Guide* [Online].Available:http://www.sfenvironment.org/sites/default/files/fliers/files/sfe_re_sf_solar_pv_permitting_guide.pdf.

[84] Pitt. D. (2013, Dec 20). *Taking the Red Tape Out of Green Power: How to Overcome Permitting Obstacles to Small-Scale Distributed Renewable Energy* [Online].Available:http://www.gracelinks.org/media/pdf/red_tape_report_online.pdf.

[85] *Solar PV Market Update*, Volume 10: Quarter 2, EPRI, Palo Alto, California, June 2014.

[86] *The Impact of Local Permitting on the Cost of Solar Power*, US DoE SunRun Report, January, 2011.

[87] *National Electric Code 2014*, National Fire Protect Association, 2014.

[88] *Inverter, Converters, and Controllers for use in Independent Power Systems*, UL 1741, 2001.

[89] *Standard for Distributed Resources Interconnected with Electric Power Systems*, IEEE Standard 1547, 2003.

[90] Bin Gu; Dominic, J.; Jingyao Zhang; Lanhua Zhang; Baifeng Chen; Jih-Sheng Lai, "Control of electrolyte-free microinverter with improved MPPT performance and grid current quality," *Applied Power Electronics Conference and Exposition (APEC), 2014 Twenty-Ninth Annual IEEE* , pp.1788, 1792, 16-20 March 2014.

[91] M. Wang, W. Yu and A. Q. Huang, "Power-weighting-based multiple input and multiple output control strategy for single-phase PV cascaded H-bridge multilevel grid-connected inverter," *2015 IEEE Applied Power Electronics Conference and Exposition (APEC)*, Charlotte, NC, 2015, pp. 2148-2153.

[92] Alam, M. K.; Khan, F.; Johnson, J.; Flicker, J., "PV ground-fault detection using spread spectrum time domain reflectometry (SSTDR)," *Energy Conversion Congress and Exposition (ECCE), 2013 IEEE* , pp.1015,1020, 15-19 Sept. 2013.

[93] Zhihua Li, Yuanzhang Wang, Diqing Zhou, and Chunhua Wu, “An Intelligent Method for Fault Diagnosis in Photovoltaic Array”, ICSC 2012, Part II, CCIS 327, pp. 10, 16, 2012.

[94] *Introduction to Modbus TCP/IP*, Acromag Incorporated, Wixom, MI, USA.

[95] E. M. Najm and A. Q. Huang, "Integrated DC/DC parallel PnP PV architecture method for powering residential buildings," *DC Microgrids (ICDCM), 2015 IEEE First International Conference on*, Atlanta, GA, 2015, pp. 371-376.